AD-A154 783 SOLID STATE RESEARCH(U) MASSACHUSETTS INST OF TECH 1/2
LEXINGTON LINCOLN LAB A L MCWHORTER 15 AUG 84 1984-3
ESD-TR-84-042 F19628-85-C-0002

UNCLASSIFIED F/G 20/12 NL

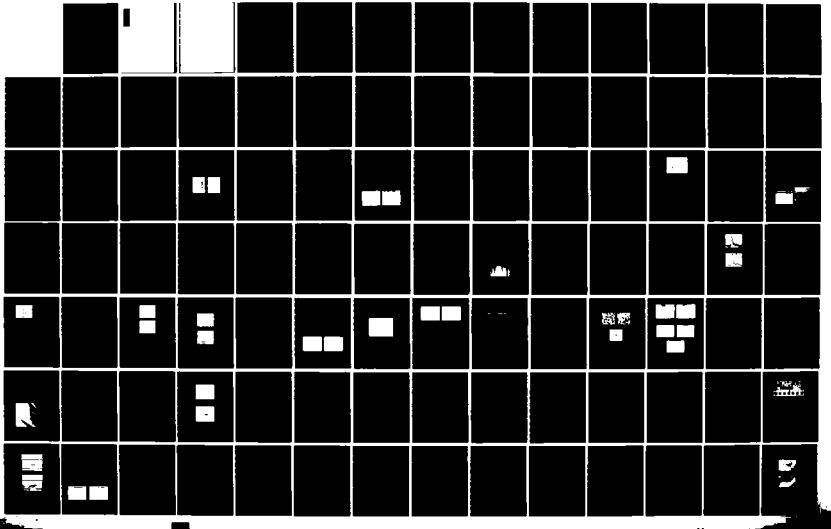

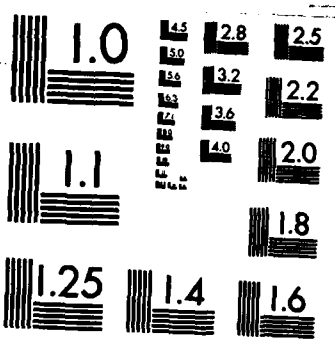

MASSACHUSETTS INSTITUTE OF TECHNOLOGY
LINCOLN LABORATORY

# SOLID STATE RESEARCH

## QUARTERLY TECHNICAL REPORT

1 MAY — 31 JULY 1984

ISSUED 28 DECEMBER 1984







LEXINGTON MASSACHUSETTS

## ABSTRACT

This report covers in detail the sold state research work of the Solid State Division at Lincoln Laboratory for the period 1 May through 31 July 1984. The topics covered are Solid State Device Research, Quantum Electronics, Materials Research, Microelectronics, and Analog Device Technology. Funding is primarily provided by the Air Force, with additional support provided by the Army, DARPA, Navy, NASA, and DOE.

# TABLE OF CONTENTS


| | | |
|---|---|---|
| Abstract | | iii |
| List of Illustrations | | vii |
| List of Tables | | xii |
| Introduction | | xiii |
| Reports on Solid State Research | | xvii |
| Organization | | xxix |
| 1. SOLID STATE DEVICE RESEARCH | | 1 |
| | 1.1 Traveling-Wave Electrooptic Modulator with Maximum Bandwidth-Length Product | 1 |
| | 1.2 Frequency Response of a GaAs Guided-Wave Electrooptic Interferometer Modulator | 4 |
| | 1.3 A Surface-Emitting GaInAsP/InP Laser with Low Threshold Current and High Efficiency | 7 |
| | 1.4 Extremely Rapid Outdiffusion of Fe from InP | 12 |
| | 1.5 Substrate Transfer Technique for the LPE Growth of InGaAs(Fe) | 13 |
| 2. QUANTUM ELECTRONICS | | 19 |
| | 2.1 Continuously Tunable Infrared LIDAR System Using a Co:$MgF_2$ Laser | 19 |
| | 2.2 Picosecond GaAlAs Diode Laser Amplifier | 23 |
| | 2.3 Use of Spatial Time-Division Repetition Rate Multiplication of Mode-Locked Laser Pulses to Generate Microwave Radiation from Optoelectronic Switches | 26 |
| 3. MATERIALS RESEARCH | | 31 |
| | 3.1 Merged CMOS/Bipolar Technologies Utilizing Zone-Melting-Recrystallized Si-On-Insulator Films | 31 |
| | 3.2 Selective Tungsten Silicide Formation by Ion-Beam Mixing and Rapid Thermal Annealing | 34 |
| | 3.3 MESFETS Fabricated in GaAs Layers Grown Directly on Si Substrates by Molecular Beam Epitaxy | 40 |
| | 3.4 New High-Efficiency GaAs Solar Cell Structure Using a Heterostructure Back-Surface Field | 45 |

4. MICROELECTRONICS 53

4.1 Gallium Arsenide Overlapping Gate Charge-Coupled Devices 53
4.2 Microwave Performance of OMCVD-Overgrown PBTs 57
4.3 A Comparison of E-Beam Evaporated and Electroplated AuZn Ohmic Contacts to p-Type GaAs 60
4.4 Ion-Beam-Assisted Etching of Diamond 66
4.5 Planar Receptors at 140 GHz Using Dipole Antennas 70

5. ANALOG DEVICE TECHNOLOGY 75

5.1 Surface-Acoustic Wave/Field-Effect Transistor Wideband Programmable Filter 75
5.2 InP Optoelectronic Sampler for a Wideband Radar Signal Processor 79

# LIST OF ILLUSTRATIONS


| Figure No. | | Page |
|---|---|---|
| 1-1 | Schematic Diagram of Traveling-Wave Mach-Zehnder Interferometric Modulator | 1 |
| 1-2 | SEM Photographs of Traveling-Wave Electrode. A 500X Magnification of the Center Electrode with the Ground Planes on Either Side (Top) and a 5000X Magnification of Center of Above Photograph (Bottom). The Gap Between Electrodes is 4 $\mu$m Wide | 2 |
| 1-3 | Linear Small-Signal Frequency Response of Traveling-Wave Modulator. Measured Response Is Shown by X Points and Theoretically Predicted Response Is Shown by Solid Line | 3 |
| 1-4 | Schematic Illustration of GaAs Electrooptic Interferometric Modulator | 4 |
| 1-5 | Scanned Output of Interferometer: (a) Biased for a Maximum Output in the Center Guide, and (b) Biased for a Minimum Output in the Center Guide | 5 |
| 1-6 | Frequency Response of Interferometers Obtained from Swept-Frequency Measurements: (o) Optical Response Obtained with Interferometer Biased at a Vp Point; ($\Delta$) Square Root of Above When Biased at a Linear Optical Response Point $V_{\pi}/2$. The Electrical Bandwidth of the Interferometer Electrode Structure Is $\approx$2.2 GHz (Point A), Which Translates into a Linear Optical Bandwidth of $\approx$3.0 GHz (Point B). | 6 |
| 1-7 | A Schematic Cutaway View of the Surface-Emitting GaInAsP/InP Laser. The Surface Emission Is Achieved by Adding a 45° Mirror to A Previously Developed Buried-Heterostructure Laser with Transported Mirrors. | 8 |
| 1-8 | Simultaneous Fabrication of the 45° (Parabolic) and the Transported Mirrors. The Dotted Curve Is a Parabola with Its Focus at Point F. | 9 |
| 1-9 | SEM Photograph of an Approximately Parabolic Mirror (Left) and a Transported Mirror (Right). [cf. Figure 1-8(c)]. | 10 |
| 1-10 | Light Output Vs Current Characteristic of a Surface-Emitting GaInAsP/InP Laser. The Laser Is Mounted P-Side Up on a Copper Sink as Shown in the Insert | 10 |
| 1-11 | Far-Field Pattern of a Surface-Emitting GaInAsP/InP Laser | 11 |

| Figure No. | | Page |
|---|---|---|
| 1-12 | Photomicrographs of Cleaved and Stained Cross Section under Nomarski Contrast. Right: Approximately 600× Magnification Showing Epitaxial Growth (≈3 $\mu$m Thick); Left: Approximately 150× Magnification Showing Full Thickness of Substrate. Weak Lines ≈ 30 $\mu$m from Top and Bottom Surface Occur at Transition from Conducting to Semi-Insulating Regions | 12 |
| 1-13 | Schematic Drawing of Substrate-Transfer Apparatus Cross Section Showing Platform and Transfer Rod Which Have Been Added to the Push/Pull Piece | 14 |
| 1-14 | Curves Show $n_{eff}$ and $\rho$ Vs n as Calculated from the Two-Band Conduction Model with $\mu_n = 1 \times 10^4$ cm$^2$/V-s, $\mu_p = 150$ cm$^2$/V-s and $n_i = 1 \times 10^{12}$ cm$^{-3}$. Measured $n_{eff}$ Values Have Been Placed on the $n_{eff}$ Vs n Curve to Determine n Values. These, in Turn, Are Used to Make the Comparison between Measured and Predicted $\rho$ Values | 14 |
| 2-1 | Optically Pumped Co:$MgF_2$ Laser Used in the Remote Sensing LIDAR System | 19 |
| 2-2 | Co:$MgF_2$ LIDAR System | 20 |
| 2-3 | Frequency Scan of LIDAR Signal Returns from Foliage on Hillside at a Range of 6.7 km | 21 |
| 2-4 | Range-Resolved LIDAR Signals Backscattered from Aerosols (a) at Water Vapor Absorption Frequency and (b) Off-Resonance. (Energy/Pulse = 5 mJ) | 22 |
| 2-5 | Schematic Illustration of Experimental Arrangement | 24 |
| 2-6 | (a) Unamplified Pulse from Comb-Generator-Driven GaAlAs Diode Laser. Average Laser Power 1 mW, Repetition Rate 1 GHz. (b) Amplified Diode Laser Pulse at an Amplifier Current i = 100 mA | 25 |
| 2-7 | Net Gain as Function of Amplifier Injection Current | 26 |
| 2-8 | Demonstration of Gated Diode Laser Amplifier. See Text for Explanation | 27 |
| 2-9 | Schematic Arrangement of Optical Components Used for Spatial Time-Division Repetition Rate Multiplication of Mode-Locked Laser Pulses | 28 |

| Figure No. | | Page |
|---|---|---|
| 2-10 | Oscilloscope Traces Showing Spatial Time-Division Repetition Rate Multiplication of Mode-Locked Laser Pulses Using System with Three Retroprisms and Four Beam Splitters. Time Scale Is 500 ps/div. (a) Top Trace Is Input Signal While Lower Three Traces Show the Generation of Repetition Rates $2f_o$, $4f_o$, and $8f_o$. (b) Top Trace Is the Input Signal While Lower Traces Are the Outputs with Retroprism 3, Retroprisms 2 and 3, and Retroprisms 1, 2, and 3 in the Optical Path, Respectively | 29 |
| 2-11 | Output on an RF Spectrum Analyzer from a GaAs Avalanche Photodiode Driven by the 2-GHz Signal in Figure 2-10. Amplitude Scale Is Linear. The Two Traces Represent Two Frequency Ranges for the Same Signal | 30 |
| 3-1 | Schematic Diagrams of Two Configurations with SOI/CMOS and Bipolar Devices Fabricated on the Same Si Wafer. The Bipolar Device Is Fabricated in (a) the SOI Film or (b) Epitaxial Layers Grown Selectively on the Si Substrate | 32 |
| 3-2 | Drain I-V Characteristics of SOI/MOSFETs: (a) n-Channel and (b) p-Channel. Gate Length Is 2 $\mu$m, and Gate Widths Are 30 $\mu$m for n-Channel Devices and 50 $\mu$m for p-Channel Devices | 32 |
| 3-3 | Output Waveform of 39-Stage SOI/CMOS Ring Oscillator for 5-V Supply Voltage. The Propagation Delay per Stage is ~280 ps | 33 |
| 3-4 | Common-Emitter I-V Characteristics for Bipolar Transistors: (a) SOI and (b) Epitaxial | 34 |
| 3-5 | Schematic Structure of a MOSFET with Self-Aligned Silicided Gate, Source, and Drain | 35 |
| 3-6 | Rutherford Backscattering Spectra of W-Coated Si Samples After Annealing: (a) without $As^+$ Implant, (b) with $As^+$ Implant | 36 |
| 3-7 | Transmission Electron Micrographs of $WSi_2$ Films Formed by RTA at (a) 950°C, (b) 1000°C, and (c) Electron Diffraction Pattern Showing Tetragonal $WSi_2$ Phase | 37 |
| 3-8 | Photomicrographs of $WSi_2$ Stripes Formed on Patterned Oxidized Si Wafers by RTA at (a) 950°C and (b) 1000°C | 38 |
| 3-9 | Diode I-V Characteristics for Shallow $n^+$-p Junctions Formed by Ion-Beam Mixing and RTA. The $As^+$ Ion Implantation Was Performed at Energies of (a) 180, (b) 150, and (c) 120 KeV | 38 |

| Figure No. | | Page |
|---|---|---|
| 3-10 | Distribution of Leakage Currents (Measured at a Reverse Bias of 5V) for Diodes with Different As Implant Energies | 39 |
| 3-11 | Cross-Sectional TEM of GaAs/Si Heteroepitaxial Test Structure. Scale: 20 mm = 0.5 $\mu$m | 41 |
| 3-12 | Photoluminescence Spectrum at 5 K of Nominally Undoped GaAs Layer Grown Directly on Si | 42 |
| 3-13 | Schematic Diagram of MGS MESFET | 42 |
| 3-14 | Schottky Diode Characteristic of MGS MESFET | 44 |
| 3-15 | Transistor Characteristics of MGS MESFET with Substrate Biased at +5.0 V | 44 |
| 3-16 | Schematic Energy Band Diagram of $n^+/p/p^+$ Shallow-Homojunction Solar Cell with Heterostructure Back-Surface Field | 45 |
| 3-17 | Schematic Cross Section of Shallow-Homojunction GaAs Solar Cell with GaAs/AlGaAs Heterostructure BSF | 46 |
| 3-18 | Open-Circuit Voltage as a Function of Short-Circuit Density for Heterostructure BSF and Conventional Cells under AM1 Illumination at Various Stages of $n^+$ Anodic Thinning | 46 |
| 3-19 | Photocurrent as a Function of Voltage for a GaAs Cell with Heterostructure BSF | 48 |
| 3-20 | External Quantum Efficiency as a Function of Wavelength for the Cell of Figure 3-19 | 48 |
| 4-1 | Fabrication Sequence of GaAs Overlapping Gate CCD | 54 |
| 4-2 | Four-Phase GaAs Overlapping Gate CCD | 55 |
| 4-3 | CCD Input (Top) and Output (Bottom) for (a) 64-$\mu$s Space between Pulse Bursts, and (b) 10-ms Space between Pulse Bursts | 56 |
| 4-4 | DC Characteristics of GaAs PBTs Overgrown by (a) VPE, and (b) OMCVD | 57 |
| 4-5 | Short-Circuit Current Gain Vs Frequency for Various GaAs PBTs | 58 |
| 4-6 | Power Gain Vs Frequency for Various GaAs PBTs | 58 |
| 4-7 | Comparison of Model Elements for GaAs PBTs | 59 |
| 4-8 | Theoretical Ohmic Contact Resistivities to p-Type GaAs as a Function of Doping Concentration | 62 |

| Figure No. | | Page |
|---|---|---|
| 4-9 | Auger Sputter Profile of Evaporated AuZn Contact | 63 |
| 4-10 | Auger Sputter Profile of Electroplated Au with 0.5% Zn Contact | 64 |
| 4-11 | Auger Sputter Profile of Evaporated Au in Combination with Electroplated Au with 0.5% Contact | 65 |
| 4-12 | Drawing of a Cross Section of IBAE System Utilizing the $LN_2$ Trap to Isolate the Reactive Gas Region from the Ion Gun | 66 |
| 4-13 | The Etching Rate of Diamond as a Function of Equivalent Reactive Gas Pressure | 67 |
| 4-14 | The Etching Rate of Diamond as a Function of Diamond Temperature | 68 |
| 4-15 | The Etching Rate of Diamond and the Sputter Etching Rate of the Al Mask as a Function of the Angle between the Ion Beam and the Normal to the Substrate | 68 |
| 4-16 | SEM Comparing Two Samples. The Sample Shown in the Top Micrograph Was Etched 10 $\mu$m Deep with the Ion Beam at 45° to the Substrate Normal and the Sample Shown in the Lower Micrograph Was Etched with the Ion Beam Normal to the Substrate | 69 |
| 4-17 | SEM of a Periodic Structure with 18-$\mu$m Pitch Etched 17-$\mu$m Deep at 45° | 70 |
| 4-18 | Double Dipole Microstrip Antenna on Quartz Substrate | 71 |
| 4-19 | E- and H-Plane Radiation Patterns at 132 GHz | 72 |
| 5-1 | Schematic View of Air-Gap Structure. The Air Gap Is Typically 3000 Å in Height; the Electric Fields of the SAW Delay Line Are Coupled Through the Air Gap into the Silicon | 75 |
| 5-2 | Schematic View of the SAW/FET. The View Is Through the $LiNbO_3$ Showing the Alignment of the Silicon Chip with the SAW Delay Line | 76 |
| 5-3 | Equivalent Circuit of SAW/FET Unit Cell. Each Track of the Device Contains 175 Identical Unit Cells Which Drive the RF Load in Parallel. This Unit Cell Is Used for Computations of the Circuit Model | 77 |

| Figure No. | | Page |
|---|---|---|
| 5-4 | Output of SAW/FET Operated as a Matched Filter. Top Trace Is Output; Middle Trace Is Input, both Displayed at 1 $\mu$s/div. Bottom Trace Is Program Input, in this Case a Sine Wave of Frequency 0.9 MHz. Superimposed on the Bottom Trace Is the Shift Register Bit Which Controls the FET Switches. Bottom Trace Is Displayed at 20 $\mu$s/div. | 78 |
| 5-5 | SAW/FET Inpulse Response for the Programming Waveform Shown in the Photograph. Top Trace: Input Impulse; Middle Trace: Filter Output. Bottom: Program Input Superimposed on Shift Register Bit. Input and Output Are Displayed at 200 ns/div. Program Input Is Displayed at 20 $\mu$s/div. The Programming Voltage Turns Alternating Groups of Ten Taps On and Off | 78 |
| 5-6 | Circuit Diagram of the Optoelectronic Track-and-Hold | 80 |
| 5-7 | (a) Equivalent Circuit for Optoelectronic Track-and-Hold; (b) Model of the Time-Variant Conductance of InP Switch, $G_s(t)$, Controlled by the Laser Command Pulses | 81 |
| 5-8 | Square-Wave Responses of Optoelectronic Track-and-Hold Circuits Using (a) a 2-$\mu$m Switch, and (b) a 6-$\mu$m Switch | 83 |
| 5-9 | SPICE Simulated Response Functions, $h(t,\tau)$, of Optoelectronic Track-and-Hold Circuits for (a) Single Stage, and (b) Two Cascaded Stages | 84 |
| 5-10 | Responses of Track-and-Hold Circuits to 110-MHz Sine Wave Inputs with a 100-MHz Sampling Rate. (a) Experimental and (b) Simulated Responses for Single-Stage Track-and-Hold; (c) Experimental and (d) Simulated Responses for Two-Stage Track-and-Hold | 86 |


## LIST OF TABLES


| Table No. | | Page |
|---|---|---|
| 4-1 | Ohmic Deposition Techniques and Results | 61 |

| MS No. | | | |
|---|---|---|---|
| 6628 | GaAs Permeable Base Transistors Fabricated Using Organometallic Chemical Vapor Deposition | K.B. Nichols<br>R.P. Gale<br>M.A. Hollis<br>G.A. Lincoln<br>C.O. Bozler | 1984 Device Research Conference, Santa Barbara, 18-20 June 1984 |
| 6632 | Microwave Oscillations and Optical Effects from Resonant Tunneling Quantum Well Structures | T.C.L.G. Sollner<br>P.E. Tannenwald<br>W.D. Goodhue<br>D.D. Peck<br>H.Q. Le | |
| 6637 | Lateral Photodetectors on Semi-Insulating InGaAs and InP | V. Diadiuk<br>S.H. Groves | |
| 6647 | 14 GHz Operation of Q-Switched Diode Lasers | D.Z. Tsang<br>J.N. Walpole<br>S.H. Groves<br>Z.L. Liau | |
| 6652 | GaAs MESFETS and AlGaAs Double-Heterostructure Diode Lasers Fabricated on Monolithic GaAs/Si Substrates | H.K. Choi<br>T.H. Windhorn<br>B-Y. Tsaur<br>G.M. Metze<br>G.W. Turner<br>J.C.C. Fan | |
| 6660 | Na Profiles in SiO Films by Fluorescence Induced During Reactive-Ion Etching | S.R.J. Brueck<br>S.W. Pang<br>T.F. Deutsch | Gordon Conference on Plasma Chemistry, Tilton, New Hampshire, 13-17 August 1984 |
| 6668 | Surface-Acoustic-Wave Chirp Transformers | R.C. Williamson | Workshop on Signal Processing Devices, Santa Fe, 21-25 May 1984 |
| 6682 | Optical Interconnects for VLSI | F.J. Leonberger | Gordon Conference on Optical Information Processing, Plymouth, New Hampshire, 12 June 1984 |
| 6714 | Dry Etching Induced Damage in GaAs and Si | S.W. Pang | Gordon Research Conference, Wolfeboro, New Hampshire, 11 July 1984 |
| 6715 | Ion Beam Induced Etching | M.W. Geis<br>J.N. Randall<br>N.N. Efremow<br>G.A. Lincoln<br>N.P. Economou | |

| MS No. | | | |
|---|---|---|---|
| 6571 | Investigation of Undesired Impurity Incorporation in the GaAs Overgrowth of Submicrometer-Period Gratings | M.A. Hollis<br>K.B. Nichols<br>C.O. Bozler<br>A.R. Calawa<br>M.J. Manfra | 1984 Electronic Materials Conference, Santa Barbara, California, 20-22 June 1984 |
| 6584 | Selective Tungsten Silicide Formation by Ion Beam Mixing and Rapid Thermal Annealing | B-Y. Tsaur<br>C.K. Chen<br>C.H. Anderson, Jr.<br>D.L. Kwong* | |
| 6576 | High Average Power Mode-Locked Co:$MgF_2$ Laser | B.C. Johnson<br>M. Rosenbluh<br>P.F. Moulton<br>A. Mooradian | Ultrafast Phenomena Conference Meeting, Monterey, 12-15 June 1984 |
| 6597 | Picosecond Gain Measurements of a GaAlAs Diode Laser | W.Lenth | |
| 6580 | Ion Beam Resist Exposure Using Grid Support Stencil Masks | J.N. Randall<br>D.C. Flanders<br>N.P. Economou<br>J.P. Donnelly<br>E.I. Bromley | EIPBT 1984, Tarrytown, New York, 29 May-1 June 1984 Accepted by J. Vac. Sci. Technol. |
| 6598 | Epitaxial Semiconductor Insulator Structures — GaAs/Fluoride/GaAs (001) | P.W. Sullivan*<br>G.M. Metze<br>M. Rona*<br>J.E. Bower* | Third International Conference on MBE, San Francisco, 1-3 August 1984 |
| 6602 | Remote Sensing Using a Continuously Tunable Co:$MgF_2$ Laser | N. Menyuk<br>D.K. Killinger<br>S. Lovold*<br>P.F. Moulton<br>A. Mooradian | 12th International Laser Radar Conference, Aix-en-Provence, France, 13-17 August 1984 |
| 6613 | Low Power Ion-Beam-Assisted Etching of InP | N.L. DeMeo<br>J.P. Donnelly<br>F.J. O'Donnell<br>M.W. Geis<br>K.J. O'Connor | IBMM '84, Ithaca, New York, 16-19 July 1984 |

* Author not at Lincoln Laboratory.

| MS No. | | | |
|---|---|---|---|
| 6536 | Temperature Dependence of Quantum-Fluctuation Linewidth Broadening in (GaAl)As Diode Lasers | J. Harrison<br>A. Mooradian | CLEO '84, Anaheim, California, 19-22 June 1984 |
| 6542 | High Average Power Mode-Locked Operation of Co:$MgF_2$ and Ni:$MgF_2$ Lasers | B.C. Johnson<br>M. Rosenbluh<br>P.F. Moulton<br>A. Mooradian | |
| 6550 | Recent Advances in Solid State Lasers | P.F. Moulton | |
| 6646 | Optical Analysis of Device Materials, Structures and Processing | S.R.J. Brueck | |
| 6531A | Planar GaAs p-i-n Photodiode with Picosecond Time Response | W. Lenth | Seminar, IBM Research Laboratory, San Jose, 13 August 1984 |
| 6562A | Advances in Mass Transport Buried-Heterostructure InGaAsP Lasers | Z.L. Liau<br>J.N. Walpole<br>D.Z. Tsang | Seminar, M.I.T., 9 May 1984 |
| 6563 | Distributed Nonlinear Devices for Signal Processing Applications | S.A. Reible | Symposium on Transport and Propagation in Nonlinear Systems, Los Alamos, 23 May 1984 |
| 6564 | Reconfiguring Semi-custom ICS Using Lasermicrochemical Techniques | W.S. Graber*<br>D.J. Ehrlich<br>J.Y. Tsao<br>D.J. Silversmith<br>J.H.C. Sedlacek<br>R.W. Mountain | Custom Integrated Circuits Conference, Rochester, New York, 21-23 May 1984 |
| 6568 | Recent Advances in LPE of $Hg_{1-x}Cd_xTe$ Horizontal Slider | T.C. Harman | 1984 Electronic Materials Conference, Santa Barbara, California, 20-22 June 1984 |
| 6570 | Substrate-Transfer Technique for LPE Growth of InGaAs(Fe) | S.H. Groves<br>M.C. Plonko<br>D.L. Hovey | |

* Author not at Lincoln Laboratory.

| MS No. | | | |
|---|---|---|---|
| 6400C | Laser Photochemical Processing | D.J. Ehrlich | Seminar, Eastman Kodak, Rochester, New York, 22 May 1984 |
| 6479 | PMMA and Gold Proton Masks for Gallium Arsenide | S. Rabe<br>C.O. Bozler<br>N.N. Efremow | WOCSEMMAND 1984, San Francisco, 19-23 February 1984 |
| 6489A | Novel Processing Using Self-Developing Resist | M.W. Geis<br>J.N. Randall | American Vacuum Society, New England Annual Symposium, Nashua, New Hampshire, 11-12 June 1984 |
| 6567A | Submicrometer Structures in Si and Their Application to High Speed Devices | D.D. Rathman | |
| 6653 | Selective Epitaxial Growth and Its Applications | C.O. Bozler | |
| 6508 | Measurement and/or Processing of Optical Wavefronts Using Integrated Guided-Wave Optics | R.H. Rediker<br>T.A. Lind<br>B.E. Burke | CLEO '84, Anaheim, California, 19-22 June 1984 |
| 6523 | 4-Bit 1-GSample/sec Electrooptic Guided-Wave Analog-to-Digital Converter | R.A. Becker<br>C.E. Woodward<br>L.M. Johnson<br>F.J. Leonberger | |
| 6527 | Progress in Surface Photoacoustic Wave Spectroscopy of Thin Films | S.R.J. Brueck<br>T.F. Deutsch<br>D.E. Oates | |
| 6529 | Laser Direct Writing: A Capsule Review of the Methods and Applications in Microelectronics | D.J. Ehrlich<br>J.Y. Tsao | |
| 6530 | A Multiple Waveguide Lens | H.A. Haus*<br>L. Molter-Orr*<br>F.J. Leonberger | |
| 6531 | Planar GaAs p-i-n Photodiode with Picosecond Time Response | W. Lenth<br>A. Chu<br>L.J. Mahoney<br>R.W. McClelland<br>R.W. Mountain<br>D.J. Silversmith | |

* Author not at Lincoln Laboratory.

| JA No. | | | |
|---|---|---|---|
| 5666 | Effects of Ion Species and Adsorbed Gas on Dry Etching Induced Damage in GaAs | S.W. Pang<br>M.W. Geis<br>N.N. Efremow<br>G.A. Lincoln | Accepted by J. Vac. Sci. Technol. |
| 5667 | Nitrocellulose as a Positive or Negative Self-Developing Resist | M.W. Geis<br>J.N. Randall<br>R.W. Mountain<br>J.D. Woodhouse<br>E.I. Bromley<br>D.K. Astolfi<br>N.P. Economou | Accepted by J. Vac. Sci. Technol. |

## Meeting Speeches*

| MS No. | | | |
|---|---|---|---|
| 5167A | System Requirements for Signal-Processing Devices | J.H. Cafarella | Workshop on Signal Processing Devices, Santa Fe, 21-25 May 1984 |
| 6389E | Wideband Analog Signal Processing with Superconductive Circuits | R.W. Ralston | |
| 6666 | Si CCD Fourier Transformers | A.M. Chiang | |
| 5934B | Thin Films of III-V Compounds and Their Applications | J.C.C. Fan | ACCG-6/ICVGE-6, Atlantic City, 15-20 July 1984 |
| 6078C | Microstructure Electromagnetic Effects in Laser-Material Interaction | S.R.J. Brueck | Seminar, Hughes Research Laboratories, Malibu, California, 25 June 1984 |
| 6389D | Wideband Analog Signal Processing with Superconductive Circuits | S.A. Reible | Technical Seminar, National Bureau of Standards, Boulder, 1 May 1984 |
| 6400B | Laser Direct Patterning: New Chemical Mechanisms and Solid-State Device Applications | D.J. Ehrlich<br>J.Y. Tsao | International Conference on Laser Processing and Diagnostics, Linz, Austria, 15-19 July 1984 |
| 6650 | Optical Microanalysis of Device Materials and Structures | S.R.J. Brueck | |

* Titles of Meeting Speeches are listed for information only. No copies are available for distribution.

| JA No. | | | |
|---|---|---|---|
| 5595 | Theoretical Analysis of Coherently Coupled Optical Waveguide Bends | L.M. Johnson<br>D. Yap | Accepted by Appl. Opt. |
| 5600 | Coupling Between Successive Ti:$LiNbO_3$ Waveguide Bends and Branches | D. Yap<br>L.M. Johnson | Accepted by Appl. Opt. |
| 5607 | High Frequency Heterodyne Spectroscopy with Current-Modulated Diode Lasers | W. Lenth | Accepted by IEEE J. Quantum Electron. |
| 5611 | Optimal Design of CdS and $Cd_{0.8}Zn_{0.2}$ S-Based Single Junction and Multi-Junction Solar Cells | J.C.C. Fan<br>B.J. Palm | Accepted by Solar Cells |
| 5627 | Picosecond Gain Measurements in a GaAlAs Diode Laser | W. Lenth | Accepted by Opt. Lett. |
| 5637 | A Guided-Wave Gallium Arsenide Monolithic Interferometer | J.P. Donnelly<br>N.L. DeMeo<br>G.A. Ferrante<br>K.B. Nichols<br>F.J. O'Donnell | Accepted by Appl. Phys. Lett. |
| 5644 | Use of Spatial Time-Division Repetition Rate Multiplication of Mode-Locked Laser Pulses to Generate Microwave Radiation from Optoelectronic Switches | A. Mooradian | Accepted by Appl. Phys. Lett. |
| 5653 | A Comparison of Laser-Initiated and Thermal Chemical Vapor Deposition of Tungsten Films | T.F. Deutsch<br>D.D. Rathman | Accepted by Appl. Phys. Lett. |
| 5661 | Repair of X-Ray Lithographic Masks Using UV-Laser Photodeposition | J.N. Randall<br>D.J. Ehrlich<br>J.Y. Tsao | Accepted by J. Vac. Sci. Technol. |
| 5664 | Ion-Beam-Assisted Etching of Diamond | N.N. Efremow<br>M.W. Geis<br>D.C. Flanders<br>G.A. Lincoln<br>N.P. Economou | Accepted by J. Vac. Sci. Technol. |

| MS No. | | | |
|---|---|---|---|
| 6524 | Surface and Gas Processes in Photodeposition in Small Zones | J.Y. Tsao<br>D.J. Ehrlich | *Laser Assisted Deposition, Etching and Doping,* S.D.Allen, Ed., Proc. SPIE **459**, 2-8 (1984) |
| 6540 | Buried Heterostructure Q-Switched Diode Lasers | D.Z. Tsang<br>J.N. Walpole<br>Z.L. Liau<br>S.H. Groves | *Optical Interfaces for Digital Circuits and Systems,* R.A. Milano, Ed., Proc. SPIE **466**, 40-44 (1984) |
| 6541 | Electron Beam Techniques for Integrated Circuit Testing and Customization | D.C. Shaver | Proceedings 1984 Custom Integrated Circuit Conference Rochester, New York, 21-23 May 1984, pp. 606-609 |
| 6544 | GaAs Monolithic Frequency Doublers with Series Connected Varactor Diodes | A. Chu<br>W.E. Courtney<br>L.J. Mahoney<br>R.W. McClelland<br>H.A. Atwater | 1984 IEEE Microwave and Millimeter-Wave Monolithic Circuits Symposium Digest of Papers, H.J. Kuno, Ed., San Francisco, 29 May-1 June 1984, pp. 74-77 |
| 6575 | Receiver Technology for the Submillimeter Wave Region | B.J. Clifton | International Conference on IR Physics, Zurich, Switzerland, 23-27 July 1984, p. 1 |

* * * * *

## UNPUBLISHED REPORTS

### Journal Articles

| JA No. | | | |
|---|---|---|---|
| 5560 | Molecular Beam Epitaxy Of GaAs and AlGaAs on Si | B-Y. Tsaur<br>G.M. Metze | Accepted by Appl. Phys. Lett. |
| 5578 | Patterned Photonucleation of Chemical Vapor Deposition of Al by UV-Laser Photodeposition | J.Y. Tsao<br>D.J. Ehrlich | Accepted by Appl. Phys. Lett. |
| 5587 | Spectral Characteristics of (GaAl)As Diode Lasers at 1.7 K | J. Harrison<br>A. Mooradian | Accepted by Appl. Phys. Lett. |

## Meeting Speeches

| MS No. | | | |
|---|---|---|---|
| 6343 | High-Quality Silicon Films Prepared by Zone-Melting Recrystallization | C.K. Chen<br>M.W. Geis<br>B-Y. Tsaur<br>J.C.C. Fan | Proceedings of the Flat-Plate Solar Array Project Research Forum on the High-Speed Growth and Characterization of Crystals for Solar Cells, Port St. Lucie, Florida, 25-27 July 1983, p. 419 |
| 6378 | Measurements of Electroacoustic Coefficients in $LiNbO_3$ and $LiTaO_3$ and Application to Signal-Processing Devices | P.G. Gottschalk<br>D.E. Oates<br>P.V. Wright | 1983 Ultrasonics Symposium Proceedings, (IEEE, New York, 1983), pp. 1091-1095 |
| 6379 | Surface-Photoacoustic-Wave Spectroscopy of Thin Films | D.E. Oates<br>S.R.J. Brueck<br>T.F. Deutsch | 1983 Ultrasonics Symposium Proceedings, (IEEE, New York, 1983), pp. 695-699 |
| 6385 | Integration of Multiple Elastic Convolvers into a Communication Signal Processor | V.S. Dolat<br>G.T. Flynn | 1983 Ultrasonics Symposium Proceedings, (IEEE, New York, 1983), pp. 137-142 |
| 6409 | The Role of Oxygen in Zone-Melting Recrystallization of Silicon-On Insulator Films | J.C.C. Fan<br>B-Y. Tsaur<br>C.K. Chen<br>J.R. Dick*<br>L.L. Kazmerski* | *Materials Research Society Symposium Proceedings,* Vol. 23, (Elsevier, New York, 1984), pp. 477-489 |
| 6423 | InP Optoelectronic Switches and Their High-Speed Signal-Processing Applications | C.H. Cox, III<br>V. Diadiuk<br>I. Yao<br>F.J. Leonberger<br>R.C. Williamson | *Picosecond Optoelectronics,* G. Mourou, Ed., Proc. SPIE **439**, 164-168 (1983) |

* Author not at Lincoln Laboratory.

| JA No. | | | |
|---|---|---|---|
| 5606 | Optical Interconnections for VLSI Systems | J.W. Goodman*<br>F.J. Leonberger<br>S-Y. Kung*<br>R.A. Athale* | Proc. IEEE **72**, 850 (1984) |
| 5612 | Effects of Ionizing Radiation on SOI/CMOS Devices Fabricated in Zone-Melting Recrystallized Si Films on $SiO_2$ | B-Y. Tsaur<br>R.W. Mountain<br>C.K. Chen<br>G.W. Turner<br>J.C.C. Fan | IEEE Electron Device Lett. **EDL-5**, 238 (1984) |
| 5614 | Low-Loss Multiple-Branching Circuit in Ti-Indiffused $LiNbO_3$ Channel Waveguides | R.A. Becker<br>L.M. Johnson | Opt. Lett **9**, 246 (1984) |
| 5617 | Computer-Aided Design of Quartz Elliptical Deflector Templates | D.L. Hovey | Fusion (J. Amer. Sci. Glass-blowers' Soc.) **XXXI**, (1984) |
| 5618 | AlGaAs Double-Heterostructure Diode Lasers Fabricated on a Monolithic GaAs/Si Substrate | T.H. Windhorn<br>G.M. Metze<br>B-Y. Tsaur<br>J.C.C. Fan | Appl. Phys. Lett. **45**, 309 (1984) |
| 5620 | Composite $TaSi_2/n^+$ Poly-Si Formation by Rapid Thermal Annealing | D.L. Kwong*<br>R. Kwor*<br>B-Y. Tsaur | IEEE Electron Device Lett. **EDL-5**, 133 (1984) |
| 5622 | Oxygen in Zone-Melting-Recrystallized Silicon-On-Insulator Films: Its Distribution and Possible Role in Sub-Boundary Formation | J.C.C. Fan<br>B-Y. Tsaur<br>C.K. Chen<br>J.R. Dick*<br>L.L. Kazmerski* | Appl. Phys. Lett. **44**, 1086 (1984) |
| 5636 | "Thermal Fixing" of Ti-Indiffused $LiNbO_3$ Channel Waveguides for Reduced Photorefractive Susceptibility | R.A. Becker | Appl. Phys. Lett. **45**, 121 (1984) |

* Author not at Lincoln Laboratory.

| JA No. | | | |
|---|---|---|---|
| 5564 | Signal Correlation Using a One-Dimensional Electroabsorptive CCD Spatial Light Modulator | R.H. Kingston | Proc. IEEE **72**, 594 (1984) |
| 5569 | The Future of High-Efficiency Solar Cells | J.C.C. Fan | Solar Cells **12**, 51 (1984) |
| 5582 | Triple Ion Implantation Technique for Formation of Shallow npn Bipolar Transistor Structures in Silicon | B-Y. Tsaur<br>J.D. Woodhouse | Appl. Phys. Lett. **44**, 1005 (1984) |
| 5585 | Wideband Electrooptic Guided-Wave Analog-to-Digital Converters | R.A. Becker<br>C.E. Woodward<br>F.J. Leonberger<br>R.C. Williamson | Proc. IEEE **72**, 802 (1984) |
| 5590 | Low Threshold GaInAsP/InP Buried-Heterostructure Lasers with a Chemically Etched and Mass-Transported Mirror | Z.L. Liau<br>J.N. Walpole<br>D.Z. Tsang | Appl. Phys. Lett. **44**, 945 (1984) |
| 5597 | Growth and Patterning of GaAs/Ge Single-Crystal Layers on Si Substrates by Molecular Beam Epitaxy | P. Sheldon*<br>K.M. Jones*<br>R.E. Hayes*<br>B-Y. Tsaur<br>J.C.C. Fan | Appl. Phys. Lett. **45**, 274 (1984) |
| 5599 | GaAs MESFETs Fabricated on Monolithic GaAs/Si Substrates | H.K. Choi<br>B-Y. Tsaur<br>G.M. Metze<br>G.W. Turner<br>J.C.C. Fan | IEEE Electron Device Lett. **EDL-5**, 207 (1984) |
| 5603 | Multiple Waveguide Lens | H.A. Haus*<br>L. Molter-Orr*<br>F.J. Leonberger | Appl. Phys. Lett. **45**, 19 (1984) |

* Author not at Lincoln Laboratory.

# REPORTS ON SOLID STATE RESEARCH

**1 May through 31 July 1984**

## PUBLISHED REPORTS

### Journal Articles

| JA No. | | | |
|---|---|---|---|
| 5465 | Electron Devices on Piezoelectric Semiconductors: A Device Model | R.S. Withers | IEEE Trans. Sonics Ultrason. **SU-31**, 177 (1984) |
| 5522 | Broad-Band Guided-Wave Electro-optic Modulators | R.A. Becker | IEEE J. Quantum Electron. **QE-20**, 723 (1984) |
| 5535 | Topographic Imperfections in Zone-Melting-Recrystallized Si Films on $SiO_2$ | C.K. Chen<br>M.W. Geis<br>B-Y. Tsaur<br>R.L. Chapman<br>J.C.C. Fan | J. Electrochem. Soc. **131**, 1707 (1984) |
| 5538 | The Band Structure of a-Sn and Ge-Sn Alloys | S.H. Groves<br>W. Paul* | IEE Proc-I **131**, 42 (1984) |
| 5551 | Lasers, Their Development and Applications at M.I.T. Lincoln Laboratory | R.H. Rediker<br>I. Melngailis<br>A. Mooradian | IEEE J. Quantum Electron. **QE-20**, 602 (1984) |
| 5556 | Laser Microchemical Processing: Spatial Resolution and Rate Limits of Optical Direct-Writing Techniques | D.J. Ehrlich<br>J.Y. Tsao | Chapter in *Microcircuit Engineering '83* (Academic Press, New York, 1983), pp. 429-438 |
| 5561 | A Self-Aligned Dual-Grating GaAs Permeable Base Transistor | B.A. Vojak<br>R.W. McClelland<br>G.A. Lincoln<br>A.R. Calawa<br>D.C. Flanders<br>M.W. Geis | IEEE Electron Device Lett. **EDL-5**, 270 (1984) |

* Author not at Lincoln Laboratory.

## 5. ANALOG DEVICE TECHNOLOGY

A wideband programmable transversal filter has been built using a $LiNbO_3$ surface-acoustic-wave delay line and a silicon integrated circuit. An air-gap structure is used to couple the piezoelectric fields of the delay line to capacitively weighted taps on the silicon. The device, called a SAW/FET, has a 50-MHz programmable bandwidth, 175 taps, a 10-dB single-tap dynamic range, and an impulse response 1.5-$\mu$s long. The SAW delay line incorporates an edge-bonded transducer for short pedestal of delay with high feedthrough isolation and wide bandwidth.

A track-and-hold circuit based on InP optoelectronic switches has been developed for use in a wideband radar signal processor. The circuit demonstrated a 260-MHz analog bandwidth, 100-MHz sampling rate, and better than 1-percent accuracy. The switch input-to-output leakage caused by a slowly decaying residual conductance was circumvented by the use of a two-stage configuration.

Si wafer. The CMOS devices are fabricated in a zone-melting-recrystal'ized SOI film, while the bipolar devices are fabricated either in the SOI film or in epitaxial Si layers grown selectively on the Si substrate.

Smooth layers of tungsten silicide have been formed on silicon substrates by a two-step process that utilizes ion-beam mixing produced by $As^+$ ion implantation, followed by rapid thermal annealing. This process, which can be used for the selective formation of tungsten silicide on patterned $SiO_2$-coated substrates and the simultaneous formation of shallow $n^+$-$p$ junctions, should be useful for the fabrication of MOSFETs with self-aligned silicided gate, source, and drain.

As a step toward the integration of GaAs and Si devices and circuits on the same chip, monolithic GaAs/Si substrates have been prepared by using molecular beam epitaxy to grow device-quality GaAs layers directly on Si(100) wafers, without an intermediate Ge layer. These GaAs layers have been used for the fabrication of MESFETs with transconductance as high as 85 mS/mm and leakage current as low as 1 $\mu$A at $V_{gs} = -3$ V for gate dimensions of $2.0 \times 200$ $\mu$m.

The conversion efficiency of shallow-homojunction GaAs solar cells has been increased to over 22 percent (AM1, total area) by utilizing a p-GaAs/$p^+$-$Al_{0.2}Ga_{0.8}As$ heterostructure to produce an enhanced back-surface field. The incorporation of a higher bandgap material below the active region will also be useful in implementing two solar cell designs: a GaAs cell with a back-surface reflector and an AlGaAs cell that can be used as the upper cell in tandem configurations.

## 4. MICROELECTRONICS

A new CCD fabrication process for producing an overlapping gate structure has been developed. The gate separation is determined by the thickness of a dielectric film isolating adjacent gates. This process readily permits submicrometer control of gap size while using conventional optical lithography of much coarser precision.

GaAs permeable-base transistors (PBTs) have been successfully fabricated using organometallic chemical vapor deposition (OMCVD) for the critical overgrowth step. Incorporation of contaminants during overgrowth is significantly reduced compared with previous results obtained using vapor phase epitaxy (VPE). The small-signal, unity-current-gain frequency, $f_T$, of 33 GHz measured for these devices equal that of the best PBTs fabricated to date.

A comparative study of methods for the formation of low resistance ohmic contacts to p-type GaAs has been undertaken. Evaluation of several AuZn metallization techniques has been completed. Evaporated AuZn produced the lowest resistance contacts.

A technique for the etching of high-resolution structures in type IIA diamond has been developed. A $Xe^+$ beam and a reactive flux of $NO_2$ are used in an ion-beam-assisted etching system. An etching rate of 200 nm/min. has been achieved with an etching rate ratio of 20 between the diamond and an Al mask.

A planar receptor for 140-GHz radiation using two microstrip dipole antennas connected to a GaAs Schottky diode has been redesigned and constructed on a quartz substrate. Improved antenna patterns with 3-dB widths in the E- and H-planes of 48° and 68°, respectively, were measured and a heterodyne noise temperature of 4900 K (DSB) was observed. The results show that this structure could be useful as one element in a heterodyne imaging array.

# INTRODUCTION

## 1. SOLID STATE DEVICE RESEARCH

A traveling-wave Ti-indiffused $LiNbO_3$ guided-wave Mach-Zehnder interferometric modulator has been fabricated and characterized at $\lambda = 0.85$ $\mu$m. The modulator achieves the theoretical 3-dB linear small-signal bandwidth limit of 16 GHz for a 4-mm-long interaction length. With a $\pm 2.25$-V drive signal, an extinction ratio of 22 dB is achieved.

The frequency response of an optical guided-wave GaAs interferometer has been measured. The bandwidth of the interferometer biased at a null point was 2.2 GHz, limited by parasitics. A small-signal bandwidth of $\approx$3 GHz can be inferred from this measurement for the case where the interferometer is biased to a linear operating point. This is the highest bandwidth yet reported for a guided-wave GaAs modulator.

A surface-emitting GaInAsP/InP laser has been developed in which a monolithically integrated parabolic mirror is used to up-deflect the output of a buried-heterostructure laser. A threshold current as low as 12 mA and a differential quantum efficiency as high as 46 percent have been obtained.

Evidence is presented which suggests that Fe outdiffuses at an extremely rapid rate from InP. Observations were made on lightly doped InP(Fe) samples that were heated to 650° C for several minutes under an atmosphere deficient in phosphorus.

Reproducible growth of high-quality InGaAs(Fe) by LPE has been achieved by using long pregrowth bakes and a substrate transfer apparatus. A mixed conduction model is used to explain the large variation of transport properties with Fe doping. This model predicts a maximum resistivity of 2500 $\Omega$-cm, and samples with resistivities within 5 percent of this value have been grown.

## 2. QUANTUM ELECTRONICS

A LIDAR system using a Co:$MgF_2$ laser, which is continuously tunable from 1.6 to 1.9 $\mu$m, has been constructed. Preliminary remote sensing measurements of backscattered signals from atmospheric aerosols and solid targets have been made.

An antireflection-coated GaAlAs diode laser has been used to amplify 30-ps diode laser pulses. A net gain of up to 7.5 was measured and an estimated total gain of 13.6 was found by taking into account input coupling and collection losses.

Multiplication of the pulse repetition rate of a mode-locked laser beam using an all-optical technique has been used to generate microwave radiation from an avalanche photodiode as well as from an optoelectronic switch. The technique involves the use of multiple beam splitters and delay lines.

## 3. MATERIALS RESEARCH

Two merged CMOS/bipolar technologies utilizing SOI films have been developed for fabricating fully isolated CMOS devices and vertical bipolar transistors with good electrical characteristics on the same

# ORGANIZATION

## SOLID STATE DIVISION

A.L. McWhorter, *Head*
I. Melngailis, *Associate Head*
E. Stern, *Associate Head*
J.F. Goodwin, *Assistant*

P.E. Tannenwald, *Senior Staff*

### QUANTUM ELECTRONICS

A. Mooradian, *Leader*
P.L. Kelley, *Associate Leader*

Barch, W.E.
Belanger, L.J.
Brueck, S.R.J.
Burke, J.W.
Bushee, J.F., Jr.
DeFeo, W.E.
Ehrlich, D.J.
Feldman, B.
Hancock, R.C.
Harrison, J.*
Johnson, B.C.*
Killinger, D.K.
Lenth, W.
Menyuk, N.
Moulton, P.F.
Sedlacek, J.H.C.
Sharpe, K.A.
Sullivan, D.J.
Tsao, J.Y.

### ELECTRONIC MATERIALS

A.J. Strauss, *Leader*
J.C. Fan, *Associate Leader*
H.J. Zeiger, *Senior Staff*

Anderson, C.H., Jr.
Branz, H.M.*
Button, M.J.
Chapman, R.L.
Chen, C.K.
Choi, H.K.
Connors, M.K.
Delaney, E.J.
Fahey, R.E.
Finn, M.C.
Gale, R.P.
Iseler, G.W.
King, B.D.
Kolesar, D.F.
Krohn, L., Jr.
Mastromattei, E.L.
McClelland, R.W.
Metze, G.M.
Nitishin, P.M.
Pantano, J.V.
Tracy, D.M.
Tsaur, B-Y.
Turner, G.W.
Windhorn, T.H.

### APPLIED PHYSICS

R.C. Williamson, *Leader*
F.J. Leonberger, *Associate Leader*
T.C. Harman, *Senior Staff*
R.H. Kingston, *Senior Staff*
R.H. Rediker, *Senior Staff*

Becker, R.A.
Chinnock, C.B.
Cox, C.H., III
DeMeo, N.L., Jr.
Diadiuk, V.
Donnelly, J.P.
Ferrante, G.A.
Groves, S.H.
Hovey, D.L.
Johnson, L.M.
Liau, Z.L.
Lind, T.A.
McBride, W.F.
Molter-Orr, L.*
O'Donnell, F.J.
Plonko, M.C.
Reeder, R.E.
Schloss, R.P.*
Spears, D.L.
Tsang, D.Z.
Walpole, J.N.
Whitaker, N.*
Woodhouse, J.D.
Yap, D.*

---

* Research Assistant

## ANALOG DEVICE TECHNOLOGY

J.H. Cafarella, *Leader*
R.W. Ralston, *Associate Leader*
R.S. Withers, *Assistant Leader*

Anderson, A.C.
Arsenault, D.R.
Boisvert, R.R.
Bouman, C.A.
Brogan, W.T.
Delaney, M.*
Denneno, A.P.
Dolat, V.S.
Fischer, J.H.
Fitch, G.L.
Flynn, G.T.
Gottschalk, P.G.*
Green, J.B.
Hauser, E.M.
Holtham, J.H.
Kernan, W.C.
Lattes, A.L.
Macedo, E.M., Jr.
Macropoulos, W.
Marden, J.A.
Melngailis, J.†
Oates, D.E.
Reible, S.A.
Sage, J.P.
Smith, L.N.
Yao, I.

## MICROELECTRONICS

W.T. Lindley, *Leader*
N.P. Economou, *Associate Leader*
R.A. Murphy, *Assistant Leader*

Astolfi, D.K.
Bozler, C.O.
Bromley, E.I.
Burke, B.E.
Calawa, A.R.
Chen, C.L.
Chiang, A.M.
Chu, A.
Clifton, B.J.
Correa, C.A.
Daniels, P.J.
Durant, G.L.
Efremow, N.N., Jr.
Felton, B.J.
Flanders, D.C.
Geis, M.W.
Gray, R.V.
Hollis, M.A.
Johnson, K.F.
Kosicki, B.B.
Lax, B.†
LeCoz, Y.L.*
Lincoln, G.A., Jr.
Lyszczarz, T.M.
Mahoney, L.J.
Manfra, M.J.
McGonagle, W.H.
Mroczkowski, I.H.
Mountain, R.W.
Nichols, K.B.
Pang, S.W.
Parker, C.D.
Piacentini, W.J.
Pichler, H.H.
Rabe, S.
Randall, J.N.
Rathman, D.D.
Shaver, D.C.
Silversmith, D.J.
Smythe, D.L., Jr.
Sollner, T.C.L.G.
Taylor, J.A.*
Vera, A.
Wilde, R.E.

---

* Research Assistant
† Part Time

# 1. SOLID STATE DEVICE RESEARCH

## 1.1 TRAVELING-WAVE ELECTROOPTIC MODULATOR WITH MAXIMUM BANDWIDTH-LENGTH PRODUCT

Broadband electrooptic guided-wave modulators are useful in sensor, signal-processing, and fiber-optic communication systems. To achieve maximum bandwidth in an electrooptic modulator, a traveling-wave configuration is employed.[1] In this configuration, there is a maximum bandwidth-length product determined by the magnitude of the velocity difference between the co-propagating microwave and optical signals. Here we describe a packaged 4-mm-long Ti-indiffused $LiNbO_3$ traveling-wave interferometric modulator for use at $\lambda = 0.85\ \mu m$ that achieves the theoretically predicted linear small-signal 3-dB bandwidth of 16 GHz. A 22-dB extinction ratio is obtained and a measured $V_\pi$ of 4.5 V results in a voltage per unit bandwidth $V_\pi/\Delta f = 0.28$ V/GHz.

The traveling-wave Mach-Zehnder interferometric modulator that we have designed, fabricated, and characterized is shown schematically in Figure 1-1. The Ti-indiffused waveguides were fabricated by diffusing 400 Å of Ti into the X-face of $LiNbO_3$ at 1000°C for 5 h in $O_2$ bubbled through $H_2O$. The Ti-strip width before diffusion was $\approx 3.8\ \mu m$. This set of fabrication parameters yields low-loss waveguides (1 dB/cm or less) suitable for single TE- and TM-mode propagation in the Y-direction at $\lambda = 0.85\ \mu m$. After the diffusion, the crystal end faces were cut and polished to facilitate end-fire coupling. The traveling-wave

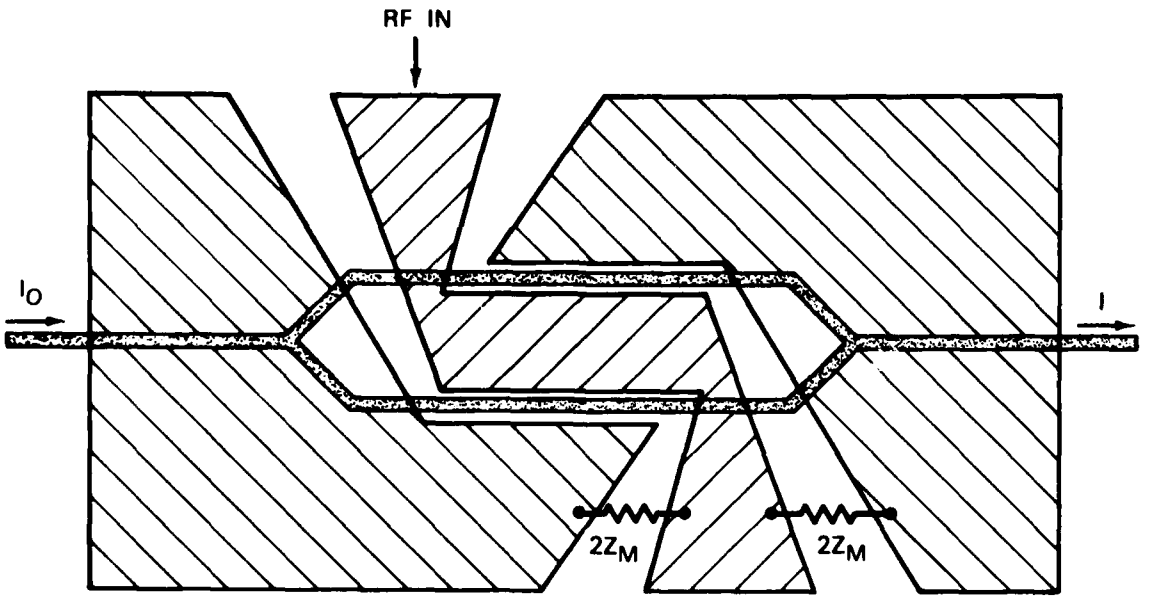


**Figure 1-1. Schematic diagram of traveling-wave Mach-Zehnder interferometric modulator.**

electrodes were fabricated on top of a 2000-Å-thick $SiO_2$ buffer layer. The center electrode was 35.5 $\mu$m wide and the electrode gap was 4 $\mu$m wide, yielding a coplanar electromagnetic waveguide with a characteristic impedance of $\approx$17 $\Omega$ (Reference 2). The electrodes, which were 2.73-$\mu$m-thick Cr/Au, were electroplated through 4-$\mu$m-thick photoresist. By adjusting both the plating-bath temperature and current, the DC resistance and the surface roughness were minimized. Figure 1-2 shows scanning-electron-microscope

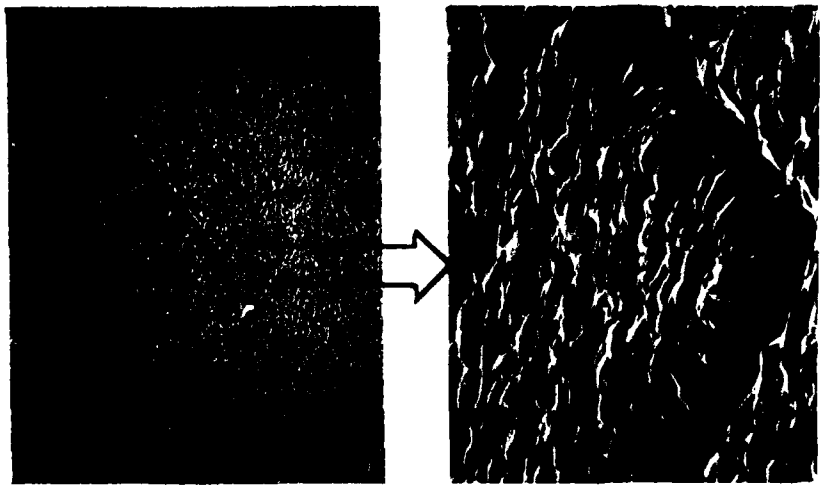

137527-S-01

**Figure 1-2. SEM photographs of traveling-wave electrode. A 500X magnification of the center electrode with the ground planes on either side (top) and a 5000X magnification of center of above photograph (bottom). The gap between electrodes is 4 $\mu$m wide.**

(SEM) photographs of the electrodes. Note that since the photoresist employed was thicker than the plated Au, there is no lateral spreading of the electrodes. The end-to-end resistance of the 4-mm-long, 35.5-$\mu$m-wide center electrode was 0.9 $\Omega$, yielding a resistivity $\rho \approx 2.18 \times 10^{-6}$ $\Omega$-cm, very close to that of bulk Au.

Four features of the device and its packaging are crucial. First, thick well-defined very-high-conductivity Au electrodes are necessary to achieve maximum performance. Several

other devices with thinner and/or lower-conductivity electrodes were seen to substantially decrease performance, as was expected.[3] Second, because coplanar electromagnetic waveguides are known to support higher-order modes and because these modes occur at lower frequencies for thicker substrates,[2] $LiNbO_3$ 250-$\mu$m thick was used for these devices. This is just thick enough to allow reliable handling without breakage. Third, again to insure that no higher-order modes propagated, other ground planes were kept several millimeters away from the top and bottom of the $LiNbO_3$ crystal. And fourth, the modulator electrodes are terminated on chip in their characteristic impedance. Failure to properly terminate results in either a peaked or a reduced bandwidth response.[3]

The device was first tested at low frequencies. A 4.5-V drive signal ($V_\pi$) was seen to drive the modulator from its maximum to its minimum point. Subsequent measurements indicated that the extinction ratio $-10 \log (I_{min}/I_{max})$ was 22 dB.

The wideband characteristics of the modulator were measured by means of the linear small-signal swept-frequency technique.[4] This is an important measurement technique because it provides a consistent and easily interpretable determination of bandwidth.

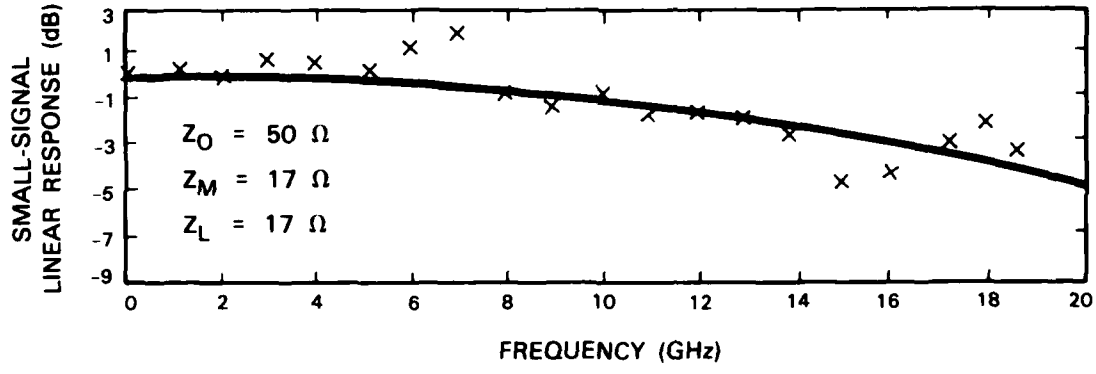


138225-N-01

**Figure 1-3. Linear small-signal frequency response of traveling-wave modulator. Measured response is shown by X points and theoretically predicted response is shown by solid line.**

The results of the swept-frequency measurements and the predicted response, after Kubota *et al.*,[3] are shown in Figure 1-3. Here we see that the modulator has a linear small-signal 3-dB bandwidth of 16 GHz. Near 7 and 15 GHz, there are small deviations from the predicted response, probably due to the packaging. Although the data are shown for 1-GHz increments, they were taken continuously. All the data points shown can be connected by smooth curves. These data are in excellent agreement with theoretically predicted results for a 16-GHz modulator.

R. A. Becker

## 1.2 FREQUENCY RESPONSE OF A GaAs GUIDED-WAVE ELECTROOPTIC INTERFEROMETER MODULATOR

We have recently reported a GaAs guided-wave electrooptic interferometric modulator.[5] These devices have the potential of being integrated with lasers for both high-speed analog and digital modulation. In this section, the frequency response of these interferometers is reported.

As shown in Figure 1-4, the interferometer structure consists of a three-guide coupler[6-8] input section, the two active arms of the interferometer, and a three-guide coupler output section. The three-guide couplers consist of three closely spaced single-mode $n^-$-$n^+$ slab-coupled waveguides,[9] while the two active arms are single-mode $p^+$-$n^-$-$n^+$ slab-coupled waveguides.[10] The input three-guide coupler acts as a power divider. Power input into the center guide is divided equally between the two outside guides in a coupling length, $L_C$. The output three-guide coupler acts as a power combiner. For power input into the two outside guides, the in-phase components of the two inputs are combined in the center guide in a length, $L_C$, while the out-of-phase components remain in the outside guide. The effective index in the active arms may be changed via the electrooptic effect by changing the bias on the p-n junctions. The phase of the output of either or both arms of the interferometer may therefore be changed, resulting in modulation of the signal out of the center guide of the output three-guide coupler.

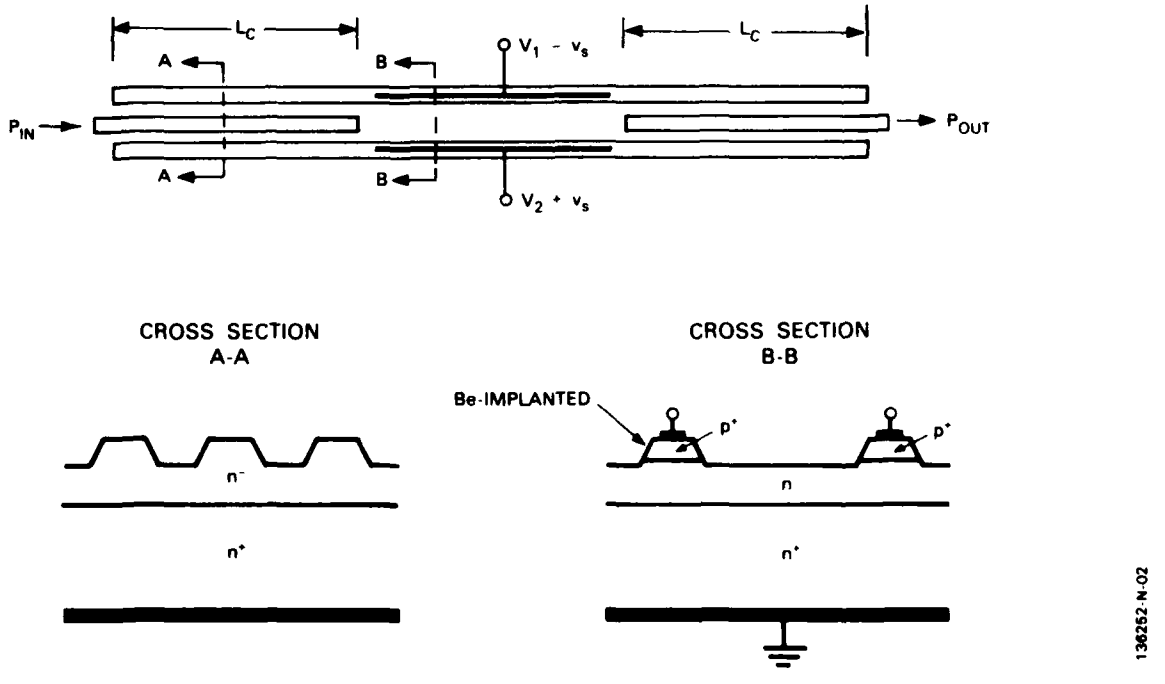


**Figure 1-4. Schematic illustration of GaAs electrooptic interferometric modulator.**

The actual interferometers were fabricated on a GaAs wafer consisting of an unintentionally doped $n^-$-epilayer ($n \leqslant 5 \times 10^{15}\ cm^{-3}$) grown on an $n^+$-substrate ($n \approx 2 \times 10^{18}\ cm^{-3}$) oriented 5° off the $\{100\}$. A multi-energy Be implant[11] was used to form the $p^+$-region. Following implantation annealing, the rib-waveguide interferometer structure was etched using a Ti-etch mask. A $SiO_2$ layer was then deposited and ohmic contacts applied to the $p^+$-ribs and the back of the $n^+$-substrate. In these experiments, the length of the output three-guide coupler was determined by cleaving instead of photolithographically so that the output of all three guides could be observed. Additional information on the fabrication procedure can be found in Reference 5.

To test the interferometer, radiation from a single-mode GaInAsP/InP double-heterojunction laser operating at 1.3 $\mu$m was end-fired coupled into the center guide of the input three-guide coupler. The electric field of the input light was polarized parallel to the plane of the slab.

The output of a recently fabricated interferometer with 2-mm-long active arms biased for maximum and minimum output in the center guide is shown in Figures 1-5(a) and (b), respectively. The output is more symmetric and the extinction ratio is higher than obtained on initial devices.[5] Maximum output in the center guide is not obtained with the same bias (typically zero) on both arms because of a built-in optical phase difference (of about 25°)

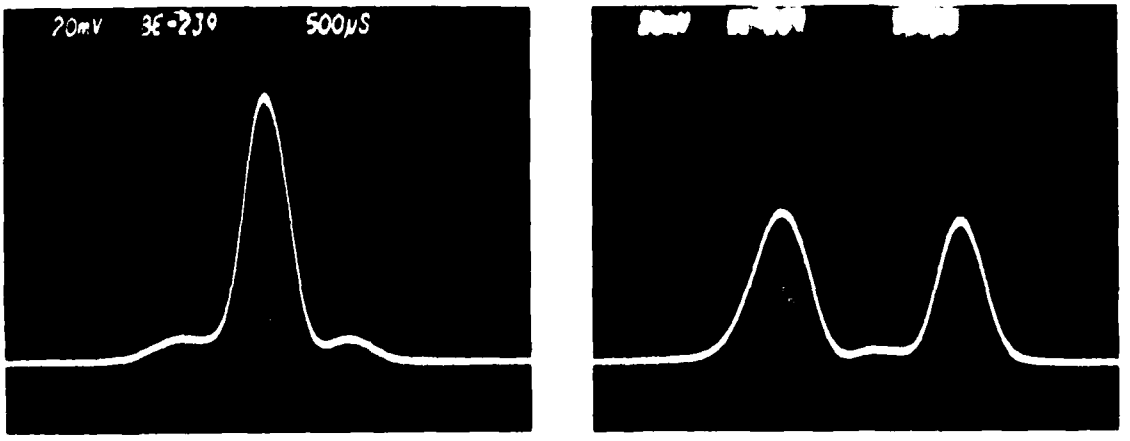


138996-R

**Figure 1-5. Scanned output of interferometer: (a) biased for a maximum output in the center guide, and (b) biased for a minimum output in the center guide.**

between the two arms. The output three-guide coupler is slightly shorter than a coupling length, resulting in a small amount of power remaining in the outside guides when the interferometer is biased for maximum output in the center guides. When biased for minimum output in the center guide, about 1.5 percent of the power remained in the center guide for an extinction ratio of ≈18 dB.

Swept-frequency measurements[4] were used to determine the frequency response of the above interferometer. For these measurements, the interferometer was biased by means of a bias "T" to a $V_\pi$ point, i.e., a point at which there is a minimum in the output of the center guide, and a swept high-frequency signal modulated by a 2-kHz square wave was applied to one arm of the interferometer. The output of the center guide was detected by a photodiode and a lock-in amplifier referenced to the 2-kHz square wave used to obtain a high signal-to-noise ratio output signal. The frequency response obtained from these measurements corresponds to the electrical response of the interferometer electrode structure. As shown in Figure 1-6, the measured 3-dB electrical bandwidth of the interferometer

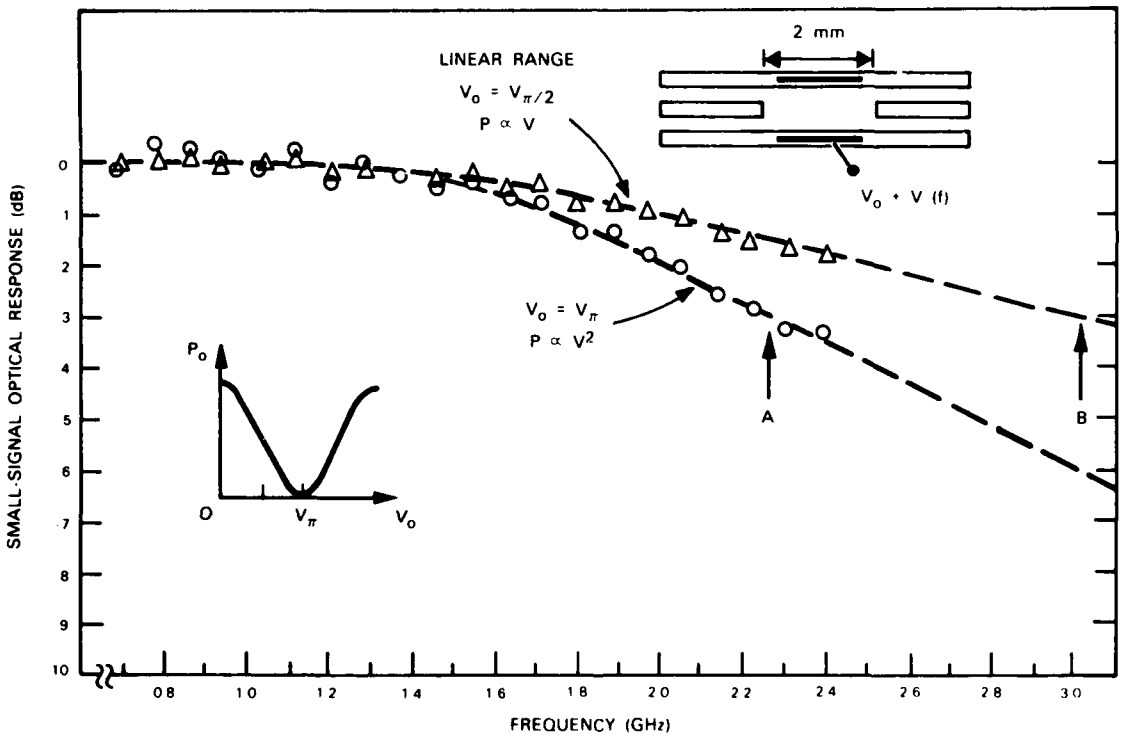


**Figure 1-6. Frequency response of interferometers obtained from swept-frequency measurements: (○) optical response obtained with interferometer biased at a $V_p$ point; (△) square root of above when biased at a linear optical response point $V_\pi/2$. The electrical bandwidth of the interferometer electrode structure is ≈2.2 GHz (point A), which translates into a linear optical bandwidth of ≈3.0 GHz (point B).**

(point A) is ≈2.2 GHz. Because the transfer function of the interferometer with applied bias is nonlinear, the electrical-to-optical small-signal response depends on the bias point. If the interferometer is biased to operate in the linear optical range, i.e., a $V_\pi/2$ point, the optical response is equal to the square root of that obtained from the swept-frequency measurements at a $V_\pi$ point. The square root of the electrical response is therefore also plotted in Figure 1-6 and indicates a linear optical bandwidth (point B) of 3.0 GHz.

The bandwidth of these interferometers is currently limited by parasitics. The major limiting parasitic is the resistance of the long narrow metal contacts on top of the $p^+$-ribs. The end-to-end resistance of the metallization on the device measured is ≈60 Ω. This high resistance means that the active arm electrode must be treated as a lossy transmission line or distributed RC circuit. In addition, the bonding pads, which run out over the $SiO_2$ insulating layer, add a parasitic capacitance of ≈0.25 pF. It should be possible to significantly reduce both of these parameters by modifications in the fabrication procedures so that the linear optical bandwidth of an interferometer with 2-mm-long active arms should increase toward the calculated maximum in a 50-Ω system, namely ≈12 GHz; here transit time limitations also become important.

J.P. Donnelly G.A. Ferrante
N.L. DeMeo K.B. Nichols

## 1.3 A SURFACE-EMITTING GaInAsP/InP LASER WITH LOW THRESHOLD CURRENT AND HIGH EFFICIENCY

Surface-emitting diode lasers are of considerable interest for a variety of new applications such as monolithic two-dimensional arrays and optical interconnects for integrated circuits. However, results reported to date[12,13] have had a variety of difficulties. In this work, a new approach is introduced that has resulted in a surface-emitting GaInAsP/InP laser with performance comparable to the best of the conventional edge-emitting ones.

As illustrated in Figure 1-7, the surface emission is achieved by adding a 45° mirror to a previously developed buried-heterostructure laser with "transported" mirrors.[14] As shown in Figure 1-8, the 45° mirror is fabricated at the same time as the transported mirror by partially removing the phosphosilicate glass (PSG) mask during the selective chemical etching procedure[14] such that a stair-structure is formed and subsequently mass-transported. By designing the stair-structure such that regions I, II, III, and IV in Figure 1-8(c) have equal areas, the resulting mirror profile can approximate a portion of a parabola and can therefore reduce the laser beam divergence. It can be verified directly by integration that the equal-area requirement is fulfilled to within a few percent by choosing

$$t_1 = \left(2 + \frac{8}{3}\epsilon - \frac{8}{9}\epsilon^2\right)\sigma$$

$$t_2 = \left(2 - \frac{4}{3}\epsilon - \frac{32}{9}\epsilon^2 - \frac{64}{9}\epsilon^3\right)\sigma$$

and

$$s = (2 + \frac{2}{3}\epsilon + \frac{4}{9}\epsilon^2)\,\sigma \quad ,$$

where $t_1$, $t_2$, s, $\sigma$, and a are defined in Figure 1-8 and $\epsilon \equiv \sigma/2a$. [The parabola shown as a dotted curve in Figure 1-8(c) can be expressed as $y = x^2/2a$.] To fully collect the diverging laser output and to achieve a narrow diffraction-limited beam, larger parabolic mirrors are desired but necessitate higher mass-transport temperatures. For example, 715°C was needed to fully smooth the parabolic mirror in Wafer 685 with $t_1 \simeq 2.7$ $\mu$m, $t_2 \simeq 2.2$ $\mu$m, and $s \simeq 2.5$ $\mu$m. Figure 1-9 shows a scanning-electron micrograph of a cross-sectional view of an approximately parabolic mirror and a transported mirror [**cf.** Figure 1-8(c)].

The wafer is then metallized by using the previously described procedure,[14,15] except that, instead of sputtering, the Ti and Au layers are deposited by using angle evaporations in order to avoid coating the front laser mirror (the one facing the parabolic mirror). Note that the laser resonator as shown in Figure 1-7 consists of two transported mirrors, and no cleaved mirror is used. After metallization, the rear mirror is coated by PSG/Au layers, while the front one is only covered by the PSG of an estimated 0.17 $\mu$m thickness.

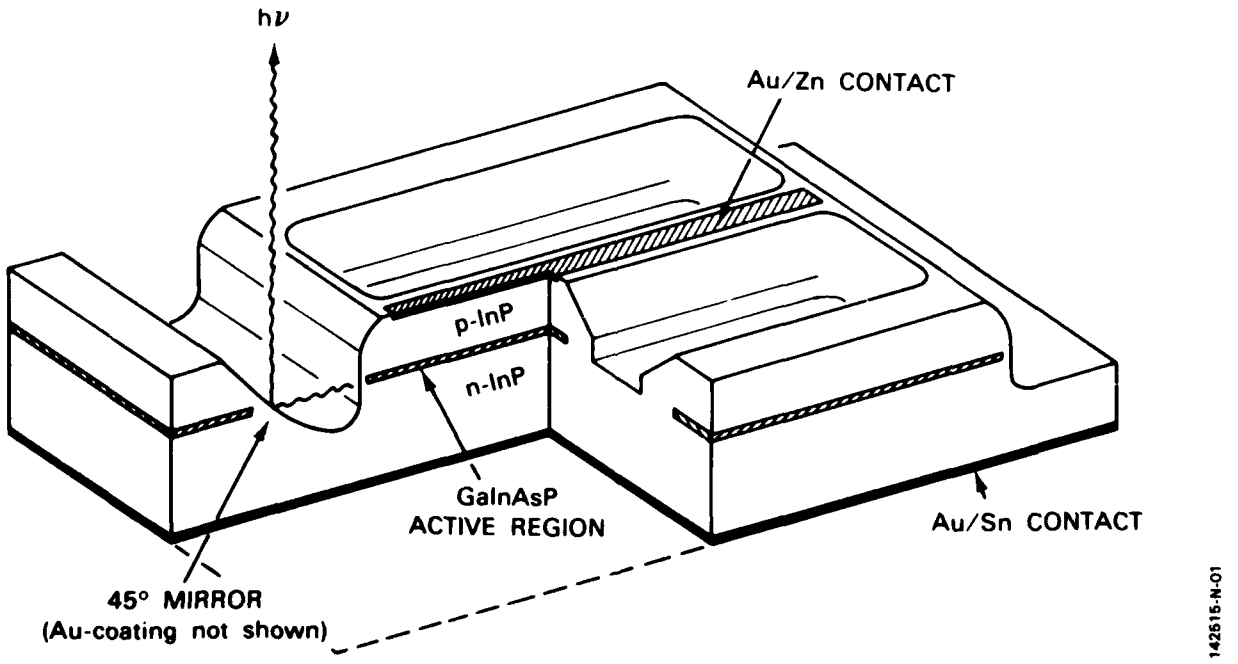


**Figure 1-7. A schematic cutaway view of the surface-emitting GaInAsP/InP laser. The surface emission is achieved by adding a 45° mirror to a previously developed buried-heterostructure laser with transported mirrors.**

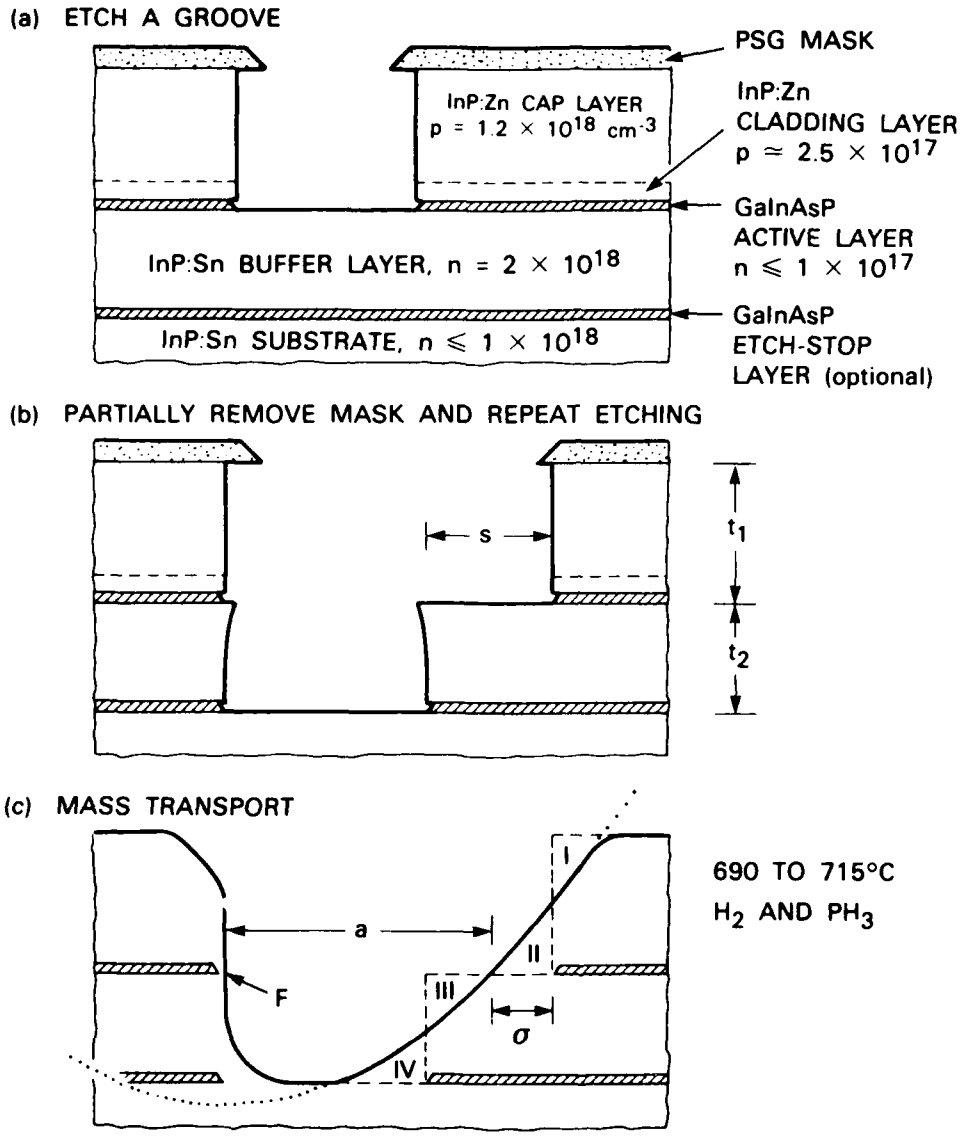


142791-N-01

**Figure 1-8. Simultaneous fabrication of the 45° (parabolic) and the transported mirrors. The dotted curve is a parabola with its focus at point F.**

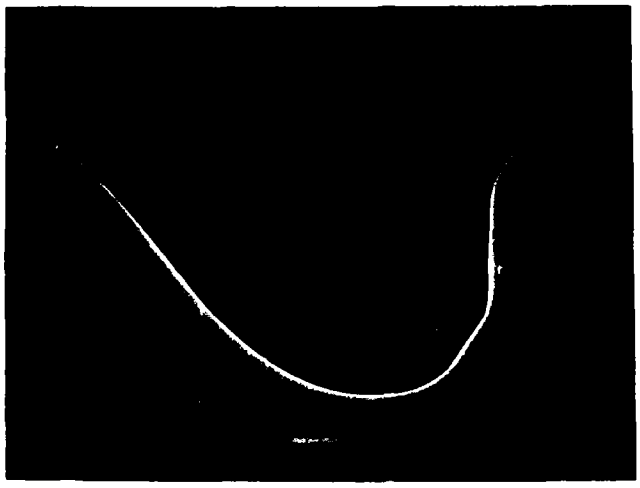

143640-S

*Figure 1-9. SEM photograph of an approximately parabolic mirror (left) and a transported mirror (right). [cf. Figure 1-8(c)].*

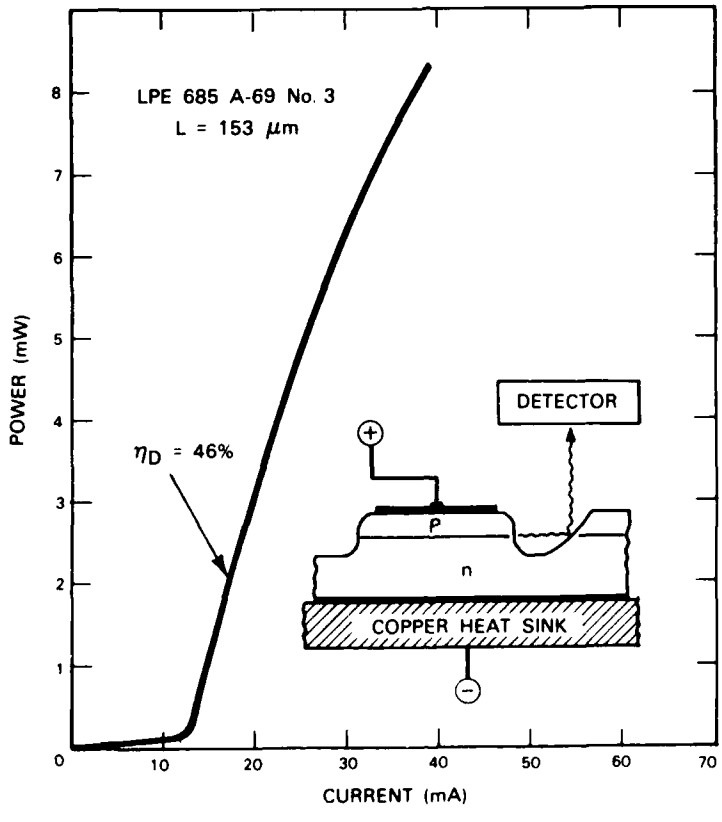


142253-N-03

**Figure 1-10. Light output vs current characteristic of a surface-emitting GaInAsP/InP laser. The laser is mounted p-side up on a copper heat sink as shown in the insert.**

Surface-emitting lasers with low threshold current and high efficiency have been obtained with good yield. For example, 70 percent of the 26 devices tested (without preselection) from Wafer 685 showed pulsed threshold currents of 12 to 18 mA. Figure 1-10 shows a CW light-current characteristic with a threshold current of 12 mA and an initial differential quantum efficiency of 46 percent. A typical far-field pattern is shown in Figure 1-11, in which a narrow beam (15° angular width for the main lobe) nearly perpendicular to the substrate surface is demonstrated. Other tested devices show angular widths as small as 12°, which is considerably narrower than the corresponding far-field patterns (typically $\geqslant$30°) of the conventional edge-emitting lasers[16-20] and is close to the diffraction-limited angular width estimated from the present parabolic mirror size.

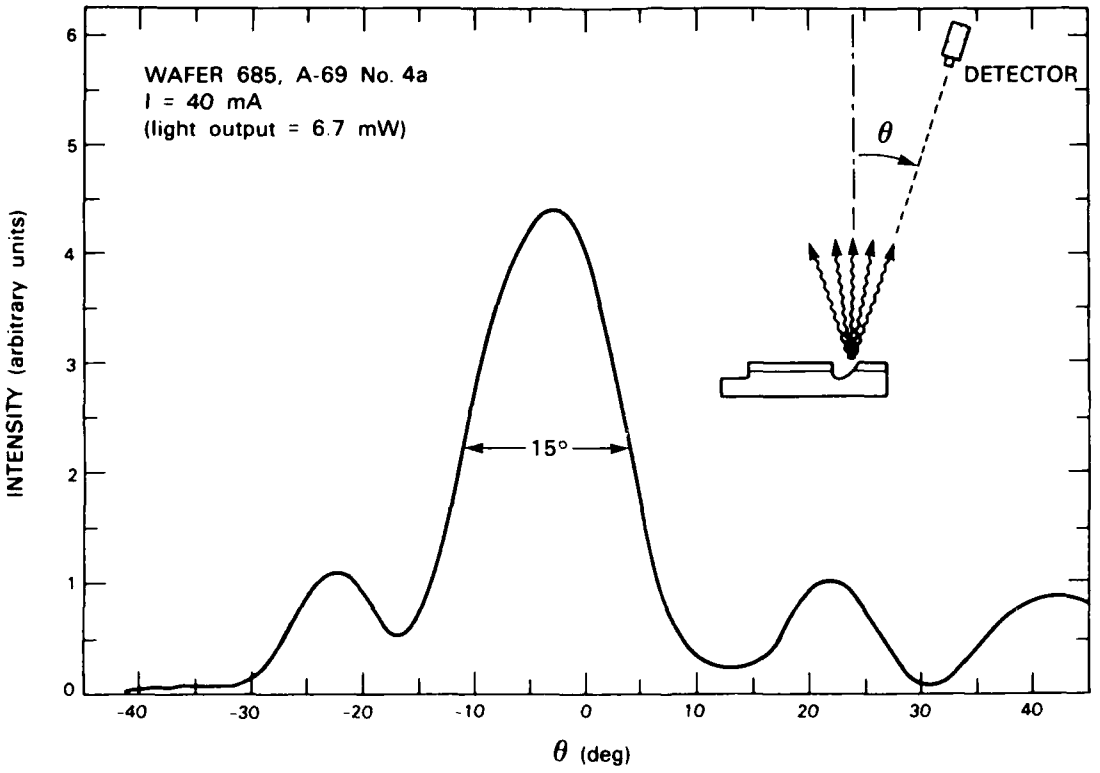


**Figure 1-11. Far-field pattern of a surface-emitting GaInAsP/InP laser.**

In conclusion, a high-performance surface-emitting GaInAsP/InP diode laser has been developed which is very promising for a variety of new applications in integrated optoelectronics.

Z.L. Liau
J.N. Walpole

## 1.4 EXTREMELY RAPID OUTDIFFUSION OF Fe FROM InP

Iron accumulation at the surface of InP(Fe) samples that occurs during heat treatments that are typical of epitaxial growth, diffusion, and annealing has been studied by several workers.[21-24] A depletion region under the accumulated surface is usually found to extend approximately 1 $\mu$m into the sample, although it has appeared that the amount of Fe from the depleted region cannot account for the amount of Fe accumulated at the surface. More recently, a phenomenon of extremely rapid outdiffusion of n-type dopants, with a depleted region 10s to 100s of micrometers deep, has been found to occur when heating takes place under an atmosphere deficient in phosphorus.[25,26] When the dopant was p-type or was Fe, the effect could not be detected by chemical staining or cathodoluminescence.

Here we report observations suggesting that this effect of extremely rapid outdiffusion does indeed occur with Fe. In Figure 1-12, the right-hand side shows a Nomarski contrast photomicrograph of a cross section of InGaAs grown on a semi-insulating InP(Fe) substrate. The cleaved surface has been chemically stained with $KOH:K_3Fe(CN)_6$. At the left is the same cross section, again under Nomarski, but at lower magnification and showing the full thickness of the substrate. Under the lower magnification, weak lines are seen to run parallel to and $\approx$30 $\mu$m from both front and back surfaces of the substrate. Electrical tests show that this region is conducting and is n-type. It has formed during a 5 to 10-min. exposure of the substrate to an $H_2$ ambient at $\approx$650°C prior to growth in the substrate-transfer apparatus described in Section 1.5. (The region of Fe accumulation is removed by

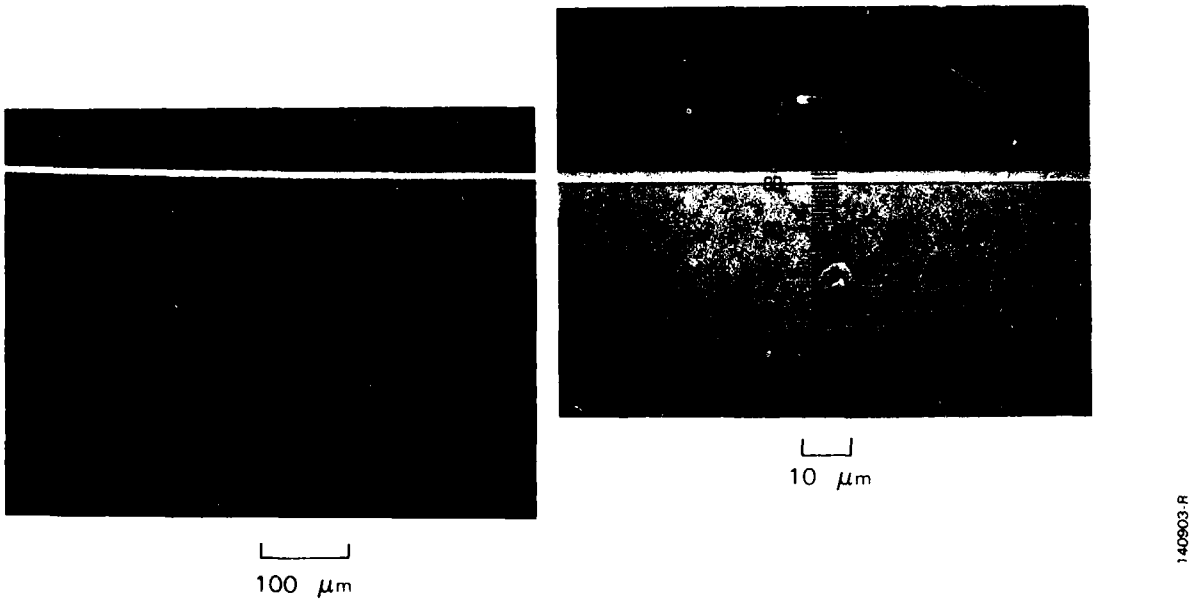


**Figure 1-12. Photomicrographs of cleaved and stained cross section under Nomarski contrast. Right: approximately 600X magnification showing epitaxial growth ($\approx$3 $\mu$m thick); left: approximately 150X magnification showing full thickness of substrate. Weak lines $\approx$30 $\mu$m from top and bottom surface occur at transition from conducting to semi-insulating regions.**

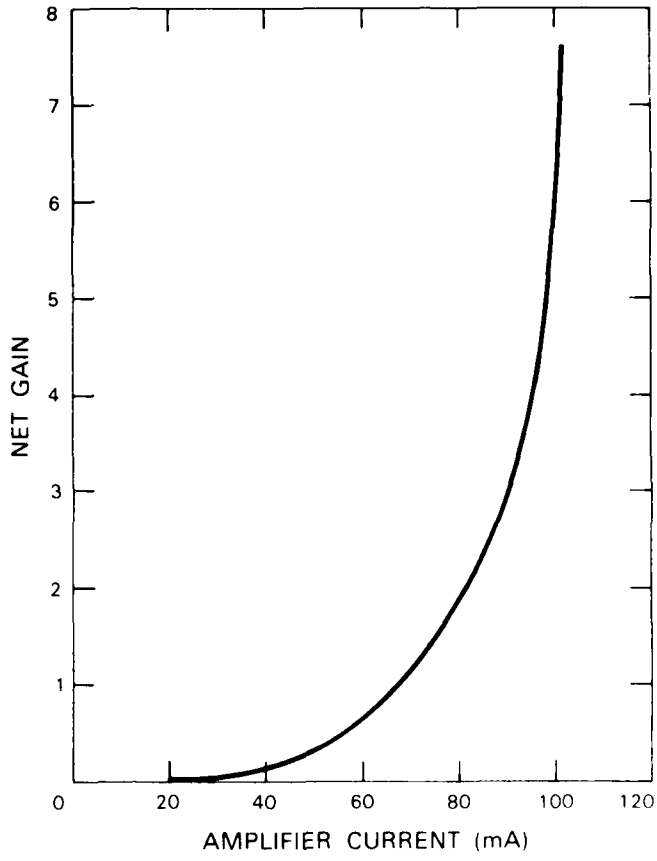


142781-N-02

**Figure 2-7. Net gain as function of amplifier injection current.**

The picosecond diode laser amplifier can be operated as a gated amplifier by driving it with a modulated injection current. The bottom trace in Figure 2-8 shows that the amplifier output is zero at zero bias current. The middle trace shows the amplifier output when a DC current of 90 mA is injected in the amplifier. The top trace shows the amplifier output when short current pulses with a repetition rate of 500 MHz are used to selectively amplify every other pulse of the incident 1-GHz pulse train. Figure 2-8 suggests that the diode laser amplifier can be used as a switching device and a mixer.

W. Lenth

## 2.3 USE OF SPATIAL TIME-DIVISION REPETITION RATE MULTIPLICATION OF MODE-LOCKED LASER PULSES TO GENERATE MICROWAVE RADIATION FROM OPTOELECTRONIC SWITCHES

An all-optical technique has been demonstrated which can substantially increase the pulse repetition rate of the output from any pulsed or mode-locked laser. Multiplication of the repetition rate by a factor of 16 has been demonstrated. A mode-locked laser pulse

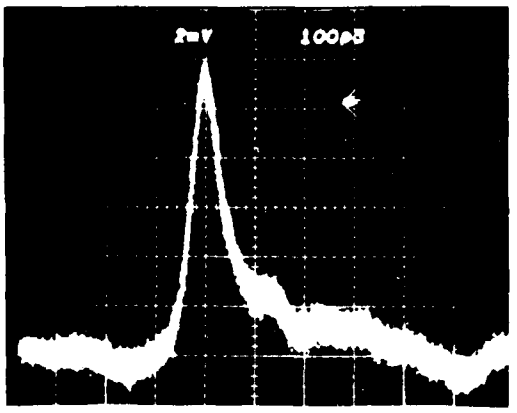

INPUT PULSE

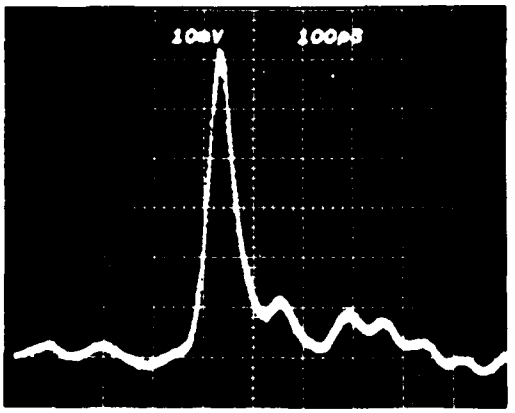

OUTPUT PULSE
AMPLIFIER CURRENT: 100 mA

**Figure 2-6. (a) Unamplified pulse from comb-generator-driven GaAlAs diode laser. Average laser power 1 mW, repetition rate 1 GHz. (b) Amplified diode laser pulse at an amplifier current i = 100 mA.**

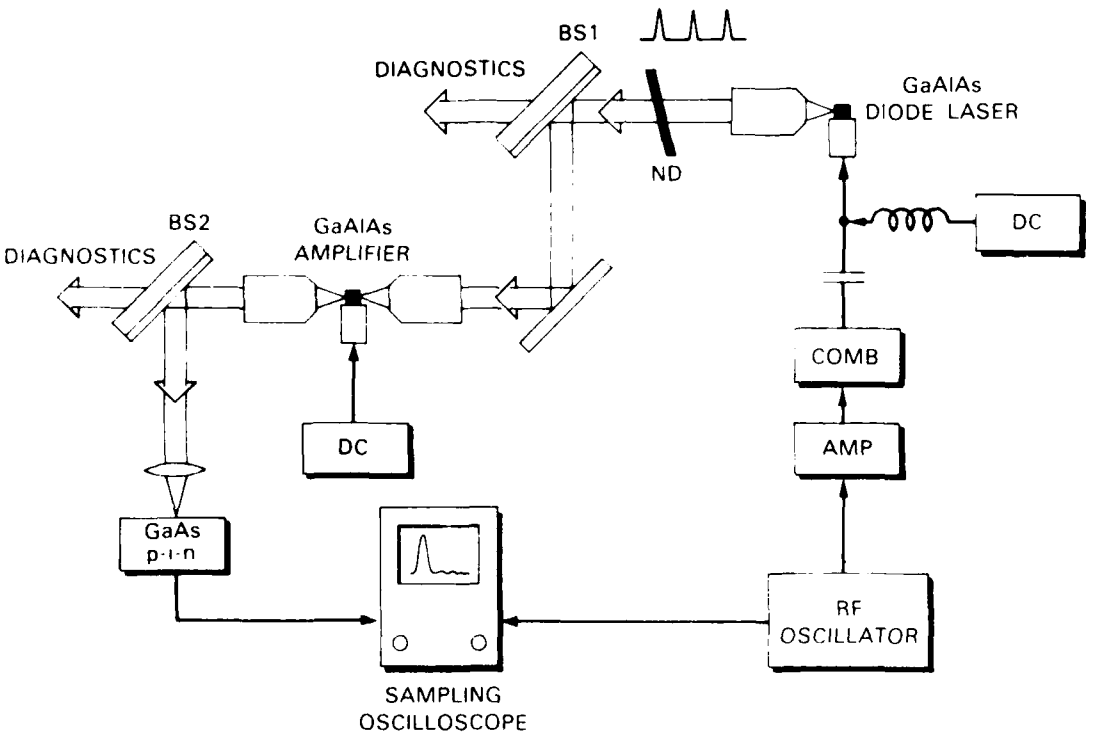


**Figure 2-5. Schematic illustration of experimental arrangement.**

the pulse. Figure 2-6(b) shows the amplifier output with an injection current of 100 mA; the net gain obtained is 6. For a systematic measurement of the net gain as a function of the amplifier current, it is necessary to measure the input and output power simultaneously. The high-speed photodiode and the sampling oscilloscope did not have the sensitivity to measure the power of the amplifier input and output pulses over a wide range of amplifier injection currents. Instead, we have used a large-area Si photodiode to record the average input and output power. A mechanical light chopper was placed between the diode laser and the amplifier in order to discriminate amplified laser radiation from spontaneous emission from the amplifier. Figure 2-7 shows the net gain as a function of the amplifier injection current. The highest net gain observed was 7.5 at $i_{DC}$ = 101 mA. The combined coupling and collection losses for the amplifier input and output are approximately 45 percent; i.e., the actual gain of the device was 13.6. The average power of the pulse train that was focused onto the amplifer front facet was 0.1 mW, which corresponds to a pulse energy of 0.1 pJ. The gain was found to start saturating at an average input power of 0.25 mW and was down -3 dB at 2.5 mW. The gain saturation was independent of amplifier injection current.

Figure 2-4 corresponds to a 50-ns time period, and each curve represents an average over 25 laser pulses. In general, aerosol returns have been observed over ranges to slightly over 1 km, depending upon atmospheric visibility.

N. Menyuk
D.K. Killinger
S. Lovold*
P. F. Moulton
A. Mooradian

## 2.2 PICOSECOND GaAlAs DIODE LASER AMPLIFIER

Very high data rate optical communication systems may require optical amplifiers of high bandwidth in order to regenerate the optically encoded information after long-distance fiber interconnects. We have studied the amplification of picosecond laser pulses using an antireflection-coated GaAlAs laser diode as an amplifier. The experimental arrangement is schematically illustrated in Figure 2-5. A channeled-substrate-planar (CSP) GaAlAs laser diode was driven with the 80-ps current pulses of a comb generator to produce 30-ps laser pulses at a repetition rate of 1 GHz. A weak DC current which was lower than the threshold current for CW lasing was superposed on the current pulses so that the average laser power was a few milliwatts. Practically all of this power was contained in the optical pulse train with no significant CW contribution. The laser pulses were coupled into the waveguide region of an antireflection-coated CSP GaAlAs diode laser amplifier. This diode was mounted on a package that permitted optical access to both facets. The amplifier output was collimated with a microscope objective identical to the one used to focus the input light on the front facet. This objective permitted collection of 74 percent of the total output power. The input coupling efficiency of this microscope objective was assumed to be also 74 percent. Using a beam splitter (see Figure 2-5), the temporal and spectral characteristics of the incident laser pulses and the amplifier output pulses could be monitored simultaneously. A DC current was applied to the amplifer. A high-speed GaAs p-i-n photodiode and a sampling oscilloscope were used to detect the laser pulses. In order to achieve maximum gain, the wavelength of the diode laser output was tuned to the maximum of the amplifier gain curve by means of temperature control. During most of the experiments, neutral density filters of at least 15-dB attenuation were placed between the oscillator and the amplifier diode in order to avoid external cavity operation of the amplifier diode. Even at the highest amplifier injection currents, the output showed no evidence of feedback from the amplifier.

Figure 2-6 gives a direct comparison of an amplifier input and output pulse. The incident pulse was recorded by removing the coupling and collimating lenses and the amplifier from the beam path. The observed pulse duration corresponds primarily to the time resolution of the detection system; however, there are some reflections at the tail of

* Norwegian Defense Research Establishment, Kjeller, Norway

backscattered from a hillside 6.7 km from the laboratory as a function of wavelength. The frequency scan covers approximately 5 $cm^{-1}$, and all the major absorption regions shown can be identified with known water vapor absorption lines. While more than one absorption line is involved in most of the absorption regions, the absorption near 1.769 $\mu$m arises primarily from a single absorption line. The observed linewidth of about 0.2 $cm^{-1}$ is consistent with a laser linewidth of 0.15 $cm^{-1}$. Differences between observed and predicted absorption levels can be understood on the basis of the finite laser bandwidth.*

We have also scanned spectral regions which include absorption bands of HCl and $CH_4$ (methane), simultaneously measuring both LIDAR return signals from a hillside 3 km distant and the transmittance of the portion of the laser beam passing through the laboratory absorption cell containing a known concentration of either HCl or $CH_4$. While no HCl or $CH_4$ was observed in the atmosphere, the laboratory absorption cell measurements yielded absorption coefficients of 0.6 $(cm\text{-}atm)^{-1}$ for the 1.7525-$\mu$m R(1) line of the 2-0 band of HCl and 0.036 $(cm\text{-}atm)^{-1}$ for the 1.6713-$\mu$m P(2) absorption line of the $2\upsilon_3$ band of $CH_4$. These results indicate that HCl column content concentrations well below a part per million should be observable at ranges up to 10 km with this system; correspondingly, a range-resolved concentration sensitivity of a few parts per million at ranges slightly over a kilometer may be expected. The concentration detection sensitivity of methane will be over an order of magnitude smaller than that of HCl. However, one should be able to measure concentrations of 10 to 100 parts per million, which should be useful for measuring gas leaks.

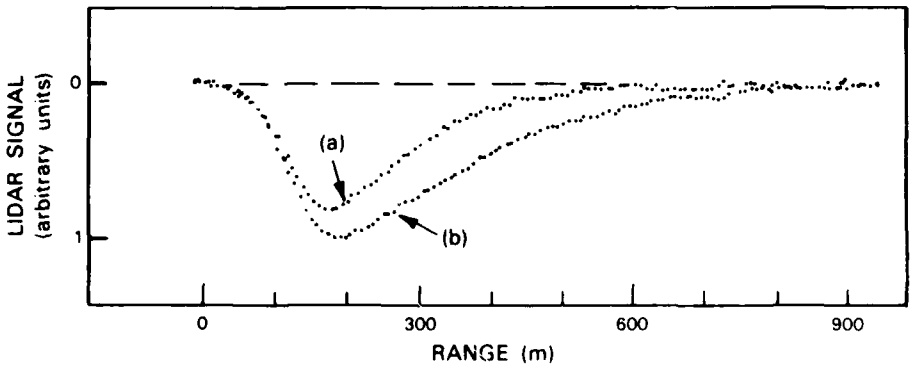


140755-N-02

**Figure 2-4. Range-resolved LIDAR signals backscattered from aerosols (a) at water vapor absorption frequency and (b) off-resonance. (Energy/pulse = 5 mJ).**

Preliminary range-resolved measurements of LIDAR signals backscattered from aerosols have been made, as shown in Figure 2-4. The figure represents an overlay of two sets of data. One set was obtained with the laser frequency coincident with a water vapor line near 1.75 $\mu$m, with the second set off-resonance. The difference between the two sets represents a measure of the water vapor content of the atmosphere as a function of range. Each dot in

* C. Cahen and G. Megie, J. Quant. Spectros. Radiat. Transfer 25, 151 (1981).

With the single set of cavity mirrors described above, continuous tuning between 1.6 and 1.9 $\mu$m has been obtained. The resulting Co:$MgF_2$ laser pulse length is approximately 300 ns with a 0.15 $cm^{-1}$ bandwidth. Output energies near 50 mJ have been obtained in the free-running mode; however, possible damage to the dichroic cavity mirror has limited operation to about 10 to 15 mJ when operating in the Q-switched mode.

The LIDAR system, including the Co:$MgF_2$ laser cavity, is shown in Figure 2-2. Although most of the laser output is used for remote sensing, portions of the output are used to provide diagnostics. In particular, a room-temperature HgCdTe detector monitors the output of each pulse and provides an optical trigger to various electronic components, and the absorption cell shown in the figure permits laboratory determination of the molecules being detected. The spectrometer monitors the laser frequency at a particular position; however, when the laser is used in a continuous frequency scanning mode, the spectrometer is used as a spectrograph, with the output imaged on a 64-element pyroelectric detector array with 100-$\mu$m spacing of the individual elements. This arrangement permits visual observation in real time of the laser spectral output over a range of about 25 $cm^{-1}$ and ensures that the laser output is single mode and that the frequency is continuously tuned over the free spectral range of the etalon.

The LIDAR portion of the laser output beam is expanded to a diameter of about 3 cm and directed to the target with a 50-cm beam-steering mirror. The return beam is sent through a 60-cm Cassegrain telescope onto an InSb detector. The signal is then sent to a waveform digitizer and computer for signal processing.

Preliminary measurements have been obtained with this system. These have included both column-content measurements using backscattered returns from topographic targets, and range-resolved returns from aerosols. Figure 2-3 shows a computer output of LIDAR signals

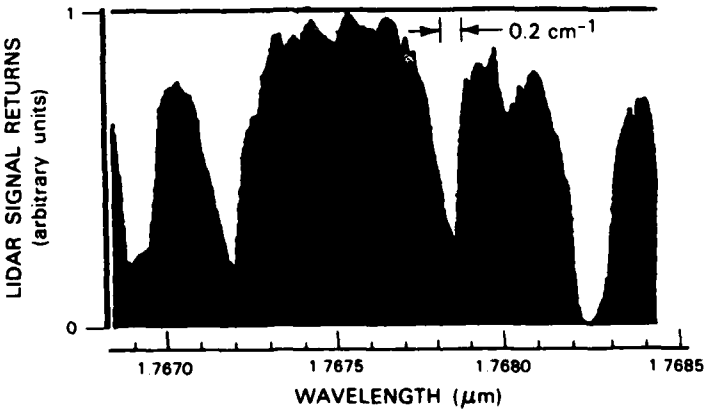


140758-N

**Figure 2-3. Frequency scan of LIDAR signal returns from foliage on hillside at a range of 6.7 km.**

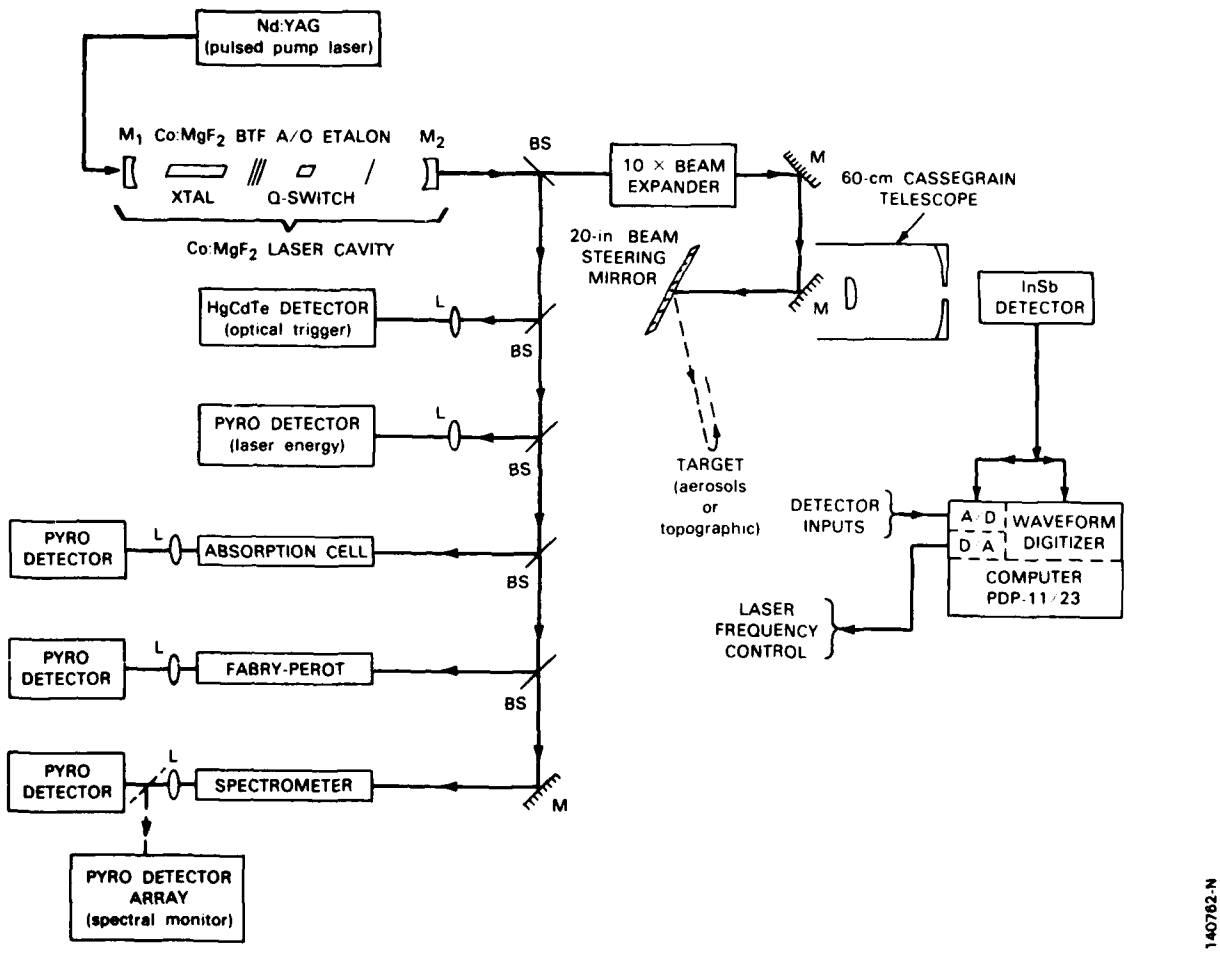


**Figure 2-2. Co:$MgF_2$ LIDAR system.**

# 2. QUANTUM ELECTRONICS

## 2.1 CONTINUOUSLY TUNABLE INFRARED LIDAR SYSTEM USING A Co:$MgF_2$ LASER

A LIDAR system for the remote sensing of atmospheric species which uses a continuously tunable Co:$MgF_2$ laser as the radiation source has been constructed, and preliminary measurements have been made with this system.

The Co:$MgF_2$ laser has been found to be continuously tunable between 1.5 and 2.3 $\mu$m.* However, to be effective as a remote sensing LIDAR source, it is necessary that the Co:$MgF_2$ laser also be pulse pumped, Q-switched, and have a reasonably narrow linewidth. The laser cavity designed to meet these criteria is shown in Figure 2-1, which also includes the Nd:YAG pump source radiating at 1.32 $\mu$m.

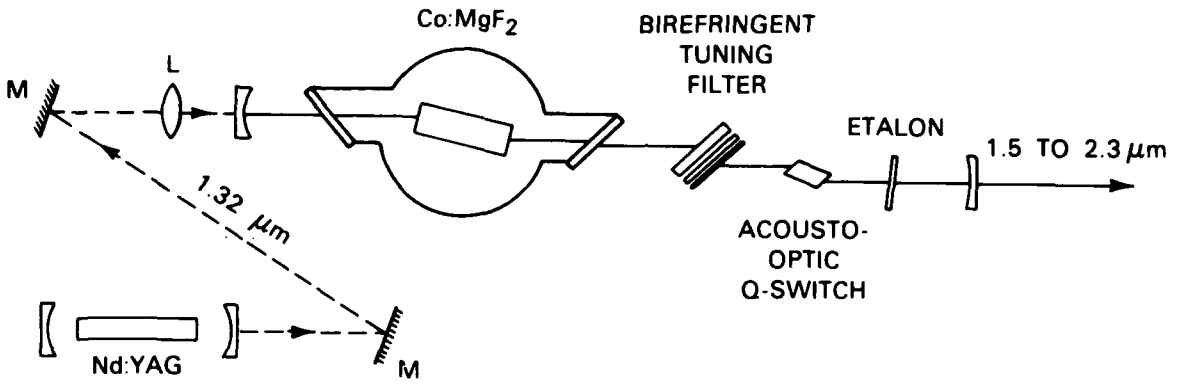


140760-N-01

**Figure 2-1. Optically pumped Co:$MgF_2$ laser used in the remote sensing LIDAR system.**

The Co:$MgF_2$ laser cavity is 70 cm long. One end of the cavity consists of a dichroic mirror with high transmittance at 1.32 $\mu$m and high reflectivity at 1.7 $\mu$m; the other end of the cavity is an output coupling mirror that is about 95 percent reflecting at 1.7 $\mu$m. The Nd:YAG pump laser pulses with 400 mJ energy and ~1 ms pulse length are focused onto a Co:$MgF_2$ crystal cut at the Brewster angle and located in a liquid nitrogen dewar. An optoacoustic modulator is used to obtain the energy in a single Q-switched pulse. Tuning is accomplished through the use of a three-element birefringent filter† in conjunction with a 0.25-mm quartz etalon.

---

* P.F. Moulton, IEEE J. Quantum Electron. QE-18, 1185 (1982).

† S. Lovold, P.F. Moulton, D.K. Killinger, and N. Menyuk, "Frequency Tuning Characteristics of a Q-Switched Co:$MgF_2$ Laser," submitted to IEEE J. Quantum Electron.

18. R.J. Nelson, P.D. Wright, P.A. Barnes, R.L. Brown, T. Cella, and R.G. Sobers, Appl. Phys. Lett. **36**, 358 (1980).

19. H. Ishikawa, H. Imai, T. Tanahashi, K. Hori, and K. Takahei, IEEE J. Quantum Electron. **QE-18**, 1704 (1982).

20. I. Mito, M. Kitamura, K. Kobayashi, S. Murata, M. Seki, Y. Odagiri, H. Nishimoto, M. Yamaguchi, and K. Kobayashi, IEEE J. Lightwave Technol. **LT-1**, 195 (1983).

21. J. Chevirer, M. Armand, A.M. Huber, and N.T. Linh, J. Electron. Mater. **9**, 745 (1980).

22. D.E. Holmes, R.G. Wilson, and P.W. Yu, J. Appl. Phys. **52**, 396 (1981).

23. J.D. Oberstar, B.G. Streetman, J.E. Baker, and P. Williams, J. Electrochem. Soc. **128**, 1814 (1981).

24. B. Cockayne, G.T. Brown, W.R. MacEwen, and G.W. Blackmore, J. Mater. Sci. Lett. **2**, 309 (1983).

25. A.K. Chin, I. Camlibel, B.V. Du't, V. Swaminathan, and W.A. Bonner, Appl. Phys. Lett. **42**, 901 (1983).

26. A.K. Chin, I. Camlibel, T.I. Sheng, and W.A. Bonner, Appl. Phys. Lett. **43**, 495 (1983).

27. G.A. Antypas, Appl. Phys. Lett. **37**, 64 (1980).

28. A.R. Clawson, D.P. Mullin, D.I. Elder, and H.H. Wieder, J. Cryst. Growth **64**, 90 (1983).

29. Solid State Research Report, Lincoln Laboratory, M.I.T. (1981:1) p. 10, DTIC AD-A103887/6.

30. S.H. Groves, M.C. Plonko, C.A. Armiento, and V. Diadiuk, J. Cryst. Growth **64**, 83 (1983).

31. S.H. Groves, V. Diadiuk, M.C. Plonko, and D.L. Hovey (to be published).

32. V. Diadiuk and S.H. Groves (to be published).

## REFERENCES


1. See, for example, R.C. Alferness, IEEE Trans. Microwave Theory Tech. **MTT-30**, 1121 (1982).
2. K.C. Gupta, R. Garg, and I.J. Bahl, *Microstrip Lines and Slotlines* (Artech House, Dedham, MA, 1979), p. 257.
3. K. Kubota, J. Noda, and O. Mikami, IEEE J. Quantum Electron. **QE-16**, 754 (1980).
4. S. Uehara, Appl. Opt. **17**, 68 (1978).
5. Solid State Research Report, Lincoln Laboratory, M.I.T. (1984:2), p. 3; also J.P. Donnelly, N.L. DeMeo, G.A. Ferrante, K.B. Nichols, and F.J. O'Donnell, to be published in Appl. Phys. Lett., August 1984.
6. K. Iwasaki, S. Kurazano, and K. Itakuma, Electron Commun. Jpn. **58-C**, 100 (1975).
7. H.A. Haus and C.G. Fonstad, Jr., IEEE J. Quantum Electron. **QE-17**, 2321 (1981).
8. J.P. Donnelly, N.L. DeMeo, and G.A. Ferrante, J. Lightwave Technol. **LT-1**, 417 (1984).
9. E.A. Marcatili, Bell Syst. Tech. J. **53**, 645 (1974).
10. F.J. Leonberger, J.P. Donnelly, and C.O. Bozler, Appl. Phys. Lett. **28**, 616 (1976) DDC AD-A027103/1.
11. J.P. Donnelly, F.J. Leonberger, and C.O. Bozler, Appl. Phys. Lett. **28**, 706 (1976) DDC AD-A028457/0.
12. K. Iga, H. Soda, T. Terakado, and S. Shimizu, Electron. Lett. **19**, 457 (1983).
13. Y. Itaya, T. Matsuoka, Y. Nakano, Y. Suzuki, K. Kuroiwa, and T. Ikegami, Electron. Lett. **18**, 1006 (1982).
14. Z.L. Liau, J.N. Walpole, and D.Z. Tsang, Appl. Phys. Lett. **44**, 945 (1984).
15. Z.L. Liau and J.N. Walpole, Appl. Phys. Lett. **40**, 568 (1982).
16. Y. Itaya, Y. Suematsu, S. Katayama, K. Kishino and S. Arai, Jpn. J. Appl. Phys. **18**, 1795 (1979).
17. M Hirao, A. Doi, S. Tsuji, M. Nakamura, and K. Aiki, J. Appl. Phys. **51**, 4539 (1980).

Further details of this work and the report of a new type pin photodetector, fabricated entirely by metallization procedures and utilizing this high-resistivity InGaAs(Fe), have been submitted for publication.[31,32]

S.H. Groves
V. Diadiuk
M.C. Plonko
D.L. Hovey

diamond core drill. The plate is attached to the tube with the bottom of the trough aligned to the bottom of the hole in the tube. During the bake, the tube is withdrawn far enough to keep the substrate out of the hot zone of the furnace. Just prior to growth, it is moved next to the boat, and the substrate is transferred to the boat well by pushing it off the platform with the rod, the trough serving to guide the motion. The tube is then rotated 180° and used to push the slider until the substrate is protected within the graphite boat. After 5 to 10 min. for reestablishment of thermal equilibrium, the substrate is pushed through an In etch solution, removing 5 to 10 $\mu$m of material, under the growth solution.

A substrate-transfer apparatus utilizing graphite blocks was described earlier.[29,30] In comparison, this fused silica apparatus is much simpler to use, and gave essentially 100 percent successful transfer results over many growths. Also, there is no noticeable effect of outgassing due to introduction of the transfer apparatus into the hot zone. As reported in Reference 30, sulfur contamination can occur with the graphite.

As result of this new apparatus, considerable progress has been made in our understanding of the InGaAs(Fe) material and in development of devices based on this material. We have shown that the transport properties can be explained by mixed electron and hole conduction. With reasonable choices for electron and hole mobilities, $\mu_n$ and $\mu_p$, and an intrinsic carrier concentration $n_i$, this model predicts a variation between $n_{eff} \equiv -1/Re$ and n shown in Figure 1-14, where R is the Hall coefficient, e is the magnitude of the electronic charge and n is the conduction electron density. Iron acts as a compensating deep acceptor, and, as the Fe concentration increases, n decreases and becomes less than the hole concentration, p. The Hall coefficient is weighted toward the high-mobility electrons and is negative in the region shown even though $p \geqslant n$. The increasing contribution of the hole conduction as n decreases causes the apparent carrier concentration, $n_{eff}$, to reach a minimum and then rise. The resistivity, $\rho$, predicted from this model is also shown in Figure 1-14. The predicted maximum resistivity is more than four times greater than that at $n = n_i$. In Figure 1-14, we have used the measured $n_{eff}$ values to determine the n values and with these made the comparison between the measured and predicted resistivities. As can be seen, the agreement is quite good. Often the objective of the Fe doping is to maximize the resistivity; two of the samples shown here come within 5 percent of the predicted 2500 Ω-cm maximum. This is in contrast to InGaAs(Fe) growths made without the substrate transfer technique, for which only a few out of many trials showed resistivities greater than 1000 Ω-cm. The best previously grown sample is shown in Figure 1-14 (together with three samples grown by the substrate-transfer method); it can be identified as that with the highest n value. It was grown with about the same fraction of Fe added to the growth solution as the sample with the smallest n value shown. We estimate that there is at least a five times difference in Fe incorporation between these two samples, a number which indicates the degree of Fe loss to the Fe-P compound formation.

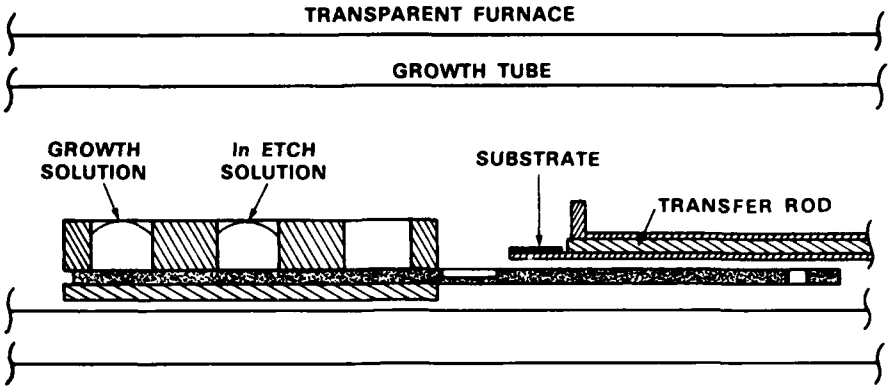


140908-N-01

**Figure 1-13. Schematic drawing of substrate-transfer apparatus cross section showing platform and transfer rod which have been added to the push/pull piece.**

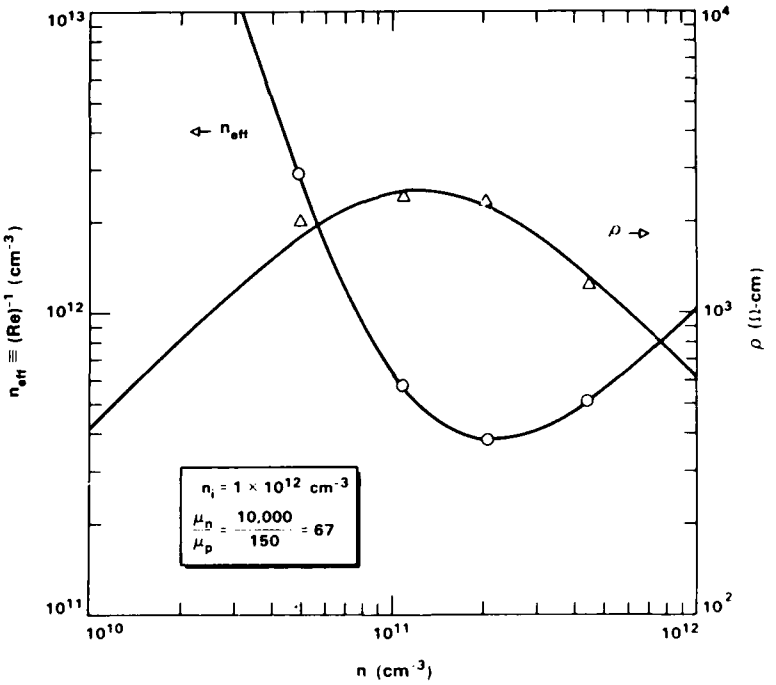


141537-N-01

**Figure 1-14. Curves show $n_{eff}$ and $\rho$ vs n as calculated from the two-band conduction model with $\mu_n = 1 \times 10^4$ cm$^2$/V-s, $\mu_p = 150$ cm$^2$/V-s and $n_i = 1 \times 10^{12}$ cm$^{-3}$. Measured $n_{eff}$ values have been placed on the $n_{eff}$ vs n curve to determine n values. These, in turn, are used to make the comparison between measured and predicted $\rho$ values.**

an In etch just prior to growth.) A key factor in the conversion is the very low Fe doping of the substrate: the atom fraction of Fe in the melt was $1.6 \times 10^{-4}$, which is 5 to 10 times lower than that typically used.

The deep surface conversion was also observed when this material was used as a substrate for MOVPE growth of InP. This involved heating to 650°C in an atmosphere containing $3 \times 10^{-3}$ fraction of $PH_3$. The surface conversion was not seen following LPE growth when the substrate was protected from thermal decomposition either with a localized pocket of phosphorus-rich vapor within the LPE boat or by maintaining a growth-tube atmosphere containing $5 \times 10^{-4}$ fraction of $PH_3$. (The $PH_3$ is more efficiently pyrolyzed in the low flow, isothermal LPE system than the high-flow, locally heated MOVPE system.) Substrates containing the more typical amounts of Fe did not show the surface conversion under any of the above conditions.

It is possible that this deep surface conversion could be caused by accumulation of n-type background impurities in the converted region. This seems unlikely considering the usual profile of n-type material following the rapid outdiffusion.[26] However, further work is needed to conclusively establish that it is indeed Fe that is outdiffusing, and now, considering the large depths involved, whether the depleted Fe can account for the surface accumulation.

S.H. Groves
M.C. Plonko

## 1.5 SUBSTRATE TRANSFER TECHNIQUE FOR THE LPE GROWTH OF InGaAs(Fe)

Growth of high-purity $In_{0.53}Ga_{0.47}As$ lattice matched to InP by liquid-phase epitaxy (LPE) forces consideration of some conflicting objectives. Long-term bakes of the growth solutions are required to reduce the concentrations of the primary impurities, Si and S, but opening the growth apparatus to load the substrate between the bake and growth steps usually recontaminates the system. An approach which has met with some success is to provide a localized phosphorus-rich atmosphere within the LPE boat to protect the substrate from thermal decomposition during the bake.[27] Inevitably, some phosphorus leaks, but this is not enough to noticeably alter the composition of the grown InGaAs. However, for the growth of InGaAs(Fe) by the method of adding Fe to the LPE growth solution,[28] the leaking phosphorus causes the formation of an Fe-P compound that is not soluble in the growth solution. As a consequence, the Fe doping efficiency has been low and highly variable.

This problem has been overcome by the addition of a simple substrate-transfer device shown in Figure 1-13. The fused silica tube used to push/pull the sliding member of the LPE boat has been modified to include a platform for storing the substrate and a concentric fused silica rod. The platform has been constructed from 1/16-in.-thick fused silica plate in which a trough, slightly wider than the substrate, has been milled with a

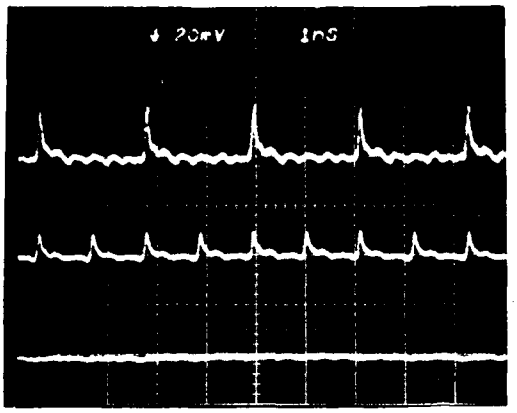


**Figure 2-8. Demonstration of gated diode laser amplifier. See text for explanation.**

train multiplied up to a 2-GHz repetition rate has been used to generate microwave radiation by means of a GaAs avalanche photodiode as well as an Fe:InP optoelectronic switch.

Figure 2-9 shows the schematic arrangement of the optical system which consists of a series of beam splitters and retroprisms. An entering pulse is split into two equal pulses, each of half the original intensity, and one of the pulses is delayed in time by one-half the initial period, $1/f_o$, by the first retroprism labeled one. The two pulses are combined and split at the second beam splitter to produce two beams, each having a repetition rate $2f_o$, with each pulse having one-quarter the intensity of the input. The second retroprism delays the pulses by an amount which is one-half that produced by the first retroprism. The two beams are then combined and split at the third beam splitter to produce two new beams that each have a repetition rate of $4f_o$ with each pulse having one-eighth the intensity of the input. It can be shown from Figure 2-9 that the pulse repetition rate of the final train is given by

$$f = 2^N f_o \quad , \tag{2-1}$$

where N is the number of retroprisms and $f_o$ is the initial mode-locked repetition rate. Except for small optical losses, the output is split into two beams at the exit, each having one-half the average power of the original beam with pulses of equal amplitude. If the initial laser is polarized, the two outputs can be made collinear with a polarization selective reflector.

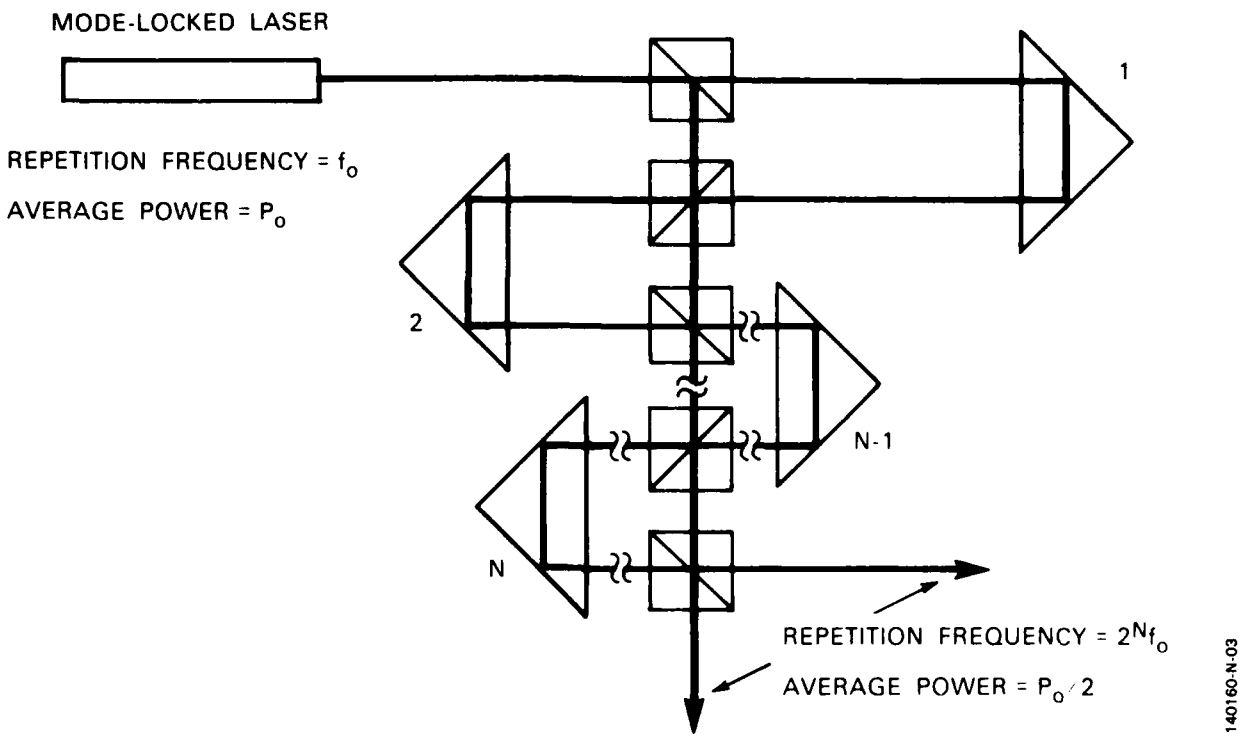


**Figure 2-9. Schematic arrangement of optical components used for spatial time-division repetition rate multiplication of mode-locked laser pulses.**

Figure 2-10 shows optical pulse trains obtained with three retroprisms and four beam splitters. A krypton ion mode-locked laser operating at 6471 Å producing 100-ps pulses at a 250-MHz repetition rate was used as the initial source. The top trace in Figure 2-10(a) is the mode-locked output of the krypton laser with a pulse separation of 4 ns. The second, third, and fourth traces show the form of the optical pulse train after the beam splitter which follows the retroprism labeled 1, 2 and 3, respectively. These traces show the initial repetition rate multiplied by 2, 4 and 8, respectively. In general, it is only necessary at each rate-doubling stage that the difference in path length between two beam splitters through a retroprism and the path length directly between the same two beam splitters be an odd integer multiple of c/2f, where f is the repetition rate that is being doubled. With ten retroprisms, multiplication of 1024 can in principle be achieved. The use of a semiconductor diode laser which can be either mode-locked or driven by a comb generator at multigigahertz rates would provide a more practical system. Such a source would reduce the number of optical elements to achieve a fixed repetition rate as well as reduce the physical dimensions to a size compatible with an all integrated optical system.

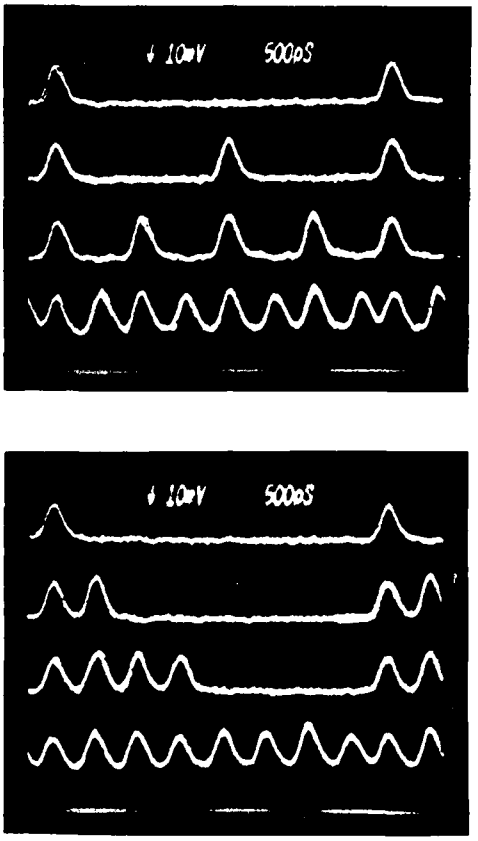


140161-R-01

**Figure 2-10. Oscilloscope traces showing spatial time-division repetition rate multiplication of mode-locked laser pulses using system with three retroprisms and four beam splitters. Time scale is 500 ps/div. (a) Top trace is input signal while lower three traces show the generation of repetition rates $2f_o$, $4f_o$, and $8f_o$. (b) Top trace is the input signal while lower traces are the outputs with retroprism 3, retroprisms 2 and 3, and retroprisms 1, 2, and 3 in the optical path, respectively.**

In addition to the set of pulses shown in Figure 2-10(a), it is possible to achieve the set of pulse forms shown in Figure 2-10(b) simply by either reversing the optical path in Figure 2-9, or by blocking one or more of the optical paths to the retroprisms. For example, the second trace in Figure 2-10(b) has only the optical path to retroprism N = 3 open. An additional feature of this scheme is that each optical path can be independently modulated to select or rapidly switch between any of the possible pulse patterns shown in Figure 2-10(a) and (b).

This technique can have a number of applications in the study of fundamental physical or chemical processes as well as in the area of high-speed optoelectronic devices. One possible device application is the generation of high-frequency microwave radiation by coherent excitation of a large number of high-speed photoconductive switches. For a scheme using two optoelectronic switches driving a load impedance which is equal to the dynamic switch on-state impedance, and using both output beams from Figure 2-9, it can be shown

that the gain, defined as the ratio of microwave output power to laser input power, can be approximately 30 at 10 GHz for InP.

Figure 2-11 shows the output on an RF spectrum analyzer from a high-speed GaAs avalanche photodiode driven by a 250-MHz mode-locked laser beam multiplied by a factor of 8, as shown in Figure 2-10. The display shows the dominant 2-GHz signal and lesser

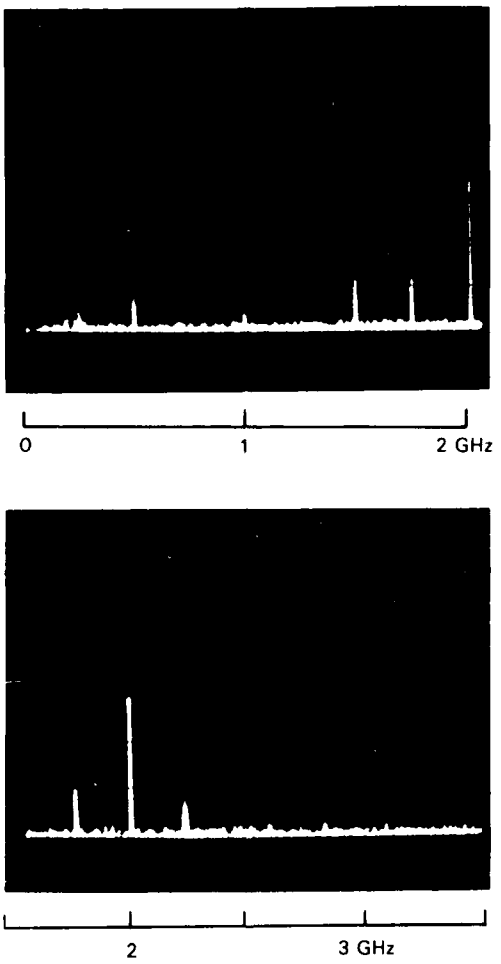


**Figure 2-11. Output on an RF spectrum analyzer from a GaAs avalanche photodiode driven by the 2-GHz signal in Figure 2-10. Amplitude scale is linear. The two traces represent two frequency ranges for the same signal.**

components separated by multiples of 250 MHz which are due to both AM and FM distortion in the signal. Output from an Fe:InP optoelectronic switch produced similar results. By optically driving a large phased-array of such devices, a considerable enhancement in coherent output power may be obtained. In addition, the generation of multihundred gigahertz optical pulses may be useful in optical computing or signal processing.

A. Mooradian

# 3. MATERIALS RESEARCH

## 3.1 MERGED CMOS/BIPOLAR TECHNOLOGIES UTILIZING ZONE-MELTING-RECRYSTALLIZED Si-ON-INSULATOR FILMS

There has been growing interest in the development of merged CMOS/bipolar integrated circuits because they combine high-speed, low-power MOS digital capability with high-performance bipolar analog capability on the same chip. Merged CMOS/bipolar technologies suitable for VLSI circuits have recently been demonstrated[1,2] in bulk Si. The SOI structure should be particularly attractive for this application because it allows more convenient integration of MOS and bipolar devices, permits higher packing density without latch-up, and has the potential to achieve higher speed performance. In this report, we describe two merged CMOS/bipolar technologies that utilize SOI films prepared by zone-melting recrystallization. We have previously reported the fabrication of high-performance CMOS devices,[3] lateral bipolar transistors,[4] and vertical bipolar transistors[5] in films of this type.

The SOI structures used for device fabrication consist of a recrystallized Si film on a $SiO_2$ layer 1 $\mu$m thick on a Si substrate. The films were prepared by the graphite-strip-heater technique for zone-melting recrystallization,[6] which employs an $SiO_2/Si_3N_4$ layer for capping the Si film in order to prevent agglomeration of the molten Si zone.[7] Two different device configurations were used, as shown schematically in Figure 3-1. In the first configuration [Figure 3-1(a)], both CMOS and bipolar devices were fabricated in an SOI film initially ~1 $\mu$m thick. The regions of the film to be used for CMOS devices were etched to a thickness of ~0.3 $\mu$m. For the second configuration [Figure 3-1(b)], the SOI film was ~0.3 $\mu$m thick. The CMOS devices were again fabricated in the film, while the bipolar devices were fabricated in Si epitaxial layers grown selectively on regions of the Si substrate that had been exposed by chemical etching. During epitaxial growth, which was accomplished by decomposition of silane, the recrystallized Si film was masked by the $SiO_2$ capping layer. Nucleation of poly-Si on this layer was prevented by adding a small percentage of HCl to the gas stream. In the second configuration, the bipolar transistors incorporate a buried collector layer, and the merged devices have a more nearly planar structure. Both the SOI and epitaxial bipolar transistors are vertical devices.

For both device configurations, the CMOS and bipolar devices, as well as 39-stage CMOS ring oscillators, were fabricated in a single processing sequence using a total of nine photomask steps. This sequence was based on the processing procedure previously reported[3] for SOI/CMOS devices, which was supplemented by a number of additional steps required in order to make the bipolar devices. The intrinsic base (p region) of both the SOI and epibipolar devices was formed by B ion implantation. The emitter was formed by diffusion from a heavily As-doped poly-Si layer, which was also the gate material for the CMOS devices. The extrinsic base ($p^+$ region) was formed by the B ion implantation used to form the source and drain of the p-channel MOSFETs.

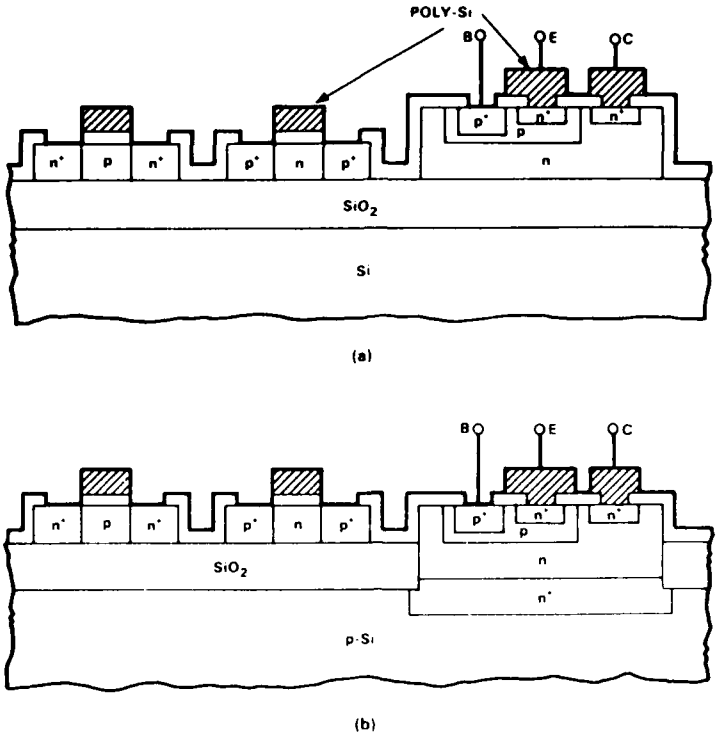


141691 N-01

Figure 3-1. Schematic diagrams of two configurations with SOI/CMOS and bipolar devices fabricated on the same Si wafer. The bipolar device is fabricated in (a) the SOI film or (b) epitaxial layers grown selectively on the Si substrate.

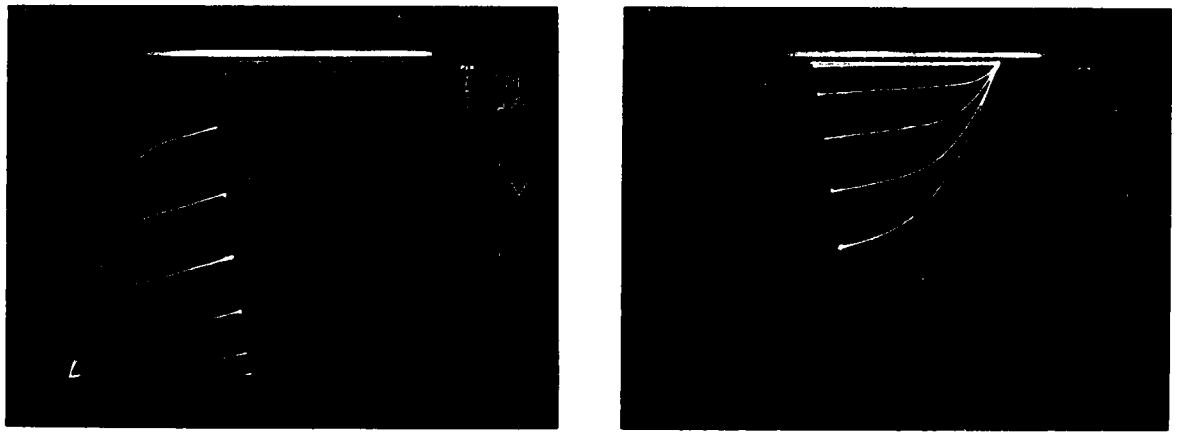

(a) (b)

143651-S

Figure 3-2. Drain I-V characteristics of SOI/MOSFETs: (a) n-channel and (b) p-channel. Gate length is 2 $\mu$m, and gate widths are 30 $\mu$m for n-channel devices and 50 $\mu$m for p-channel devices.

The CMOS devices exhibit well-behaved characteristics. Figure 3-2 shows I-V curves for typical n- and p-channel devices, which have a gate oxide thickness of 40 nm and gate length of 2 $\mu$m. The measured low-field surface mobilities for electrons and holes are ~550 and 200 $cm^2/V\text{-}s$, respectively. Subthreshold leakage currents of <0.1 $pA/\mu m$ (channel width) were measured for both n- and p-channel devices. Figure 3-3 shows the output waveform of a typical 39-stage ring oscillator (fan out = 1) for supply voltage of 5 V. The propagation delay per stage is ~280 ps. The high-speed performance is attributed to the high carrier mobilities and low parasitic capacitances of the SOI structure.

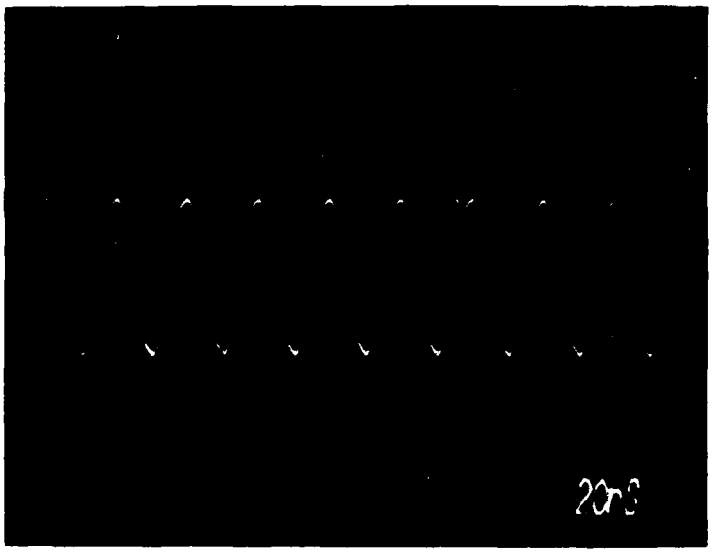

143652 S

**Figure 3-3. Output waveform of 39-stage SOI/CMOS ring oscillator for 5-V supply voltage. The propagation delay per stage is ~280 ps.**

The zone-melting-recrystallized SOI films contain low-angle sub-boundaries.[6] Enhanced dopant diffusion can occur along these sub-boundaries, causing emitter-collector shorting in the SOI bipolar transistors. The use of a poly-Si emitter and careful control of drive-in temperature greatly reduce emitter-collector shorting, even for base widths of only 0.2 to 0.3 $\mu$m. The $V_{EBO}$ of the SOI bipolar devices is ~8 V. This value, which is comparable to the value for the epidevices, indicates good emitter-base junction quality. The $V_{CBO}$ for the SOI devices is >45 V, considerably higher than the value of ~30 V obtained for the epidevices. The increase in collector breakdown voltage for the SOI devices is attributed to the presence of the SiO layer beneath the collector region. For the epidevices, the collector breakdown is governed primarily by the punch-through of the collector space charge region into the heavily doped $n^+$ buried layer. For the SOI devices, however, the entire SOI film beneath the collector-base junction becomes depleted and the field lines are terminated in the $SiO_2$ layer, resulting in a higher breakdown voltage.

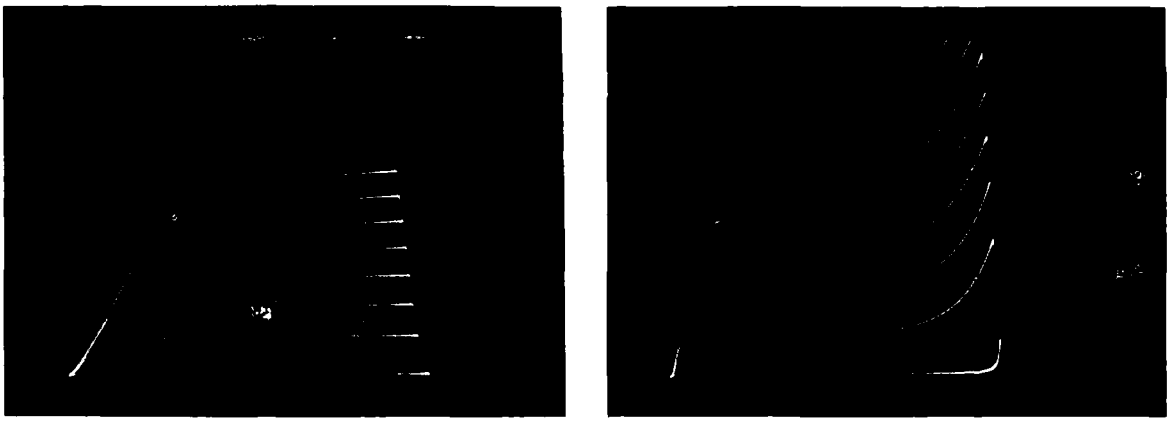

(a) (b)

143653 S

**Figure 3-4. Common-emitter I-V characteristics for bipolar transistors: (a) SOI and (b) epitaxial.**

Figure 3-4 shows typical transistor I-V characteristics for the SOI and epibipolar devices. Common-emitter current gains of more than 100 have been observed for the SOI devices, comparable to those for the epidevices. The $V_{CEO}$ for the SOI devices is ~20 V, compared with ~10 V for the epidevices. Because of the higher collector resistance of the SOI devices, the increase in collector saturation current with base current is not as rapid for these devices as for the epidevices. Thus, the collector currents for $V_{CE}$ = 5 V and $I_B$ = 30 μA are ~20 percent smaller for the SOI devices than for the epidevices. Because of their higher current driving capability, the epidevices should be more suitable for output buffer applications.[8] On the other hand, the SOI devices should also be useful for applications where high current capability is not crucial, such as bipolar sense amplifiers in memory circuits.[9]

B-Y. Tsaur
R. W. Mountain
C. K. Chen
J. C. C. Fan

## 3.2 SELECTIVE TUNGSTEN SILICIDE FORMATION BY ION-BEAM MIXING AND RAPID THERMAL ANNEALING

In the scaling down of MOS devices, silicides are being increasingly used as gate electrodes to reduce interconnect resistance and also as contact material for the source and drain to lower the contact and sheet resistance, as shown in Figure 3-5. A self-aligned silicide technology for MOSFET fabrication[10] would involve the following basic steps: formation of an $SiO_2$ layer on the poly-Si gate and Si source and drain, anisotropic etching to remove $SiO_2$ from the regions where silicide is desired, deposition of a metal film, heating to form the silicide by reaction between the metal and exposed Si, and selective etching to remove the unreacted metal from the $SiO_2$. Refractory metals such as

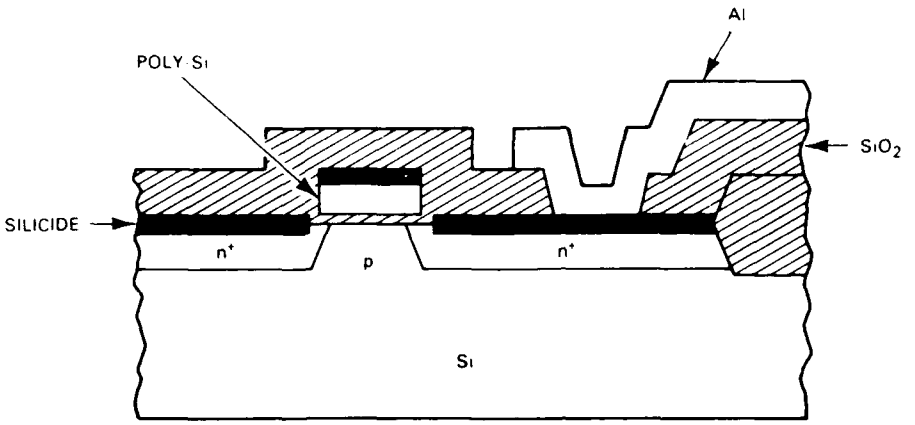


140951-N-01

**Figure 3-5. Schematic structure of a MOSFET with self-aligned silicided gate, source, and drain.**

Mo, W, and Ta are particularly favorable for this application because their silicides are relatively stable in contact with Si at high temperature and the reaction between these silicides and Al is limited. Unfortunately, silicide layers formed by thermal annealing of as-deposited refractory metal films on Si generally exhibit poor surface morphology and irreproducible electrical characteristics because native oxides at the metal-silicon interface interfere with silicide formation. However, the effect of interface contamination can be largely suppressed by ion implantation through the metal-silicon interface,[11-15] which leads to dispersion of impurity atoms at the interface and also to intermixing of the metal and silicon. Uniform silicide layers with smooth surfaces can then be obtained by annealing.

In this report, we describe the formation of tungsten silicide by ion-beam mixing (produced by $As^+$ ion implantation) followed by rapid thermal annealing (RTA). In some experiments, $WSi_2$ was formed selectively in the patterned openings of oxidized Si wafers. In other experiments, it was shown that the implanted $As^+$ ions can dope the Si substrate to form a shallow $n^+$-p junction with good electrical properties. The RTA process, as opposed to conventional furnace annealing, was used in order to (a) minimize unwanted dopant redistribution, which can lead to an increase in junction depth, (b) minimize outdiffusion of dopants from the poly-Si gate and source-drain regions, and (c) prevent bridging of narrow $SiO_2$ regions by lateral silicide formation.

Three types of substrates were used: <100> p-type Si wafers, thermally oxidized Si wafers with patterned openings etched in the $SiO_2$, and oxidized Si wafers coated with a poly-Si film deposited by LPCVD. Tungsten films ~35 nm thick were deposited by e-beam evaporation in an oil-diffusion-pumped vacuum system. Half the samples were implanted with $As^+$ ions having energies of 120 to 180 keV. The samples were subjected to furnace annealing for 20 min. or to RTA using a graphite strip heater[6] for ~10 s.

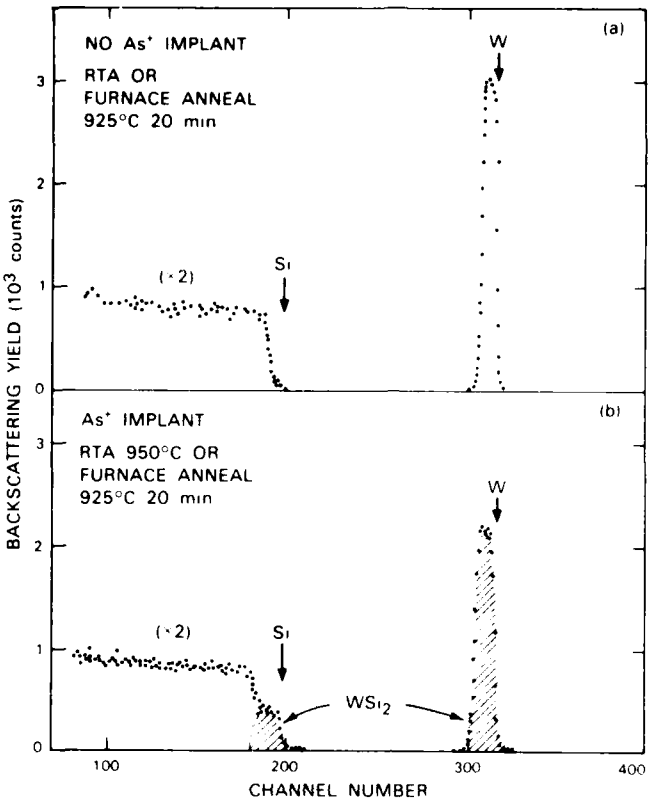


**Figure 3-6. Rutherford backscattering spectra of W-coated Si samples after annealing: (a) without $As^+$ implant, (b) with $As^+$ implant.**

Figure 3-6 shows Rutherford backscattering (RBS) spectra obtained for W-coated Si wafers after annealing. No silicide was detected for the unimplanted samples, but $WSi_2$ was observed for the implanted ones. This indicates that ion-beam mixing is essential for silicide formation. Transmission electron micrographs of $WSi_2$ films formed by RTA at 950°C [Figure 3-7(a)] and at 1000°C [Figure 3-7(b)] show that the films are composed of well-defined grains that increase in size with RTA temperature. The structure of the $WSi_2$ is tetragonal, as shown by the electron diffraction pattern of Figure 3-7(c).

The as-deposited W films have a sheet resistance of ~25 Ω/□. After $As^+$ ion implantation to a dose of $2 \times 10^{15}$ $cm^{-2}$, the sheet resistance increases to ~30 Ω/□. The resistance decreases monotonically with increasing RTA temperature to a value of ~7 Ω/□, compared with ~10 Ω/□ for the furnace-annealed samples.

Prolonged high-temperature annealing for silicide formation can produce unwanted dopant redistribution or outdiffusion, which can have a variety of adverse effects on device characteristics. These effects should be significantly reduced by using the RTA technique. We

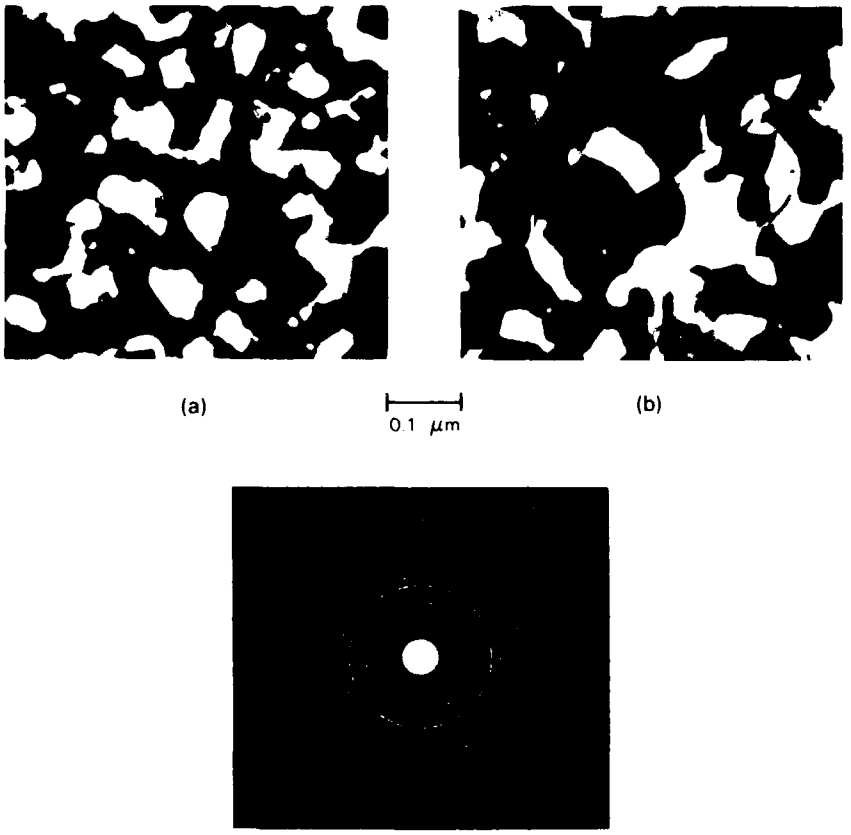


**Figure 3-7. Transmission electron micrographs of $WSi_2$ films formed by RTA at (a) 950°C, (b) 1000°C, and (c) electron diffraction pattern showing tetragonal $WSi_2$ phase.**

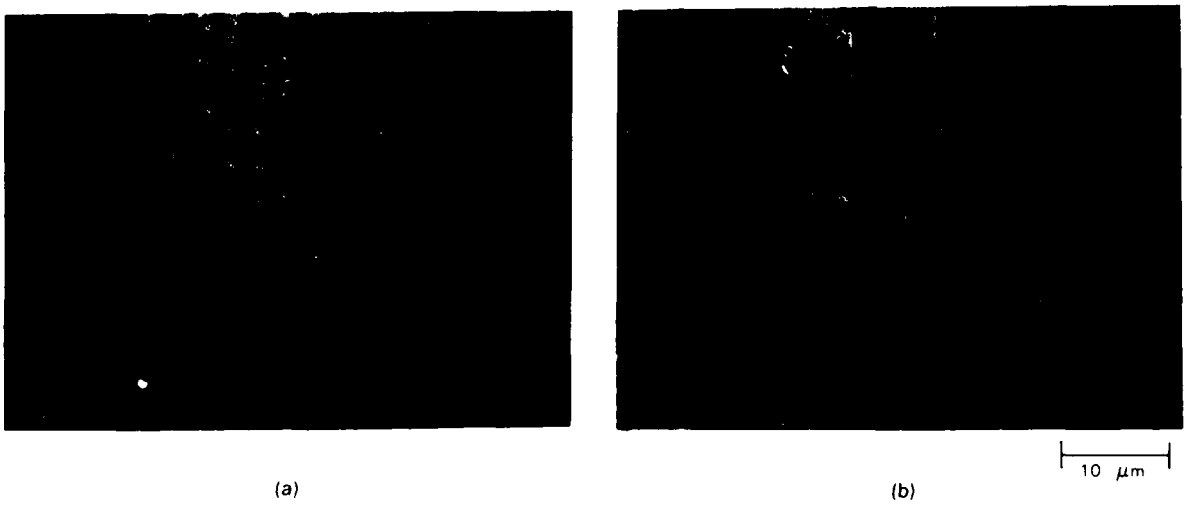


**Figure 3-8. Photomicrographs of $WSi_2$ stripes formed on patterned oxidized Si wafers by RTA at (a) 950°C and (b) 1000°C.**

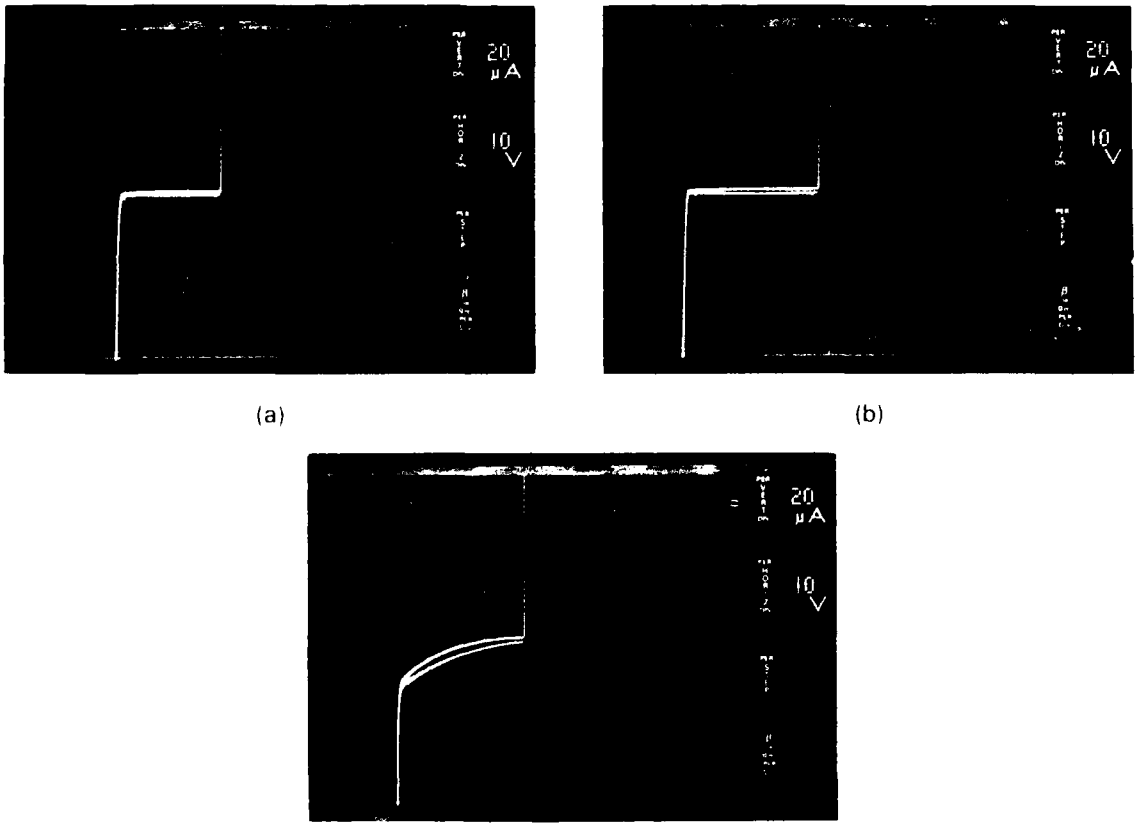


**Figure 3-9. Diode I-V characteristics for shallow $n^+$-p junctions formed by ion-beam mixing and RTA. The $As^+$ ion implantation was performed at energies of (a) 180, (b) 150, and (c) 120 keV.**

have used RBS to measure the As distribution in the as-implanted and annealed samples. During furnace annealing, a significant portion of the implanted As was lost by outdiffusion followed by evaporation from the surface. In contrast, RTA caused much less loss of As. Furthermore, RTA produced negligible diffusion of As into the Si substrate.

In one series of experiments, $WSi_2$ was formed selectively on thermally oxidized Si wafers that had openings 2 $\mu m$ wide etched in the $SiO_2$ film. After the unreacted W was removed by chemical etching, it was found that some lateral silicide formation over the $SiO_2$ had occurred for the furnace annealed samples. Lateral silicide formation was not detected for RTA samples annealed at 950°C [Figure 3-8(a)], but it did occur for such samples annealed at 1000°C [Figure 3-8(b)].

The quality of shallow $n^+$-p junctions formed by ion-beam mixing and RTA has been examined by measuring the diode I-V characteristics. Figure 3-9 shows typical results for devices with $As^+$ ion implantation performed at energies of (a) 180, (b) 150, and (c) 120 keV, respectively. Good characteristics with sharp reverse breakdown are observed for the devices of Figures 3-9(a) and (b), with somewhat higher breakdown voltage for the 150-keV diode. Figure 3-10 shows the distribution of leakage currents for diodes with different As implant

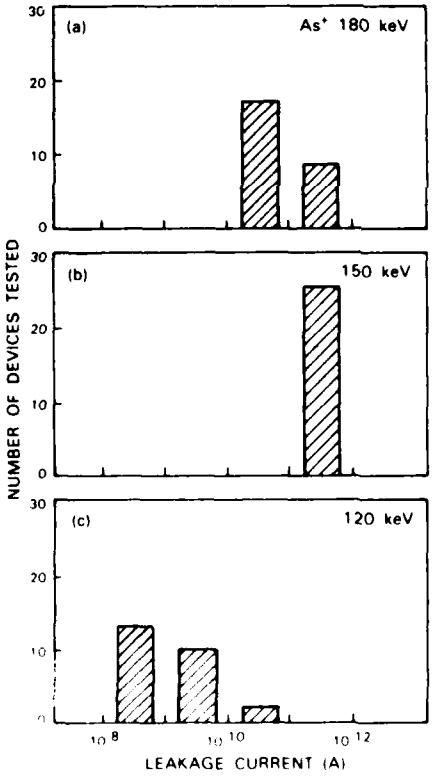


**Figure 3-10. Distribution of leakage currents (measured at a reverse bias of 5 V) for diodes with different As implant energies.**

energies. The best results were again obtained for the 150-keV devices, which have leakage current densities of the order of $10^{-8}$ A/cm$^2$, comparable to those of diodes formed by direct $As^+$ implantation into p-Si substrates.

MOS capacitors with a $WSi_2$-poly-Si gate have been fabricated on oxidized Si wafers by using the ion-beam mixing, RTA technique for $WSi_2$ formation. By means of C-V measurements on these devices, we have determined that the fixed oxide charge and mobile ion densities are each $<2 \times 10^{10}$ cm$^{-2}$ and the interface state density is $<3 \times 10^{10}$ cm$^{-2}$eV$^{-1}$. These results are similar to those obtained on conventional poly-Si gate MOS capacitors, indicating that the new technique is compatible with conventional MOS processing.

Our results show that $WSi_2$ can be formed reproducibly by ion-beam mixing and rapid thermal annealing. The process produces uniform $WSi_2$ layers selectively on patterned oxidized Si wafers with little lateral silicide growth and yields good-quality shallow $n^+$-p junctions with negligible dopant redistribution. This process should be useful for the fabrication of MOSETs with self-aligned silicided gate, source, and drain.

B-Y. Tsaur
C.K. Chen
C.H. Anderson, Jr.

## 3.3 MESFETs FABRICATED IN GaAs LAYERS GROWN DIRECTLY ON Si SUBSTRATES BY MOLECULAR BEAM EPITAXY

Currently, there is increasing interest in achieving the integration of GaAs and Si devices and circuits on the same chip, since such monolithic GaAs Si (MGS) integration could take advantage of the complementary capabilities of the two materials (and also GaAs-based alloys) more fully than the hybrid approach, which combines circuits on separate GaAs and Si chips. Recently, a variety of MGS devices, including light-emitting diodes,[17] double-heterostructure diode lasers,[18] and metal-semiconductor field-effect transistors (MESFETs),[19,20] have been fabricated in GaAs GaAlAs epitaxial layers grown on single-crystal Si wafers to form MGS substrates. In all cases, the GaAs layers were actually grown on a thin intermediate layer of Ge, rather than directly on the Si substrate. Such a Ge layer can facilitate the growth of GaAs, since the nucleation of GaAs on Si is frequently made difficult by the presence of native oxides and other contaminants (particularly carbon) on the Si surface.

We have recently shown[21] that molecular beam epitaxy (MBE) can be used to grow epitaxial GaAs layers directly on Si substrates. The quality of the initial layers did not seem sufficient to justify their use in device fabrication, but we have subsequently obtained layers with significantly improved electrical and photoluminescence (PL) properties. The direct MBE growth on Si of epitaxial GaAs layers with comparable PL properties has also been achieved by Wang.[22] We now report the fabrication of MGS MESFETs with good operating characteristics in GaAs layers grown directly on Si. These are the first devices

**Figure 4-2. Four-phase GaAs overlapping gate CCD.**

A photograph of a completed 16-stage device is shown in Figure 4-2. The CCD is a r-phase structure with the darker first-level metal forming the electrodes for phases 2 4. We have found that the charge transfer efficiencies of these devices are significantly ıter than those of our earlier planar CCDs.[4] This is shown in Figure 4-3, where the ıer trace of each photograph is a group of 32 pulses applied to the CCD input and the er trace is the delayed CCD output. The CCD clock rate was 500 kHz, and the plitude of clock phases 1 through 4 was 5.0 V. In Figure 4-3(a), the spacing between se bursts was 64 $\mu$s, and the charge loss was too small to be measured. The estimated ıer limit on the transfer inefficiency is about $2 \times 10^{-4}$ per transfer for the 64 transfers. s result compares with $7 \times 10^{-2}$ per transfer with 5-V clock swings obtained by Hansell.[3] : device of Figure 4-3(a) also exhibited small charge loss with clock swings as low as V, but at 2 V the loss increased abruptly. This capability for low-voltage operation is ıortant at high clock rates where large amplitude clock swings are difficult to generate.

In Figure 4-3(b), the spacing between bursts was increased to 0.01 s, and a noticeable is evident. This indicates that significant electron trapping is occurring in the CCD nnel. Measurement of this trapping process and identification of the deep levels are now progress and will be reported at a later date.

K.B. Nichols
B.E. Burke
J.T. Kelliher

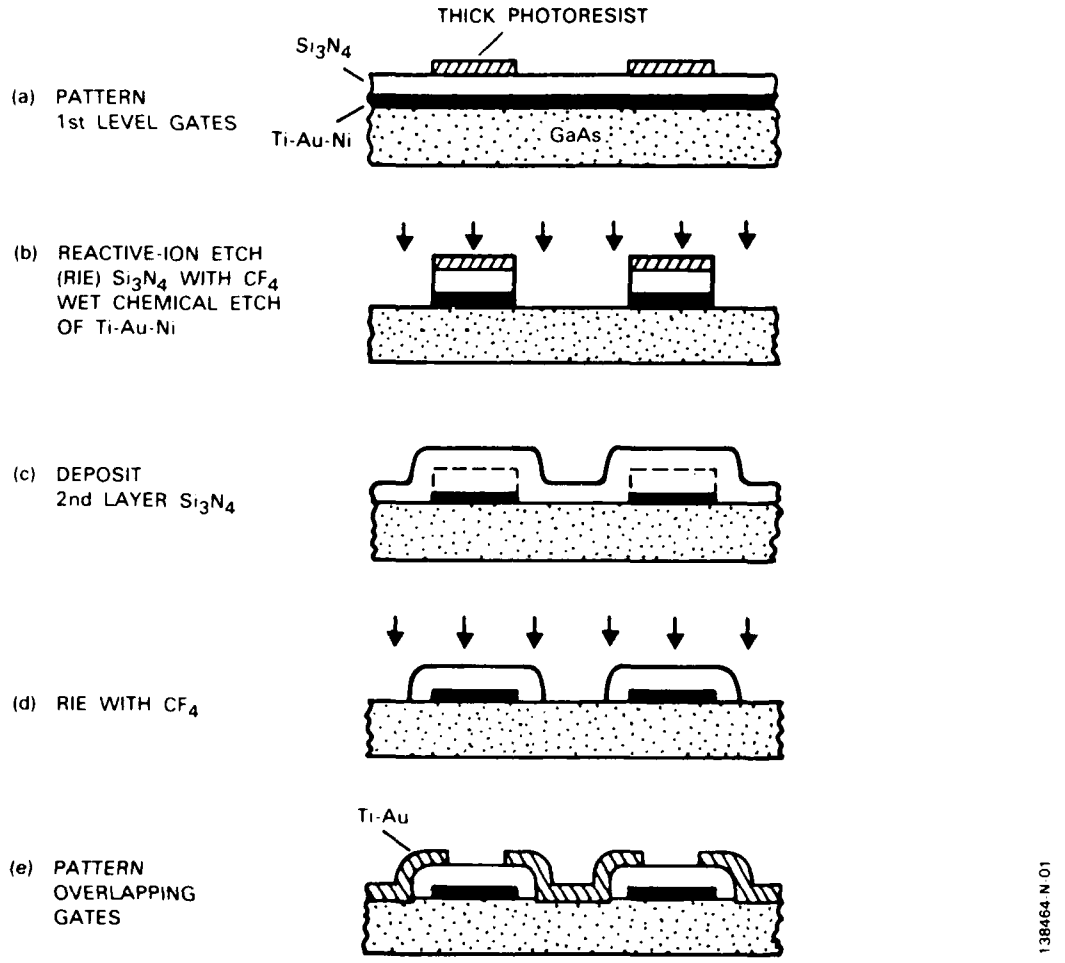


**Figure 4-1. Fabrication sequence of GaAs overlapping gate CCD.**

# 4. MICROELECTRONICS

## 4.1 GALLIUM ARSENIDE OVERLAPPING GATE CHARGE-COUPLED DEVICES

There has been recent interest in GaAs Schottky barrier charge-coupled devices (CCDs) for spatial light modulators[1] and high-speed signal-processing devices.[2] The most common gate structure in these devices consists of a single level of metal with gaps between gates of about 1 to 2 $\mu$m. This gap size is rather critical, since gaps that are too large can cause formation of potential troughs in the channel beneath the gaps[3]. Such troughs trap charge and result in large charge transfer inefficiency (CTI). One of the most difficult device fabrication problems is controlling the gap size to within a fraction of a micrometer. We describe here a new CCD fabrication process for producing an overlapping gate structure in which the gate separation is determined by the thickness of a dielectric film isolating adjacent gates. This readily permits submicrometer control of gap size while using conventional optical lithography of much coarser precision. Initial device results indicate a CTI of less than $2 \times 10^{-4}$ at a 1-MHz clock rate (excluding the effects of bulk trapping). This result is among the best reported for a GaAs CCD and indicates that trapping in troughs has been reduced below our current detection limits, if not eliminated.

The CCDs used in this work were fabricated on n-type epitaxial GaAs grown using $AsCl_3$-Ga-$H_2$ vapor phase epitaxy on a Cr-doped semi-insulating substrate. The epitaxial layer was about 1.3 $\mu$m thick and doped to a net donor concentration of $2.5 \times 10^{15}/cm^3$, resulting in a pinch-off voltage of about 3 V. The sequence of device fabrication steps is outlined in Figure 4-1, and begins with successively evaporated layers of Ti, Au, and Ni of thicknesses 700, 1000, and 800 Å, respectively. This metallization is then coated with 3000 Å of plasma-deposited silicon nitride. The first-level gate pattern is defined in photoresist, leaving the structure shown in Figure 4-1(a). The silicon nitride is then patterned using reactive-ion etching (RIE) with $CF_4$ at a bias of 250 V. This is followed by etching of the Ti-Au-Ni using conventional wet chemistry. The resulting structure is depicted in Figure 4-1(b). Note that the RIE has produced a vertically etched wall in the silicon nitride. It is this anisotropic etching feature which forms the basis of the overlapping gate structure.

In the next step, the RIE photoresist mask is stripped and a second layer of silicon nitride of 5000 Å thickness is deposited [Figure 4-1(c)]. This layer is etched using RIE with $CF_4$ until the GaAs surface is exposed [Figure 4-1(d)]. The anisotropic etching has now left both the top and sides of the first-level gates covered with dielectric. The second-level gates are then produced by a Ti-Au evaporation and lift-off procedure resulting in the structure shown in Figure 4-1(e). The interelectrode gap is determined by the thickness of the second dielectric, and is approximately 5000 Å in this case. It should be mentioned, however, that the wet etching of the first Ti/Au/Ni layer leads to some undercutting which is not depicted in Figure 4-1 and, therefore, the gap size can be somewhat greater. In the device described below, this undercut was measured to be approximately 3000 Å, resulting in a gap size of just under 1 $\mu$m. To obtain better control of gap size, it would be desirable to use a first-level metal such as tungsten which can be etched by the RIE process.

19. H.K. Choi, B-Y. Tsaur, G.M. Metze, G.W. Turner, and J.C.C. Fan, Electron Device Lett. **EDL-5**, 207 (1984).

20. T. Ishida, T. Nonaka, C. Yamagishi, Y. Kawarada, Y. Sana, M. Akiyama, and K. Kaminishi, 42nd Annual Device Research Conference, University of California at Santa Barbara, 18-20 June 1984.

21. B-Y. Tsaur and G.M. Metze, Appl. Phys. Lett. **45**, 535 (1984).

22. W.I. Wang, Appl. Phys. Lett. **44**, 1149 (1984).

23. J.C.C. Fan, B-Y. Tsaur, and B.J. Palm, in *Conference Record, 16th IEEE Photovoltaic Specialists Conference* (IEEE, New York, 1982), p. 692.

24. M.K. Armstrong-Russell, W. Freeman, and E.E. Spitler, Proc. SPIE **407**, 132 (1983).

25. R.D. Dupuis, R.P. Ruth, J.J. Coleman, W.I. Simpson, H-T. Yang, and S.W. Zehr, in *Conference Record, 14th IEEE Photovoltaic Specialists Conference* (IEEE, New York, 1980), p. 1388.

26. C.O. Bozler, J.C.C. Fan, and R.W. McClelland, in *Proceedings 7th International Symposium on GaAs and Related Compounds* (The Institute of Physics, London, 1979), p. 429.

27. G.W. Turner and M.K. Connors, J. Electrochem. Soc. **131**, 1121 (1984).

28. R.P. Gale, G.W. Turner, J.C.C. Fan, R.L. Chapman, and J.V. Pantano, in *Conference Record, 17th IEEE Photovoltaic Specialists Conference* (IEEE, New York, 1984), to be published.

29. R.W. McClelland, C.O. Bozler, and J.C.C. Fan, Appl. Phys. Lett. **37**, 560 (1980).

## REFERENCES


1. J. Miyamoto, S. Saitoh, H. Momose, H. Shibata, K. Kanzaki, and S. Kohyama, 1983 IEEE IEDM, Washington, DC, Technical Digest, p. 63.
2. F. Walczyk and J. Rubinstein, 1983 IEEE IEDM, Washington, DC, Technical Digest, p. 59.
3. B-Y. Tsaur, J.C.C. Fan, R.L. Chapman, M.W. Geis, D.J. Silversmith, and R.W. Mountain, IEEE Electron Device Lett. **EDL-3**. 398 (1982).
4. B-Y Tsaur, D.J. Silversmith, J.C.C. Fan, and R.W. Mountain, IEEE Electron Device Lett. **EDL-4**, 269 (1983).
5. Solid State Research Report, Lincoln Laboratory, M.I.T. (1984:2), p. 31.
6. J.C.C. Fan, B-Y. Tsaur, and M.W. Geis, J. Cryst. Growth **63**, 453 (1983).
7. E.W. Maby, M.W. Geis, Y.L. LeCoz, D.J. Silversmith, R.W. Mountain, and D.A. Antoniadis, IEEE Electron Device Lett. **EDL-2**, 241 (1981).
8. E.L. Hudson and S.L. Smith, 1982 IEEE ISSCC, San Francisco, Technical Digest, p. 248.
9. J. Miyamoto, S. Saitoh, H. Momose, H. Shibata, K. Kanzaki, and T. Lizuka, 1982 IEEE ISSCC, San Francisco, Technical Digest, p. 224.
10. C.M. Osburn, M.Y. Tasi, S. Roberts, C.J. Lucchese, and C.Y. Ting, in *VLSI Science and Technology*, C.J. Dell' Oca and W.M. Bullis, eds. (Electrochemical Society, 1982), p. 213.
11. B-Y. Tsaur and L.S. Hung, Appl. Phys. Lett. **37**, 922 (1980).
12. S.W. Chiang, T.P. Chow, R.F. Reihe, and K.L. Wang, J. Appl. Phys. **52**, 4027 (1981).
13. L.S. Wielunski, C-D. Lien, B-X Liu, and M-A. Nicolet, in *Proceedings Symposium on Metastable Materials Formation by Ion Implantation*, S.T. Picraux and W.J. Choyke, eds. (Materials Research Society, 1981), p. 139.
14. H. Okabayaski, E. Nagasawa, and M. Morimoto, 1982 IEEE IEDM, San Francisco, Technical Digest, p. 556.
15. B-Y. Tsaur and C.H. Anderson, Jr., Appl. Phys. Lett. **41**, 877 (1982).
16. B-Y. Tsaur, J.P. Donnelly, J.C.C. Fan, and M.W. Geis, Appl. Phys. Lett. **39**, 93 (1981).
17. Y. Shinoda, T. Nishioka, and Y. Ohmachi, Jpn. J. Appl. Phys. **22**, L450 (1983).
18. T.H. Windhorn, G.M. Metze, B-Y. Tsaur, and J.C.C. Fan, Appl. Phys. Lett. **45**, 309 (1984).

The heterostructure BSF is well suited to high-efficiency tandem structures with an AlGaAs upper junction. The higher bandgap AlGaAs layer providing the BSF will also act as a rear window to maximize the transmission of light to the lower cell. We have used this structure to fabricate 1.8 eV bandgap AlGaAs shallow-homojunction solar cells with conversion efficiencies over 16 percent AM1 (Reference 28).

Use of the heterostructure BSF in conjunction with CLEFT peeled-film technology[29] will make it possible to fabricate single-junction two-pass cells with a back-surface reflector (BSR). The cell structure allows light that is not initially absorbed in the GaAs to be transmitted through the AlGaAs layer, reflected by a highly reflecting film deposited on the back surface, and absorbed in the GaAs on the second pass. This structure will permit the use of GaAs layers that are half as thick as those in conventional cells but absorb the same amount of light. The BSR cells should exhibit an increase in $V_{oc}$ because of the heterostructure BSF and also because the dark saturation current will be reduced in the thinner GaAs layers, and higher quantum efficiencies are expected because the carriers are generated closer to the collecting junction.

R.P. Gale G.W. Turner
J.C.C. Fan R.L. Chapman

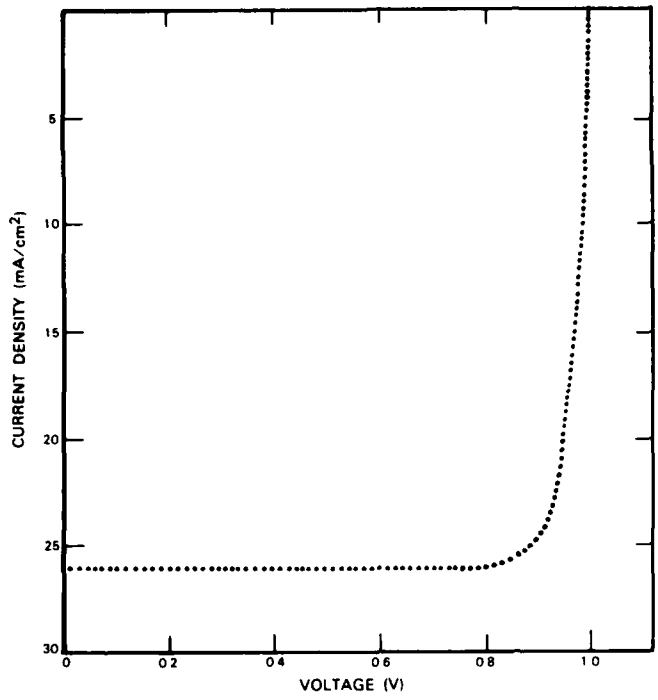


139714-N-02

**Figure 3-19. Photocurrent as a function of voltage for a GaAs cell with heterostructure BSF.**

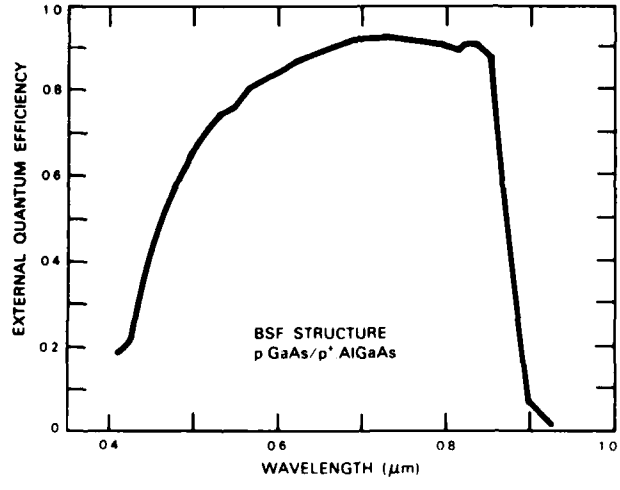


139711-N-01

**Figure 3-20. External quantum efficiency as a function of wavelength for the cell of Figure 3-19.**

to the effective barrier height by the bandgap difference can be several times larger than that due to the difference in doping. Since the BSF is the gradient of the barrier height, the effectiveness of the heterostructure is enhanced because the interface between materials of different bandgaps can be made more abrupt than the doping profile.

The present cells incorporate a $GaAs/Al_{0.2}Ga_{0.8}As$ BSF into the shallow-homojunction structure. A schematic cross section is shown in Figure 3-17. Growth of GaAs and $Al_{0.2}Ga_{0.8}As$ layers was performed by organometallic chemical vapor deposition in a horizontal reactor. The fabrication techniques were similar to those used[27] for shallow-homojunction GaAs cells without a heterostructure BSF, which we shall refer to as conventional cells. The front contact bar and fingers, which were formed by patterning an evaporated Au film deposited on the $n^+$ GaAs layer, were protected during subsequent processing by a mask of plasma-deposited $Si_3N_4$ (Reference 27). The nonmetallized regions of the $n^+$ GaAs layer were then thinned to about 500 Å by alternating anodic oxidation and oxide removal steps. The last of these steps was an anodization that formed an oxide layer that served as a single-layer antireflection (AR) coating. Cells with a total area of 0.54 $cm^2$ were defined by conventional mesa techniques. For the two cells that were found to have the best current-voltage characteristics, the anodic oxide was removed and replaced with an evaporated $MgF_2/ZnS$ double-layer AR coating.

The first effect we observed for the heterostructure BSF was that the open-circuit voltage ($V_{oc}$) under AM1 illumination was 1.00 V even before the anodic thinning process. In Figure 3-18, $V_{oc}$ is plotted as a function of short-circuit current density ($J_{sc}$) before and during the thinning process for a heterostructure BSF cell and a conventional cell. The latter cell, which is typical of our high-efficiency GaAs cells reported previously, shows a steady increase in $V_{oc}$ as $J_{sc}$ is increased with each successive anodization/stripping step. The heterostructure BSF cell, however, exhibits no noticeable change in $V_{oc}$ in spite of a 70 percent increase in $J_{sc}$.

Figure 3-19 shows the current-voltage curve under simulated AM1 conditions, adjusted to a rooftop calibration,[28] for our best heterostructure BSF cell after depositon of the double AR coating. For this curve, $V_{oc}$ is 1.01 V, $J_{sc}$ is 25.6 $mA/cm^2$, and the fill factor (ff) is 0.86, giving an AM1 efficiency of 22.2 percent based on the total cell area. This value cannot be compared directly with the measured efficiency of our best conventional GaAs cell since that cell had an anodic-oxide single AR coating. The efficiency calculated for the conventional cell with a double AR coating is 20.6 percent.

The external quantum efficiency of the cell of Figure 3-19 with a single AR coating is plotted as a function of wavelength in Figure 3-20. The quantum efficiency values are slightly better than those of our best conventional GaAs cell, but the differences are small enough to be due to differences in the anodic AR coating or $n^+$ layer thickness. Because of these variable factors, it is not certain that the heterostructure BSF produces the observed increase in photocurrent over the conventional cell. However, it is clear that the heterostructure BSF causes the observed improvement in $V_{oc}$ and ff.

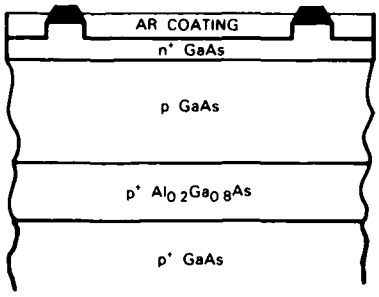


139714-N-01

**Figure 3-17. Schematic cross section of shallow-homojunction GaAs solar cell with GaAs/AlGaAs heterostructure BSF.**

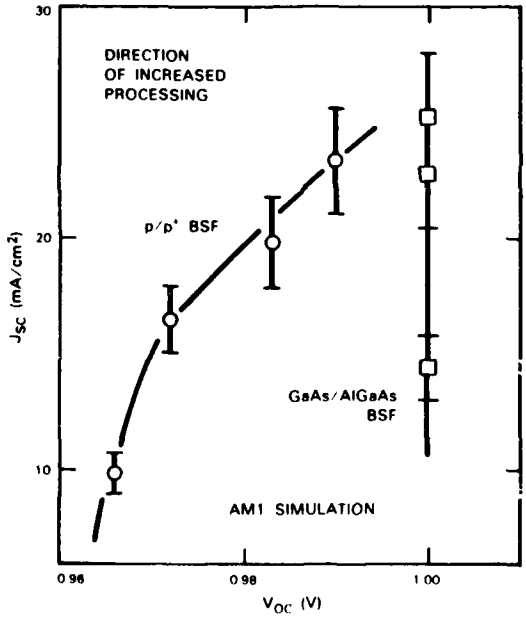


139872-N-01

**Figure 3-18. Open-circuit voltage as a function of short-circuit density for heterostructure BSF and conventional cells under AM1 illumination at various stages of $n^+$ anodic thinning.**

## 3.4 NEW HIGH-EFFICIENCY GaAs SOLAR CELL STRUCTURE USING A HETEROSTRUCTURE BACK-SURFACE FIELD

Recent analyses[23,24] have shown that higher efficiency solar cells have the potential for reducing the overall cost of photovoltaic systems. The maximum practical efficiency achievable by GaAs cells is estimated[23] to be 24 percent. The highest efficiency so far reported[25] for such cells is 22.9 percent, which was obtained for a heteroface cell with an area of only 0.027 $cm^2$. We have previously obtained[26] efficiencies up to 20 percent for shallow-homojunction cells, without an AlGaAs window layer, with an area of 0.5 $cm^2$. In an effort to improve this performance, we have now introduced a heterostructure back-surface field (BSF) into the shallow-homojunction structure. In initial experiments, we have achieved AM1 efficiencies over 22 percent for 0.5-$cm^2$ cells.

A BSF acts as a minority-carrier mirror at the back interface of the absorbing layer of the solar cell, increasing the voltage and collected current. A BSF was incorporated into our previous cells[26] by using a $p/p^+$ doping profile to produce a Fermi level difference of approximately 0.1 eV. The barrier height may be increased by incorporating a heterostructure formed by using a $p^+$ material of larger bandgap. The energy band diagram of an ideal $n^+/p^+/p^+$ heterostructure is shown schematically in Figure 3-16. The contribution

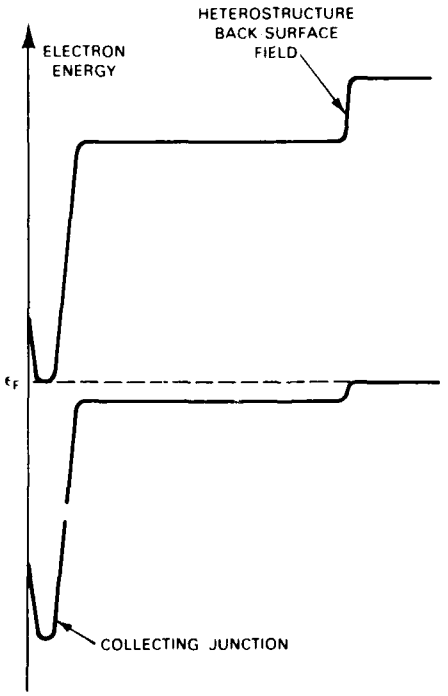


139710-N-01

**Figure 3-16. Schematic energy band diagram of $n^+/p/p^+$ shallow-homojunction solar cell with heterostructure back-surface field.**

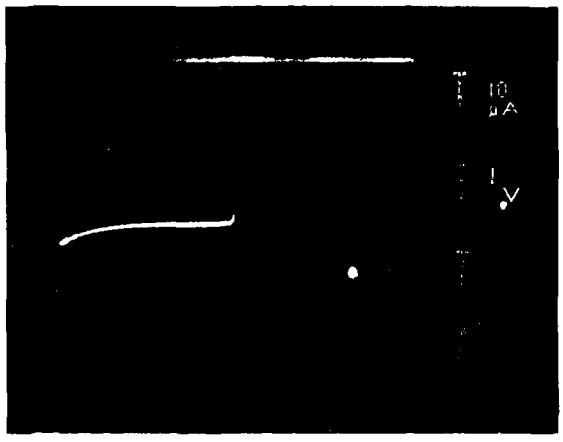


141562 R.01

Figure 3-14. Schottky diode characteristic of MGS MESFET.

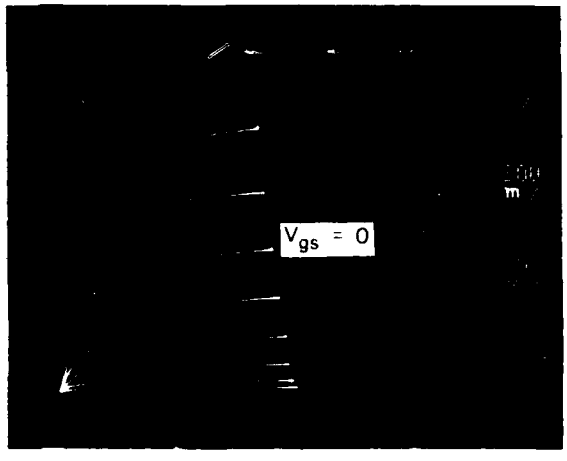


141563-R.01

Figure 3-15. Transistor characteristics of MGS MESFET with substrate biased at +5.0 V.

were made. Test layers were also characterized by measurements of the near-bandgap photoluminescence (PL) excited at 5 K by a Kr ion laser at an incident intensity of about 3 $W/cm^2$. Figure 3-12 shows a representative PL spectrum, which contains peaks at 1.504 and 1.492 eV. The peak at 1.492 eV can be attributed to carbon acceptors. The peak at 1.504 eV may be due to the free exciton, which yields a stronger, narrower peak at 1.515 eV in layers of GaAs grown by MBE on GaAs substrates. A shift of this peak to lower energy in layers grown on Si substrates is expected because of the strain resulting from the difference in lattice properties between GaAs and Si. Alternatively, the peak at 1.504 eV might be a defect-related exciton luminescence. The spectrum in Figure 3-12 also contains an impurity band peaking at about 1.41 eV, which was the only feature observed for our earlier GaAs layers grown directly on Si (Reference 21). The three features shown in Figure 3-12 are also present in PL spectra for our GaAs layers grown by MBE on Ge-coated Si substrates, but the intensity for the GaAs/Ge/Si heterostructure is much lower.

To fabricate the MGS MESFETs, three GaAs layers were grown on a $p^+$ Si substrate: a nominally undoped buffer layer, an n active layer ($n \sim 1 \times 10^{17}$ $cm^{-3}$), and an $n^+$ contacting layer ($n \sim 2 \times 10^{18}$ $cm^{-3}$). The surface of the top layer was mirror-smooth. The devices were then fabricated by essentially the same processing procedure as the one used previously[19] for the MGS MESFETs, with GaAs layers grown by MBE on an intermediate Ge layer. The design of the new devices is shown schematically in Figure 3-13. The only significant differences between this design and the one used earlier[19] are the omission of the Ge layer and an increase in the thickness of the buffer layer from 1 to 2 $\mu$m.

Figure 3-14 shows the Schottky diode characteristic between the source and gate ($2.0 \times 200$ $\mu$m) of an MGS MESFET. The ideality factor and built-in voltage are ~1.13 and ~0.69 V, respectively, compared with the corresponding values of ~1.38 and ~0.67 V for our earlier MESFETs[19] using an intermediate Ge layer. The reverse leakage current for the new device is $<1$ $\mu$A (at $V_{gs} = -3$ V), which is lower by a factor of about 100 than the value obtained for the earlier devices. This dramatic reduction in leakage current is probably a combined effect of the elimination of the Ge layer and the improvement in the quality of the active region resulting from the increase in buffer layer thickness.

Figure 3-15 shows the low-frequency transistor characteristics of the MESFET of Figure 3-14 with the substrate biased at +5.0 V. The transconductance measured at $V_{gs} = 0$ V is ~85 mS/mm, compared with ~105 mS/mm for the MGS MESFETs[19] that had an intermediate Ge layer. If the substrate is not biased, the transconductance is unchanged, but a slight unexplained kink appears in the I-V curves.

G. M. Metze
H-K. Choi
B-Y. Tsaur

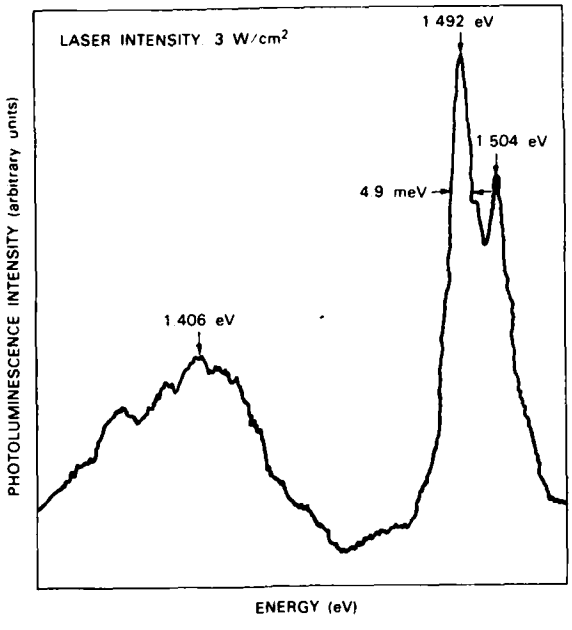


141837-N

**Figure 3-12. Photoluminescence spectrum at 5 K of nominally undoped GaAs layer grown directly on Si.**

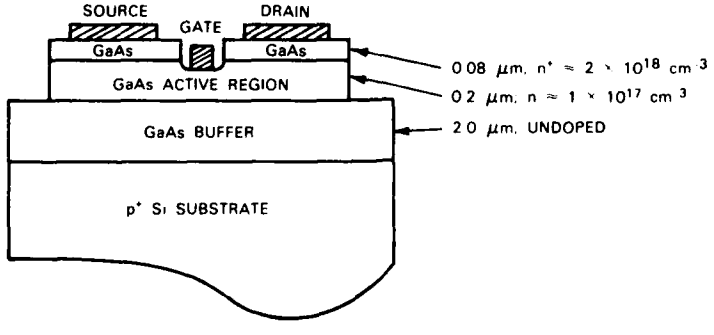


141838-N-01

**Figure 3-13. Schematic diagram of MGS MESFET.**

fabricated in such layers. Omission of the Ge layer is advantageous because it not only simplifies material preparation but also eliminates the possibility of Ge autodoping during GaAs growth.

The procedure followed for direct MBE growth of GaAs on Si was similar to the one used previously.[21] Silicon substrates oriented 2° off (100) were chemically cleaned, immediately loaded into the MBE system, and preheated to an elevated temperature in order to remove native oxides and other surface contaminants. Deposition of GaAs at a rate of ~1 μm/h was then performed at conventional MBE growth temperatures. Reflection electron diffraction was again used for *in situ* monitoring of the surface structure during substrate preheating and GaAs deposition. The diffraction results were essentially the same as those reported earlier.[21] After ~50 Å of growth, the layers exhibited one-half ordered surface reconstruction, indicating good epitaxial growth.

Figure 3-11 is a cross-sectional transmission electron micrograph of a nominally undoped GaAs test layer about 4 μm thick grown directly on Si. The dislocation density in the region more than about 2 μm from the GaAs/Si interface is seen to be several orders of magnitude lower than the density near the interface, but no absolute density measurements

143654 S

**Figure 3-11. Cross-sectional TEM of GaAs/Si heteroepitaxial test structure. Scale: 20 mm = 0.5 μm.**

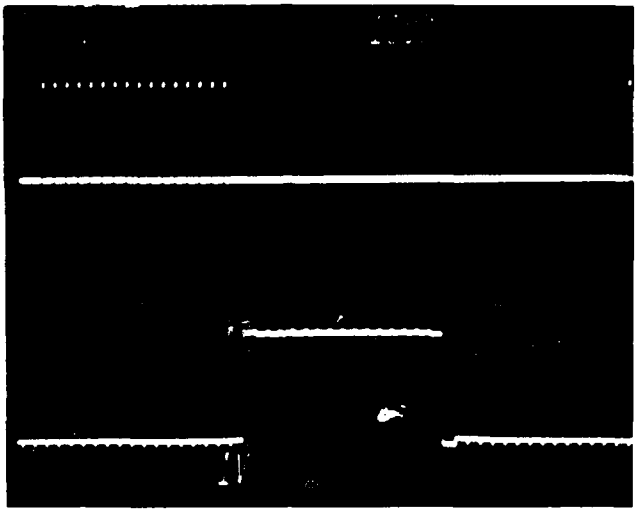

(a)

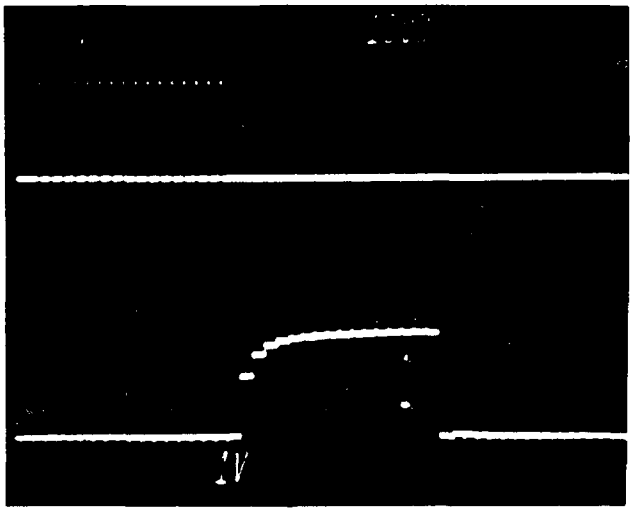

(b)

1436427

Figure 4 3. CCD input (top) and output (bottom) for (a) 64-$\mu$s space between pulse bursts, and (b) 10-ms space between pulse bursts.

## 4.2 MICROWAVE PERFORMANCE OF OMCVD-OVERGROWN PBTs

GaAs permeable-base transistors (PBTs) were first fabricated using chloride transport vapor phase epitaxy (VPE) to overgrow a submicrometer tungsten grating.[5] Although VPE-overgrown PBTs have been fabricated with a maximum frequency of oscillation ($f_{max}$) exceeding 100 GHz (Reference 6) reproducible fabrication of these devices has not been possible. In this report, we describe the first GaAs PBTs fabricated using organometallic chemical vapor deposition (OMCVD) overgrowth. SIMS analysis of these OMCVD-overgrown tungsten gratings indicates that impurities in the tungsten are not incorporated in the overgrown GaAs within the detection limits of the SIMS analysis ($<10^{16}$ atoms/cm$^3$) (Reference 7). Also, chlorine incorporation near the tungsten fingers, which has been a problem in VPE overgrowth, is not observed.

The emitter side of the transistor was grown in a conventional $AsCl_3$ VPE reactor on a Si-doped ($2 \times 10^{18}$cm$^{-3}$) GaAs substrate. The epitaxial film was 0.4 $\mu$m thick with a carrier concentration of $6 \times 10^{16}$ cm$^{-3}$. Fabrication of the tungsten grating followed procedures described previously.[5] At this point, the wafer was divided so that a control VPE overgrowth could be preformed in addition to the OMCVD overgrowth.

The OMCVD system used for GaAs overgrowth in this work was a conventional horizontal quartz reactor with an RF induction heater. Source materials for epitaxial growth were trimethylgallium (TMG) and arsine ($AsH_3$), and the growth temperature was 630°C. The thickness of the GaAs overgrowth was 1 $\mu$m with a selenium doping concentration of $5 \times 10^{16}$ cm$^{-3}$. After OMCVD and VPE overgrowth, ohmic contacts to the GaAs substrate (emitter) and overgrown GaAs (collector) are formed using evaporated Ni-Ge-Au and a 450°C anneal.

Figure 4-4 shows the DC characteristics of a control VPE-overgrown PBT (a) and a typical OMCVD-overgrown PBT (b). The OMCVD-overgrown PBTs have higher

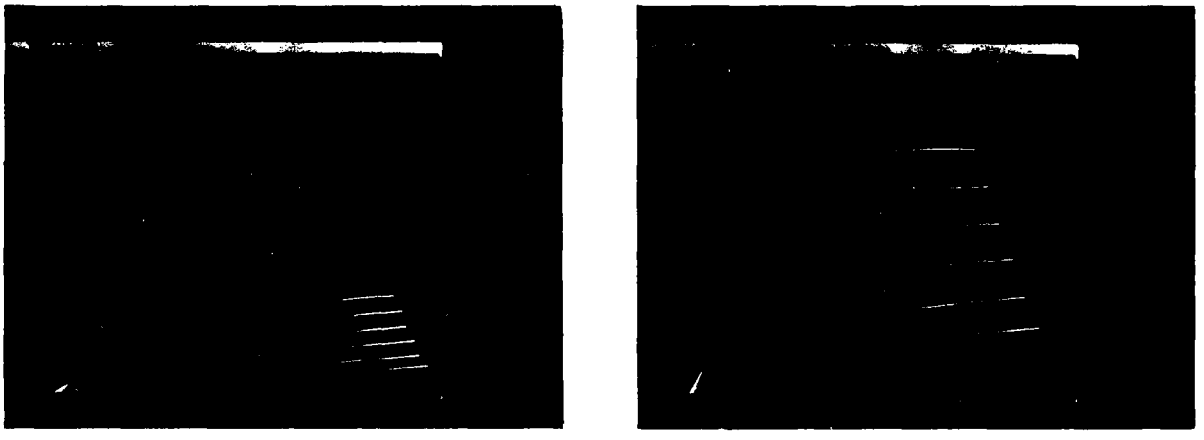

140770 R

(a) (b)

**Figure 4-4. DC characteristics of GaAs PBTs overgrown by (a) VPE, and (b) OMCVD.**

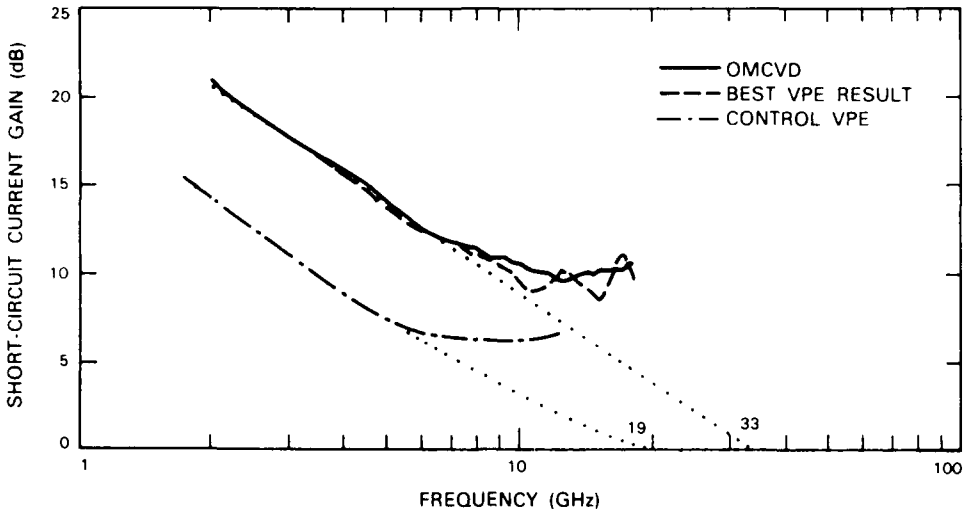


Figure 4-5. Short-circuit current gain vs frequency for various GaAs PBTs.

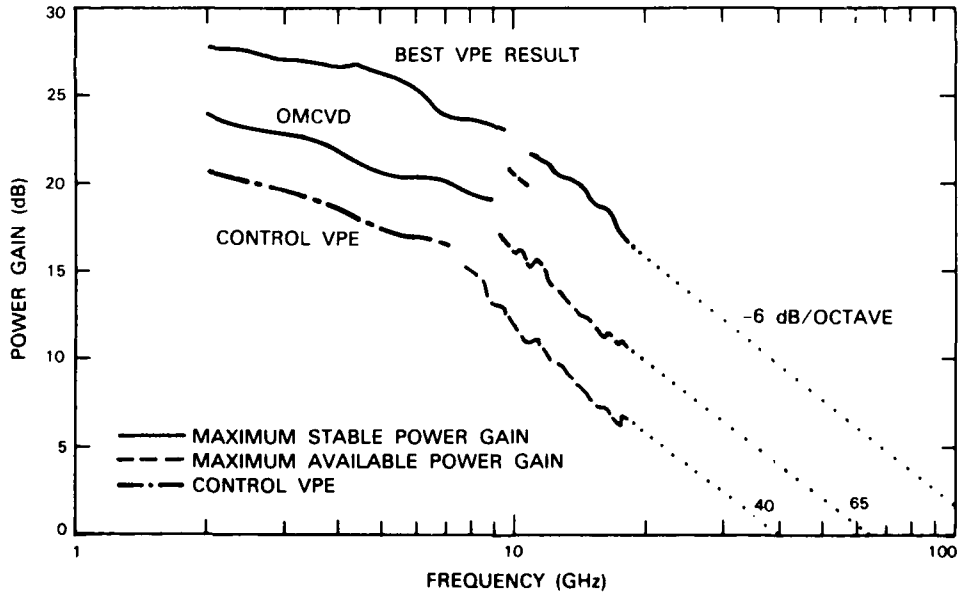


Figure 4-6. Power gain vs frequency for various GaAs PBTs.

transconductance and greater collector current at a given bias than the VPE-overgrown PBTs. The uniformity of device characteristics was also excellent for the OMCVD-overgrown PBTs, while the device in Figure 4-4(a) was one of a few good devices on the VPE-overgrown wafer. Figure 4-5 is a plot of short-circuit current gain vs frequency for a control VPE-overgrown PBT, an OMCVD-overgrown PBT and the best VPE-overgrown PBT to date.[6] The extrapolation of these microwave measurements yields an $f_T$ of only 19 GHz for the control VPE-overgrown PBT. On the other hand, the 33-GHz extrapolated $f_T$ of the OMCVD-overgrown PBT equals the best $f_T$ of any PBT fabricated to date. The OMCVD-overgrown PBTs also exhibit better microwave performance than the control VPE-overgrown PBTs, as illustrated in Figure 4-6. Extrapolation of the power gain at 18 GHz using a 6-dB/octave roll-off yields a maximum frequency of oscillation ($f_{max}$) of 65 GHz for the OMCVD PBT compared with 40 GHz for the control VPE PBT. This improvement in $f_{max}$ for the OMCVD PBT over the control VPE PBT is directly proportional to the ratio of $f_T$ for these PBTs. This extrapolated $f_{max}$ of the OMCVD PBT, however, is significantly lower than the 100-GHz $f_{max}$ of the best VPE PBTs fabricated to date. The equivalent circuit elements calculated from measured S-parameters for the OMCVD PBT and the best VPE PBT are given in Figure 4-7. The most significant difference between these PBTs is the lower output impedance of the OMCVD PBT. This impedance dominates the power gain of the OMCVD PBT, thus significantly reducing the $f_{max}$. We are currently attempting to fabricate OMCVD PBTs with higher output impedance (by reducing the doping of the

| | $R_B$ (ohms) | $R_E$ (ohms) | $R_C$ (ohms) | $R_I$ (ohms) | $C_{BE}$ (pF) | $C_{BC}$ (pF) | $g_m$ (m) | $R_{OUT}$ (ohms) | $f_T$ (GHz) | $f_{max}$ (GHz) |
|---|---|---|---|---|---|---|---|---|---|---|
| OMCVD | 0.9 | 2.2 | 6.4 | 2.3 | 1.05 | 0.05 | 211 | 185 | 33 | 65 |
| BEST VPE RESULT | 1.0 | 4.0 | 8.6 | 3.6 | 1.05 | 0.01 | 162 | 894 | 33 | >100 |

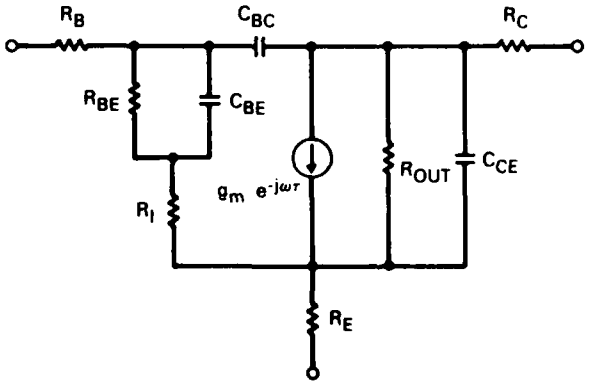


140764-N-01

**Figure 4-7. Comparison of model elements for GaAs PBTs.**

overgrown GaAs layer) without significantly degrading other device parameters. The microwave performance of such devices would equal or exceed the best PBT performance so far achieved. In conclusion, we have fabricated PBTs using OMCVD to overgrow submicrometer tungsten gratings. Extrapolation of microwave measurements on these devices yields an $f_T$ of 33 GHz, which equals the best result to date. While the 65-GHz $f_{max}$ of the OMCVD PBT was lower than the best PBTs, improvements in the output impedance will significantly improve $f_{max}$.

K.B. Nichols C.L. Chen
R.P. Gale G.A. Lincoln
M.A. Hollis C.O. Bozler

## 4.3 A COMPARISON OF E-BEAM EVAPORATED AND ELECTROPLATED AuZn OHMIC CONTACTS TO p-TYPE GaAs

Ohmic contacts with low specific resistance to p-type GaAs are needed for the fabrication of a number of devices, such as JFETs and pn-junction varactor diodes, which are used in microwave and electrooptical applications. The present work is part of a p-i-n diode development effort. The purpose of this study is to evaluate the relative merits of several AuZn metallization techniques for the fabrication of ohmic contacts to p-type GaAs doped to a concentration in the range of $8 \times 10^{18}$ to $2 \times 10^{19}$ $cm^{-3}$.

The deposition techniques investigated were: sequential e-beam evaporation of Zn and Au, electroplating Au containing 0.5 percent Zn, and electroplating pure Au. A summary of metal thickness for each ohmic metallization technique is shown in Table 4-1. After metallization, the samples were encapsulated with 3500 Å of phosphosilicate glass and alloyed at 450°C for 30 s. Specific contact resistivities were determined by the Transmission Line Method (TLM)[8] for each of the three processes. Results are shown in Table 4-1. Specific resistances in the range of $1 \times 10^{-5}$ to $2 \times 10^{-5}$ ohms/$cm^2$ were obtained by all three techniques. Lowest resistivities were obtained by sequential e-beam evaporation of Zn and Au. A comparison of the specific contact resistivities obtained in this study with theory[11] and previously published data[9-11] is shown in Figure 4-8. The theoretical curve is based on a thermionic-field-emission model assuming a barrier height of 0.48 V and an effective hole mass equal to a tenth of the free electron mass.[9]

Upon alloying there is redistribution of the constituents across the original metal semiconductor interface as shown by the Auger sputter profiles. The diffusion of Au, Ga, and As was minimal for the e-beam evaporated contact (Figure 4-9). Slightly more diffusion occurred in the case of the plated AuZn contact (Figure 4-10), and extensive diffusion took place in the last case (Figure 4-11). Approximate thickness of the transition region for each of the metallization techniques is shown in Table 4-1.

**TABLE 4-1**

**Ohmic Deposition Techniques and Results**

| Ohmic Process | Specific Resistance (Ohms-cm$^{-2}$) | Thickness of Transition Region (Å Approx.) |
|---|---|---|
| Evaporate<br>300 Å Zn<br>700 Å Au<br>Alloy | $1.7 \times 10^{-5}$<br>$8.3 \times 10^{-6}$ | 1000 Å |
| Plate<br>600 Å Au 0.5% Zn<br>Alloy<br>3000 Å Au Plate | $1.1 \times 10^{-5}$ | 1600 Å |
| Combination<br>300 Å Au e-Beam<br>800 Å AuZn Plate<br>Alloy | $2.8 \times 10^{-5}$ | 3000 Å |

The flow of current from the metal to the semiconductor is across the transition region of the alloyed ohmic contact. As a result, the thinnest transition interface produces the lowest contact resistance. This is confirmed by a comparison of the TLM data with Auger sputter profiles obtained from the prepared samples of the three metallization techniques. The evaporated AuZn contacts were homogeneous and they exhibited the lowest specific resistivity. However, optimization of this technique requires still further developments in the Zn evaporation procedure.

The electroplated Au with 0.5% Zn contacts were slightly higher in specific resistance and were not as homogeneous as the evaporated samples because of the nonuniform current distribution in the p-layer during plating. However, a relatively low contact resistance combined with simplicity of the process makes electroplating contacts desirable for some applications.

The third metallization technique overcomes plating problems by use of the conducting underlayers. But higher contact resistance due to the thicker transition regions makes this technique the least desirable one.

R.C. Brooks
L.J. Mahoney
R.W. McClelland
A. Chu
M.C. Finn

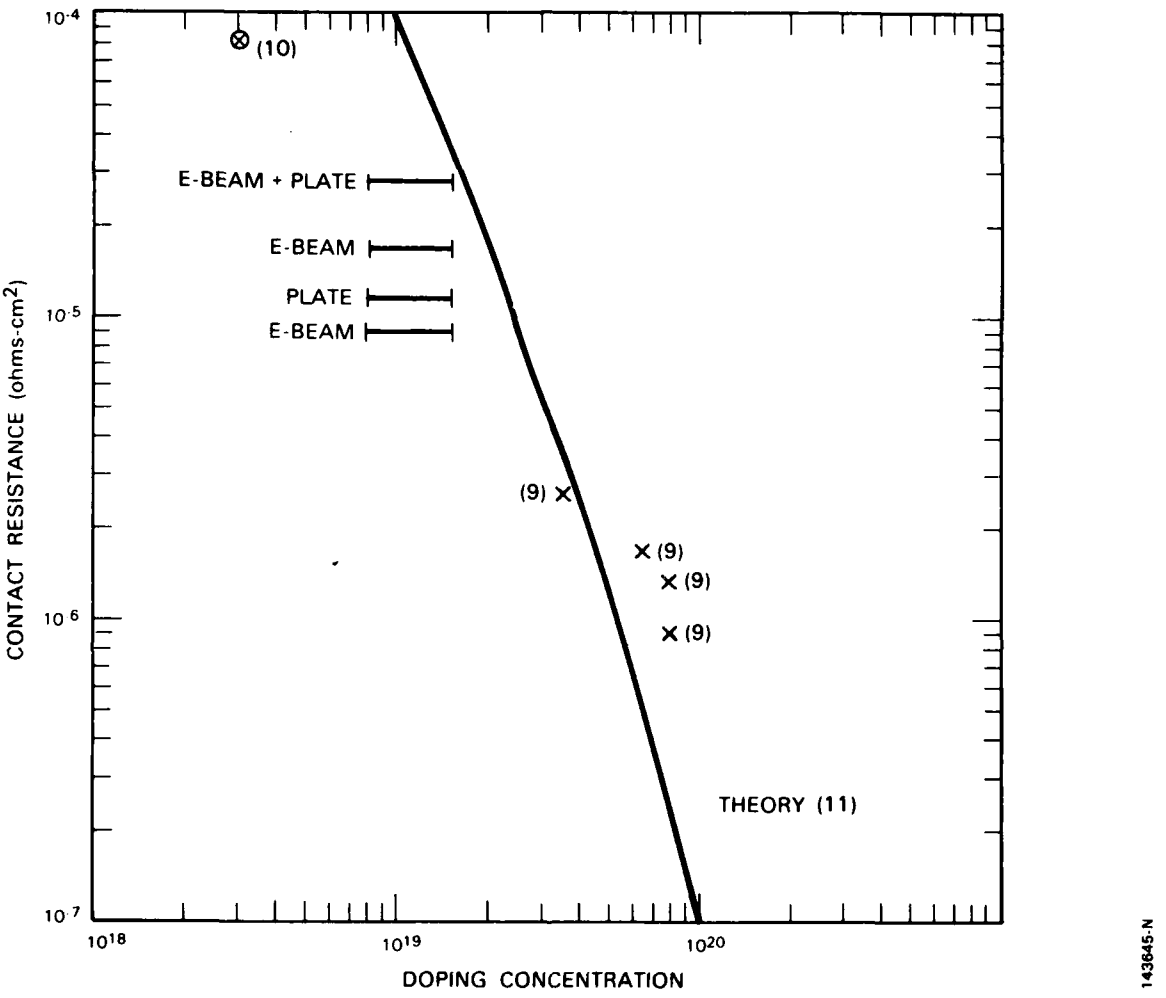


**Figure 4-8. Theoretical ohmic contact resistivities to p-type GaAs as a function of doping concentration.**

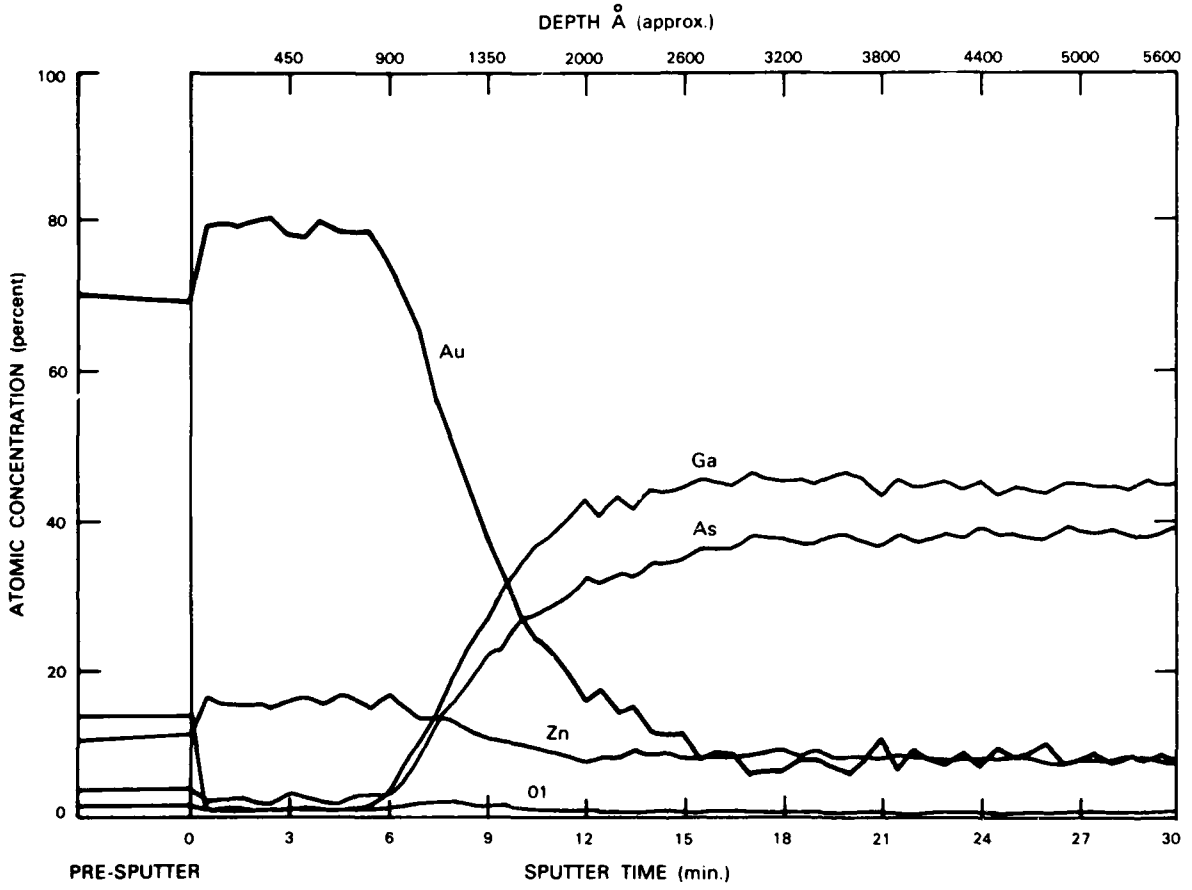


**Figure 4-9. Auger sputter profile of evaporated AuZn contact.**

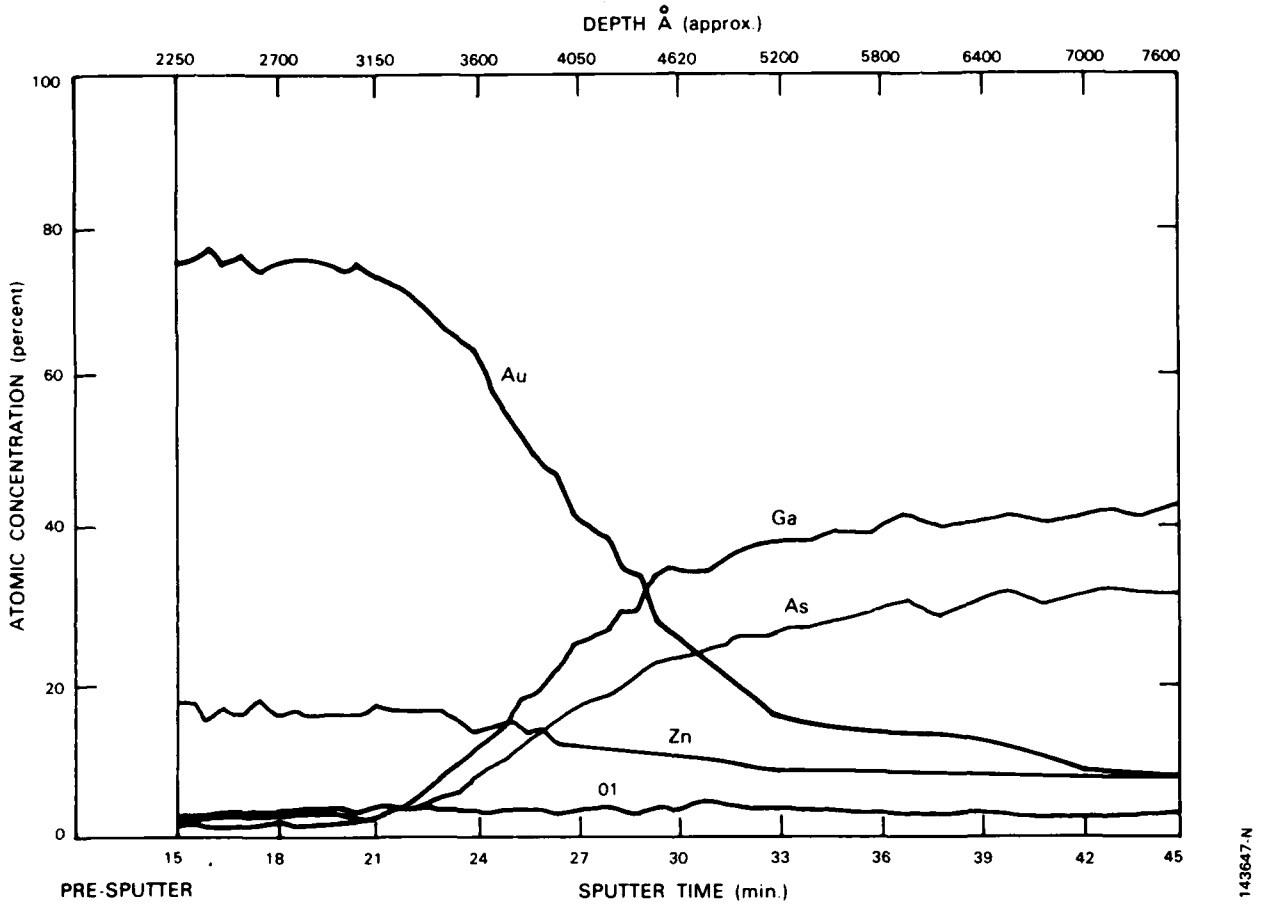


**Figure 4-10. Auger sputter profile of electroplated Au with 0.5 % Zn contact.**

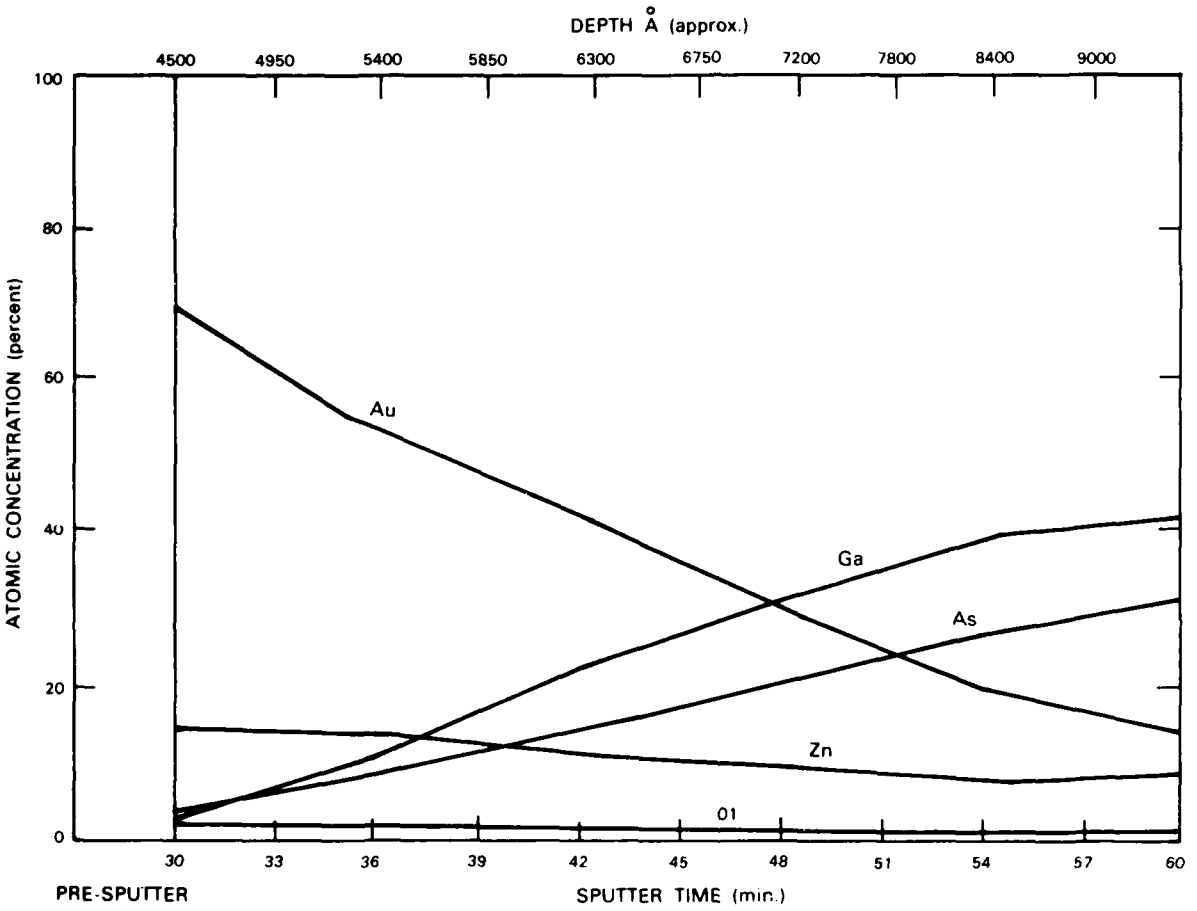


**Figure 4-11. Auger sputter profile of evaporated Au in combination with electroplated Au with 0.5% contact.**

## 4.4 ION-BEAM-ASSISTED ETCHING OF DIAMOND

The high thermal conductivity, low RF loss, and inertness of diamond makes it useful in traveling-wave tubes operating above 500 GHz. Such use requires the controlled etching of diamond to produce grating-like structures tens of micrometers deep. The inertness of diamond makes it difficult to fabricate grating structures. For example, our previous work on reactive-ion etching (RIE) with $O_2$ gave etching rates on the order of 20 nm/min. and poor etch selectivity between the masking material, Ni or Cr, and the diamond. Others have used reactive-ion beam etching with similar results.[12] In this report, an alternative approach is discussed which uses a Xe+ beam and a reactive gas flux of nitrogen dioxide, $NO_2$, in an ion-beam-assisted etching (IBAE) system. The effects of $NO_2$ flux, substrate temperature, and ion beam parameters on the etch rate and resulting etch profile are reported below.

Figure 4-12 is a schematic drawing of the IBAE system. The ion beam is produced by a Kaufman ion source. The beam consists of 2-keV Xe+ ions with a flux density of 1 mA $cm^2$. The reactive gas consists of $NO_2$ which is supplied by two jets (only one is shown in the figure). The use of $NO_2$ as the reactive gas has two important advantages over $O_2$. One is that $NO_2$, unlike $O_2$, is efficiently collected on the $LN_2$ trap. This makes it possible to operate the system at $2 \times 10^{-4}$ Torr while still maintaining a reactive flux on

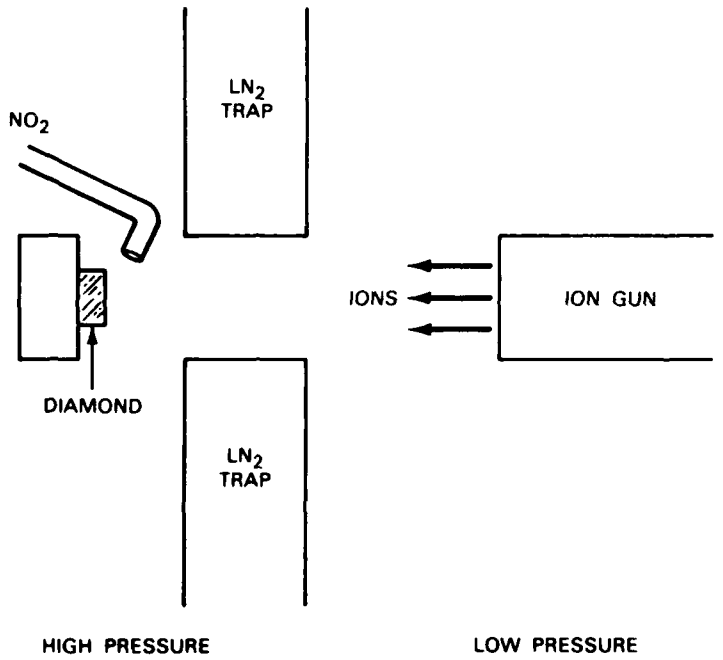


**Figure 4-12. Drawing of a cross section of IBAE system utilizing the $LN_2$ trap to isolate the reactive gas region from the ion gun.**

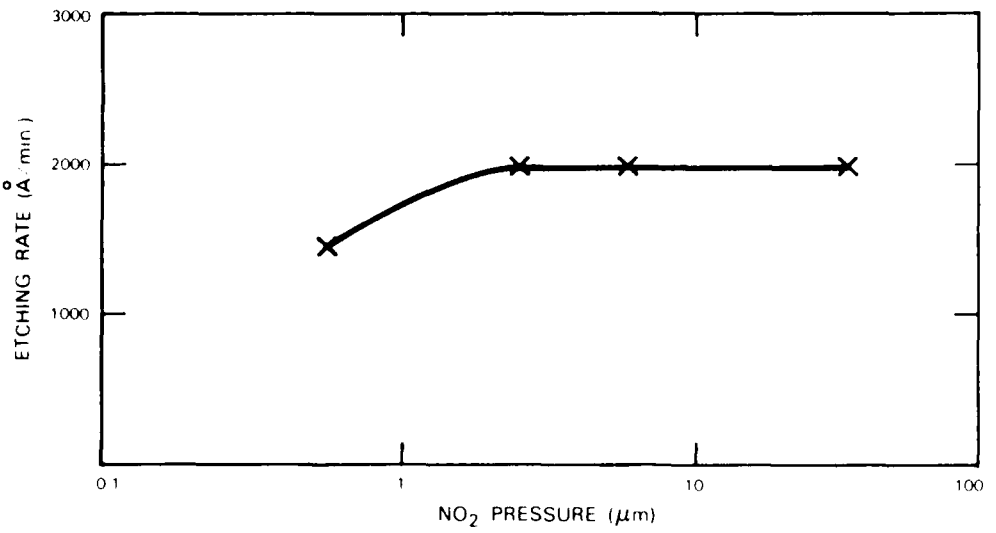


**Figure 4-13. The etching rate of diamond as a function of equivalent reactive gas pressure.**

ıe diamond sample in excess of 10 $\mu$m of equivalent pressure. In addition, when $O_2$ is sed to replace $NO_2$, the etching rate of diamond drops by a factor of 3. Figure 4-13 ıows the etching rate of diamond as a function of equivalent $NO_2$ pressure. Since the etch ıte is constant above 2 $\mu$m, the system was usually run at 5 $\mu$m of equivalent pressure.

The substrate temperature was found to be important in determining the etching rate of iamond, as shown in Figure 4-14. As the temperature is increased, the etching rate ecreases. This is believed to be due to the reduced adsorption of $NO_2$ on the diamond ırface at higher temperatures. At temperatures below -10°C, the etching rate decreases. At ıese low temperatures, a thick layer of $NO_2$ condenses on the sample and shields the iamond surface from the ion beam. Unless otherwise stated, all the measurements have een made at 0°C.

The etching rate of diamond at 0°C is 200 nm min., and suitable masking materials ıch as Si, Ni, and Al have been studied. Two problems still exist for the production of igh-quality structures: spikes which appear in the etched area and faceting of the masking ıaterial, which causes trenches to form at the edges of the etched structures. The trenching a direct result of the faceting; if faceting could be eliminated, then the trenching would o longer occur. Since the faceting is the result of the increased etch rate of the angled ıce, the facet can be eliminated by tipping the sample with respect to the ion beam. This :sults in an increased sputtering rate of the masking material and an increase in the :ching rate of the diamond substrate. Figure 4-15 is a plot of the etching rate of diamond nd the sputter etching rate of the Al mask as a function of the angle between the ion eam and the normal to the substrate. Figure 4-16 is a scanning electron micrograph ɔmparing two samples. The top micrograph is of a sample etched with the ion beam at

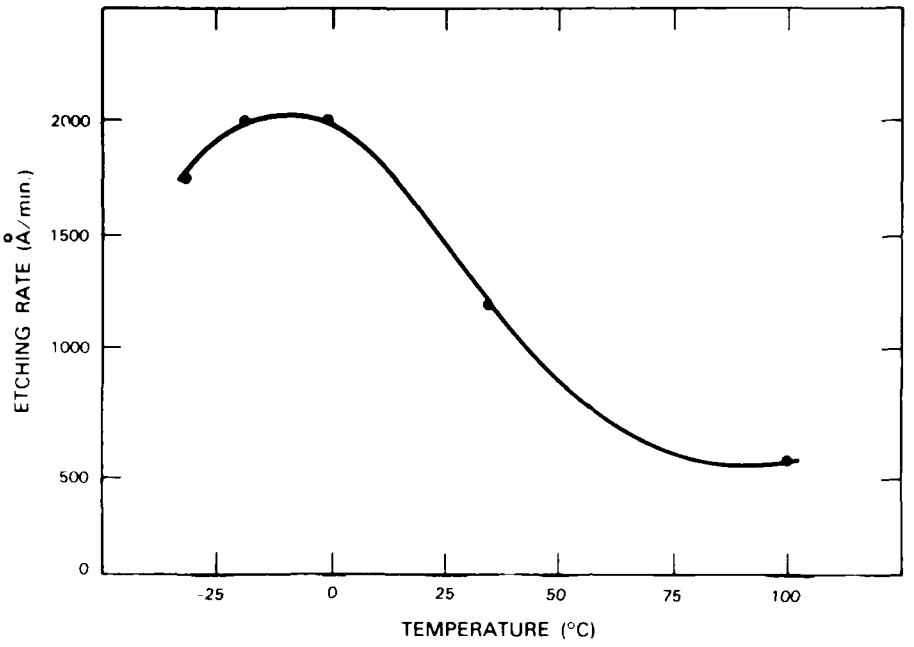


140913-N-02

Figure 4-14. The etching rate of diamond as a function of diamond temperature.

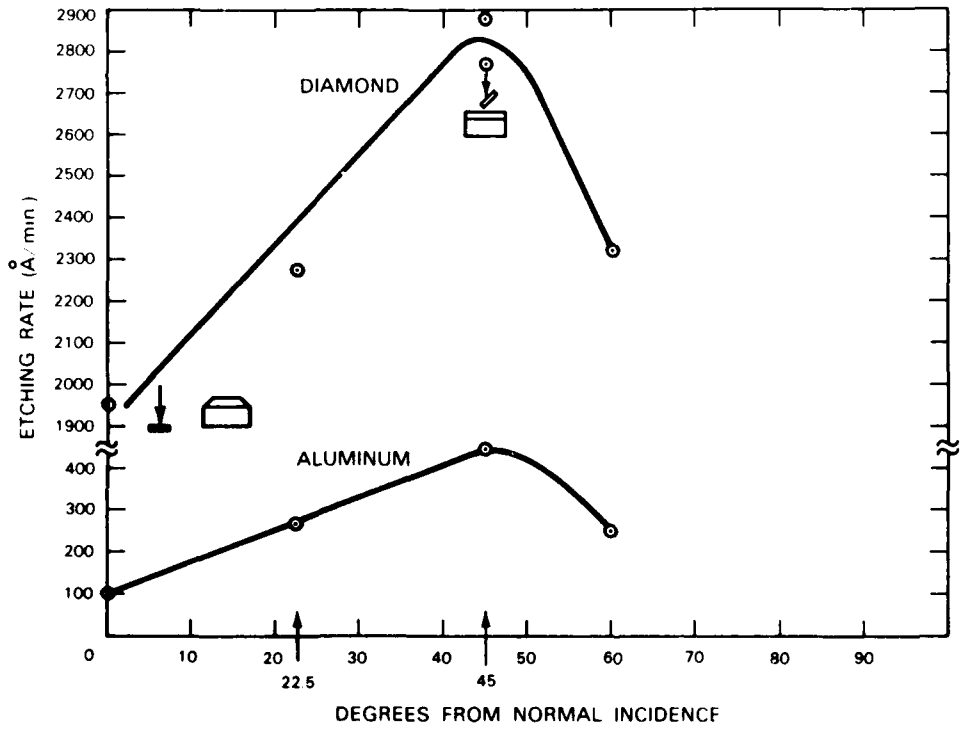


140557-N-02

Figure 4-15. The etching rate of diamond and the sputter etching rate of the Al mask as a function of the angle between the ion beam and the normal to the substrate.

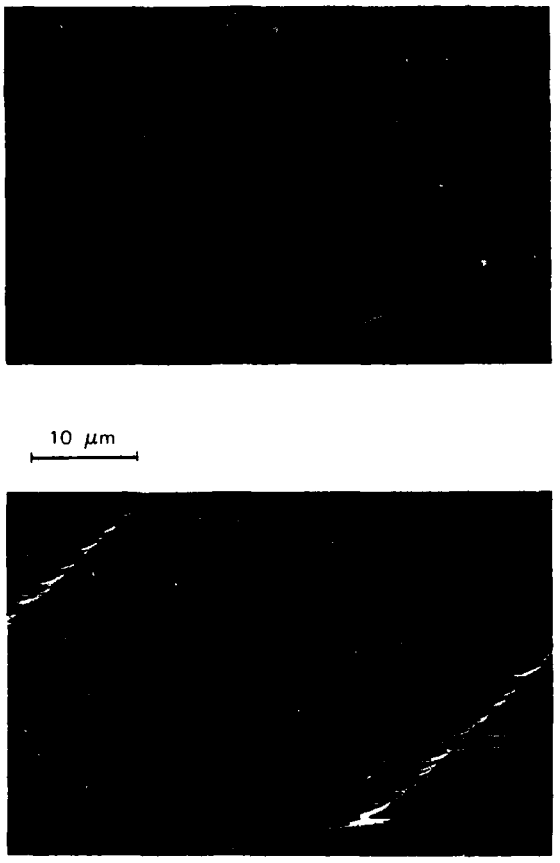


**Figure 4-16. SEM comparing two samples. The sample shown in the top micrograph was etched 10 μm deep with the ion beam at 45° to the substrate normal and the sample shown in the lower micrograph was etched with the ion beam normal to the substrate.**

AD-A154 783 SOLID STATE RESEARCH(U) MASSACHUSETTS INST OF TECH 2/2
LEXINGTON LINCOLN LAB A L MCWHORTER 15 AUG 84 1984-3
ESD-TR-84-042 F19628-85-C-0002

UNCLASSIFIED F/G 20/12 NL

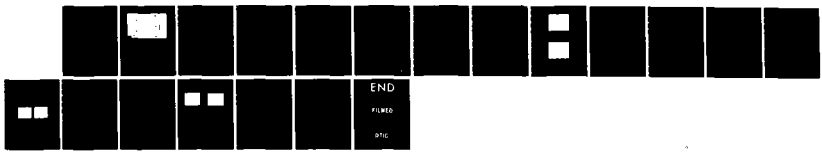

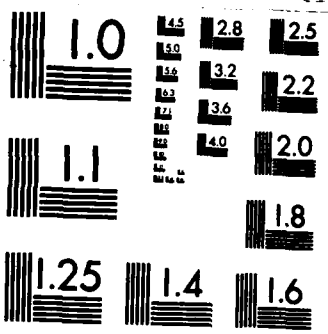

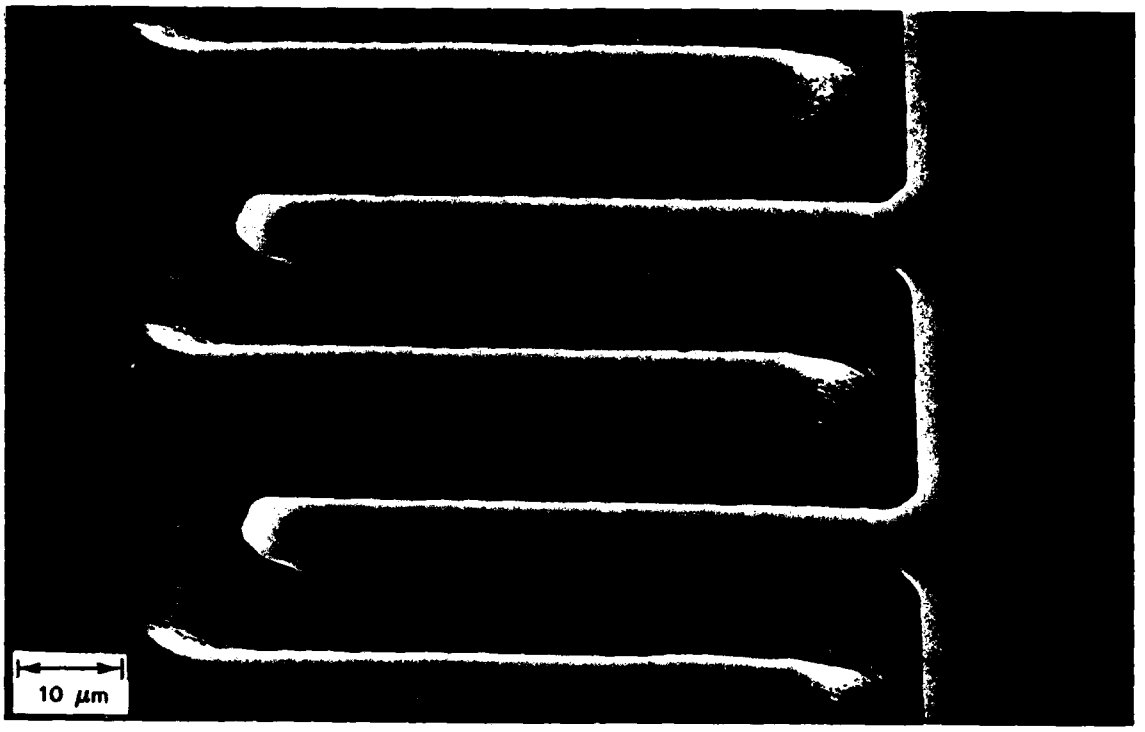


141364-R

**Figure 4-17. SEM of a periodic structure with 18-μm pitch etched 17 μm deep at 45°.**

45° to the substrate normal, and the lower micrograph is of a sample etched with the ion beam normal to the substrate. The etching at 45° has considerably less faceting and trenching.

An example of the structure needed for the traveling-wave device, etched at 45°, is shown in Figure 4-17. The structure consists of an 18-μm-period interdigital electrode pattern etched 17 μm deep.

N.N. Efremow
M.W. Geis
D.C. Flanders
G.A. Lincoln
N.P. Economou

## 4.5 PLANAR RECEPTORS AT 140 GHz USING DIPOLE ANTENNAS

The well-known advantages of monolithic circuit fabrication at microwave and millimeter-wave frequencies have prompted study of antenna elements which can be made in a planar form. Recently, we described a microstrip antenna on a quartz substrate made of two full-wavelength dipole antennas spaced $\lambda/2$ apart, which was tested near 140 GHz (Reference 13). This structure was operated as a receptor by using a GaAs Schottky diode placed between the dipoles for both heterodyne and direct detection.

A modification of this design has been completed, and significantly better antenna patterns and sensitivity have been obtained. Key changes were in the design of the low pass filter and the microstrip transmission line (see Figure 4-18). Some improvement may also be due to use of diodes from a different supplier.

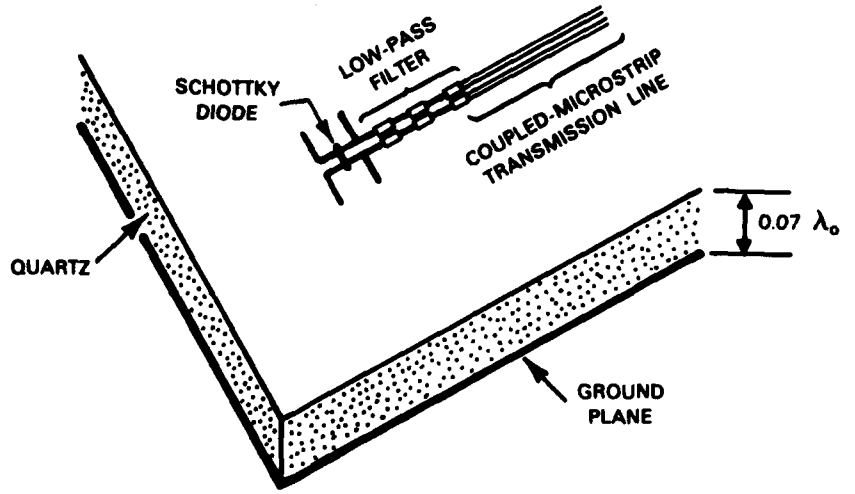


**Figure 4-18. Double dipole microstrip antenna on quartz substrate.**

The antenna and microstrip transmission lines were etched into a 2-$\mu$m-thick gold layer on a 150-$\mu$m-thick quartz substrate having a gold ground plane on the opposite side (see Figure 4-18). A GaAs beam-lead diode manufactured by AIL (Reference 14) (with zero-voltage capacitance of 7.6 pF and series resistance of 4.3 $\Omega$) was bonded into the circuit, equidistant from both dipoles.

E- and H-plane radiation patterns are shown in Figure 4-19. At 132 GHz E- and H-plane, 3 dB-widths of 48° and 63°, respectively, were measured. The separation of the dipoles was chosen so that the E- and H-plane widths would be similar. Other patterns taken at frequencies between 129 and 140 GHz are similar.

This structure was tested as a heterodyne mixer and as a video detector. For the heterodyne measurement, local oscillator power of 5 mW was supplied by a carcinotron, then combined with blackbody radiation in a diplexer and focused onto the antenna by an offset ellipsoidal mirror. The intermediate frequency signal was passed through a 1.4-GHz coaxial balun at the substrate edge and then amplified by an L-band low-noise amplifier. At 131.4 GHz, a receiver noise temperature of 4900 K (DSB) was obtained, which is a substantial improvement from our previous value of 1200 K (DSB) (Reference 15). The IF contribution to the receiver noise temperature was approximately 1000K. A video sensitivity of approximately 200 V/W was measured at 132 GHz, and at least 100 V/W was measured over a bandwith of about 8 GHz.

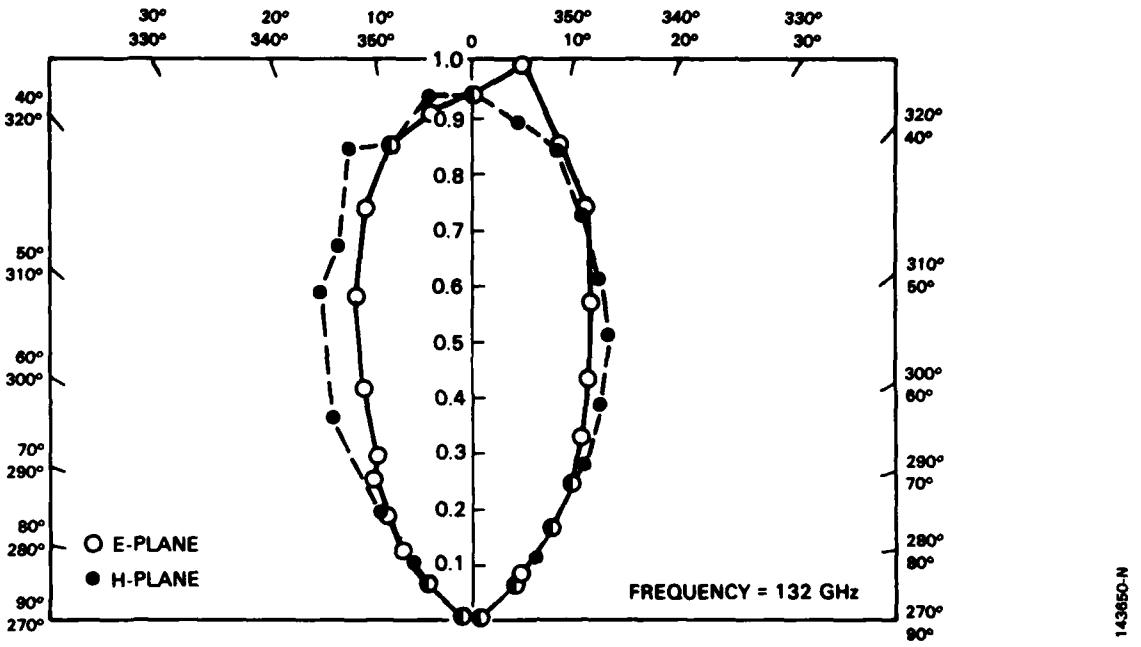


**Figure 4-19. E- and H-plane radiation patterns at 132 GHz.**

Because this receptor is planar and occupies a small area ($\sim 2\lambda^2$), it may be useful as one element in an imaging array. Toward this goal, further attention will be given to the mutual coupling between adjacent receptors and to the monolithic fabrication of the diode and antenna on a GaAs substrate.

J.A. Taylor
T.C.L.G. Sollner
J.A. Calviello*

* AIL Division of Eaton Corporation, Melville, New York.

## REFERENCES


1. R.H. Kingston, B.E. Burke, K.B. Nichols, and F.J. Leonberger, Appl. Phys. Lett. **41**, 413 (1982).
2. M.J Cohen, IEEE Intl. Electron Device Mtg., Washington, D.C., Technical Digest, December 1981, p. 622.
3. G.L. Hansell, "GaAs Schottky-Barrier Charge-Coupled Devices," Ph.D. dissertation, M.I.T., Department of Electrical Engineering, June 1982.
4. B.E. Burke, K.B. Nichols, J.T. Kelliher, and R.A. Murphy, Proc. 1982 Gallium Arsenide IC Symposium (1982) p. 45.
5. C.O. Bozler and G.D, Alley, IEEE Trans. Electron Devices **ED-27**, 1128 (1980).
6. G.D. Alley, C.O. Bozler, N.P. Economou, D.C. Flanders, M.W. Geis, G.A. Lincoln, W.T. Lindley, R.W. McClelland, R.A. Murphy, K.B. Nichols, W.J. Piacentini, S. Rabe, J.P. Salerno, and B.A. Vojak, IEEE Trans. Electron Devices **ED-29**, 1708 (1982).
7. M.A. Hollis, K.B. Nichols, C.O. Bozler, A.R. Calawa, and M.J. Manfra, 1984 Electronic Materials Conf., University of California, Santa Barbara.
8. B.L. Sharma, "Ohmic Contacts to III-IV Compound Semiconductors," Semiconductors and Semimetals **15**, 1 (1981).
9. C.Y. Su and C. Stolte, Electron. Lett. **19**, 891 (1983).
10. N.A. Papanicolaou and A. Christou, Electron. Lett. **19**, 418 (1983).
11. H.J. Gopen and A.Y.C. Yu, Solid State Electron. **14**, 515 (1971).
12. T.J. Whetten, A.A. Armstead, T.A. Grzybowski, and A.L. Ruoff, J. Vac. Sci. Technol. **A2**, 477 (1984).
13. P.T. Parrish, T.C.L.G. Sollner, R.H. Mathews, H.R. Fetterman, C.D. Parker, P.E. Tannenwald, A.G. Cardiasmenos, Proc. SPIE **337**, 49 (1982).
14. AIL Division of Eaton Corporation, Melville, New York
15. H.R. Fetterman, T.C.L.G. Sollner, P.T. Parrish, C.D. Parker, R.H. Mathews, and P.E. Tannenwald (to be published).

# 5. ANALOG DEVICE TECHNOLOGY

## 5.1 SURFACE-ACOUSTIC WAVE/FIELD-EFFECT TRANSISTOR WIDEBAND PROGRAMMABLE FILTER

Devices integrating surface-acoustic wave (SAW) delay lines for wideband input with charge-coupled devices for relatively low-speed programming or output have been reported previously.[1,2] Bandwidths of 40 MHz and delays of 3.5 μs with a dynamic range of 14 dB have been achieved. A new family of devices is now under development to increase both bandwidth and dynamic range. The devices use a SAW delay line air-gap coupled to a silicon chip containing an array of capacitive sampling fingers whose capacitance is controlled through a field-effect transistor (FET) array. Wider bandwidth is obtained with edge-bonded transducers (EBT), and larger dynamic range is made possible by the FET array which allows large variations in tap capacitance. The dynamic range is projected to be large enough to support operation as a waveform generator as well as a matched filter.

Such a programmable SAW filter has been built and tested. The filter impulse response is 1.5 μs long and the programmable bandwidth is 50 MHz centered at 150 MHz. The SAW delay line incorporates an EBT for a short pedestal of delay with high feedthrough isolation and very wide bandwidth. The use of EBTs in this context has been reported previously[3,4]

Figure 5-1 shows a schematic view of the air-gap structure including the EBT. The 3000-Å air gap allows coupling the electric fields which accompany the SAW to the circuitry in the silicon chip. The filter functions as a tapped delay line whose tap weights are programmable at a 1-MHz rate by means of the circuitry on the silicon chip. The 175 taps in the present device consist of metal sampling fingers over silicon dioxide which sample the energy propagating in the SAW delay line. The tap weights are programmed

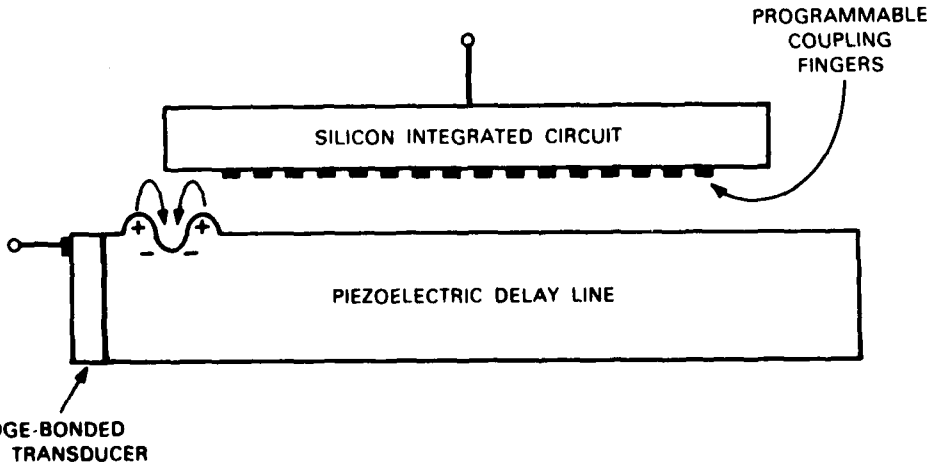


133089-N-02

**Figure 5-1. Schematic view of air-gap structure. The air gap is typically 3000 Å in height; the electric fields of the SAW delay line are coupled through the air gap into the silicon.**

utilizing the change in MOS capacitance with bias voltage. Programming is done through a single programming bus, which is connected in turn to the individual taps through an FET commutator switch controlled by an on-chip digital shift register. The filter output is obtained through a capacitive summing bus located on the chip. The tap and output circuit function as capacitive voltage dividers, as discussed below.

Figure 5-2 shows a schematic of the chip. In operation, a single bit is shifted through the shift register sequentially connecting each sampling finger, one at a time, to the programming bus. The programming voltage is applied externally at the appropriate time and is thereby sampled and stored on the capacitance of the tap. The dual track structure shown in the figure is used to suppress electromagnetic feedthrough and other spurious signals. The two SAW tracks are driven in phase and the filter output is taken as the difference of the signals on the two summing electrodes. Feedthrough and other common-mode spurious signals cancel out and the desired filter function is obtained by programming the two tracks in a differential manner.

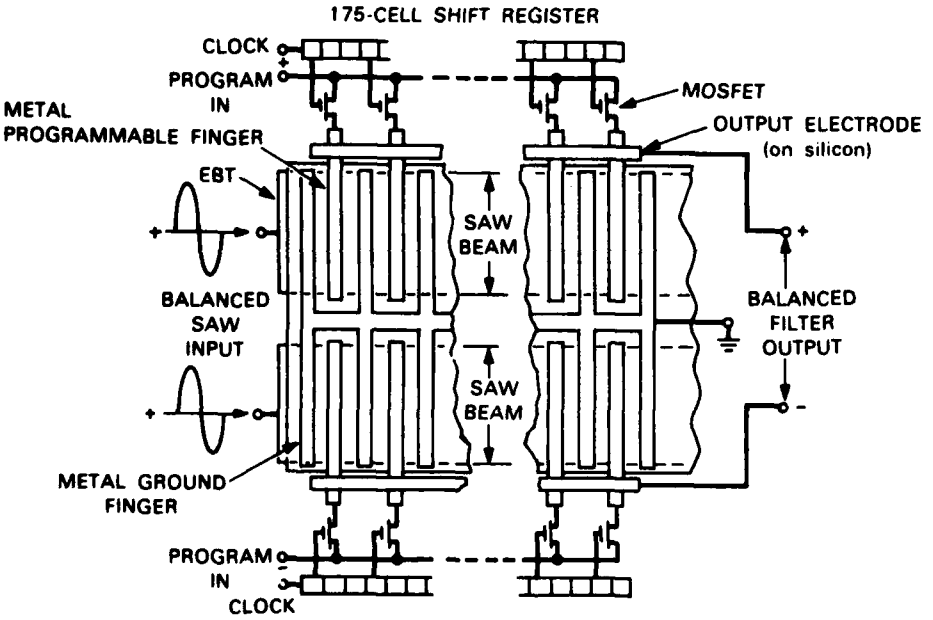


**Figure 5-2. Schematic view of the SAW/FET. The view is through the $LiNbO_3$ showing the alignment of the silicon chip with the SAW delay line.**

Figure 5-3 shows an equivalent circuit schematic of an individual tap of the filter. One sees that the device functions as a capacitive voltage divider. The indicated variable capacitor provides the programmability. Large values of tap capacitance imply small tap weight because the induced RF currents tend to be shorted to ground, and small capacitance implies large tap weights because RF currents are forced through the external

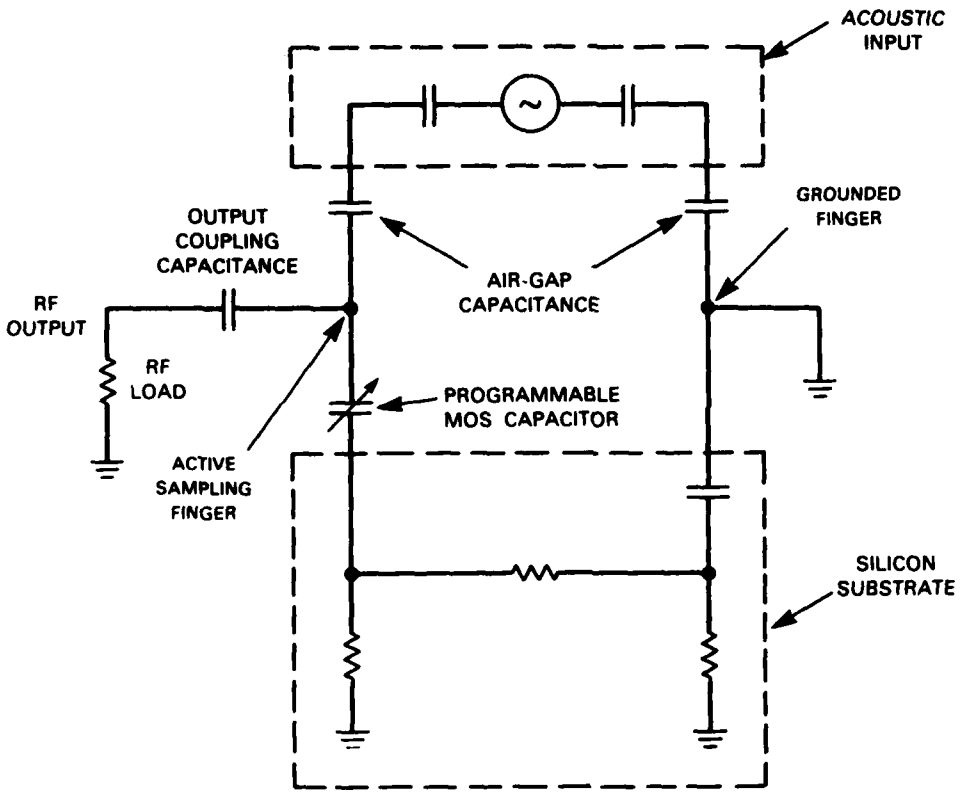


**Figure 5-3. Equivalent circuit of SAW/FET unit cell. Each track of the device contains 175 identical unit cells which drive the RF load in parallel. This unit cell is used for computations of the circuit model.**

load. The available range of capacitance values is determined by the MOS characteristics of the silicon. The dual track arrangement also serves to increase the effective dynamic range of the tap weights. When the taps are programmed to be off, there is still some residual signal due to the maximum capacitance which can be obtained. By operating the device in a differential manner, the residual tap weights can be made as small as the balance of the two identical tracks will allow.

An analytical device model has been developed based on the unit cell equivalent circuit given in Figure 5-3 . The model is able to predict accurately the RF device performance from measured low-frequency parameters of the silicon. Presently, experimental results agree well with predictions of the analytical model.

Figure 5-4 shows the performance of the SAW/FET when operated as a matched filter. The top trace in the photograph is the filter output; the middle trace is the input. Both traces are displayed on a time scale of 1 $\mu$s/cm. The bottom trace shows the input programming voltage, which is displayed on a time scale of 20 $\mu$s/cm. Superimposed on the bottom trace on the same time scale is the input to the shift register, which is a single bit

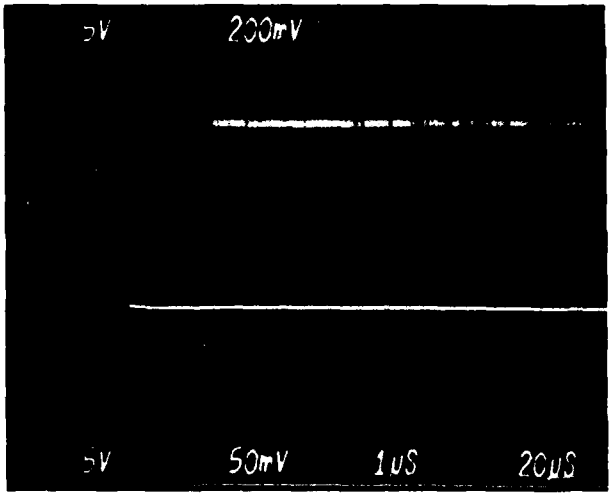


143656-S

**Figure 5-4. Output of SAW/FET operated as a matched filter. Top trace is output; middle trace is input, both displayed at 1 μs/div. Bottom trace is program input, in this case a sine wave of frequency 0.9 MHz. Superimposed on the bottom trace is the shift register bit which controls the FET switches. Bottom trace is displayed at 20 μs/div.**

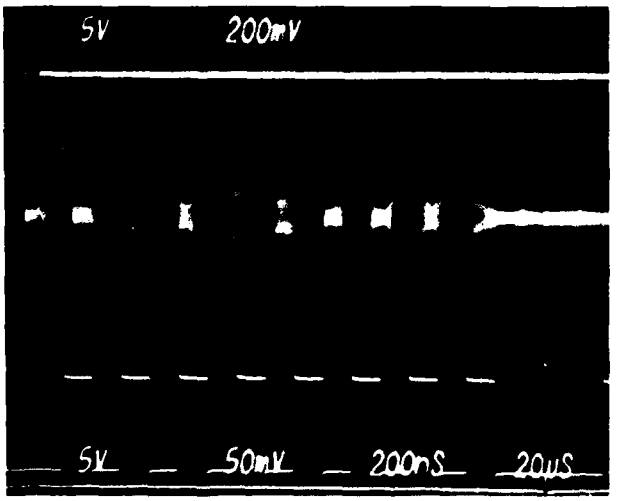


143657-S

**Figure 5-5. SAW/FET inpulse response for the programming waveform shown in the photograph. Top trace: input impulse; middle trace: filter output. Bottom: program input superimposed on shift register bit. Input and output are displayed at 200 ns/div. Program input is displayed at 20 μs/div. The programming voltage turns alternating groups of ten taps on and off.**

ntered externally. The filter input (middle trace) is a 1.5-$\mu$s RF burst at 129 MHz. The ength of the input signal is chosen to exactly fill the SAW delay line. The output is the xpected triangle which results from the correlation of two signals of exactly the same patial extent. The program input was a 0.90-MHz sine wave synchronized with the shift egister clocks. The shift register was being operated at a 1-MHz clock rate, and the clock nputs were halted at the time that the RF pulse was applied to the input. With a 1-MHz lock rate and a 0.9-MHz program waveform, the tap weights have a spatial period which orresponds to the wavelength of a 129-MHz SAW. The device was being programmed ifferentially so that the displayed output is the difference of the two acoustic tracks. In his case, one side of the device was simply programmed to have all taps at the minimum alues. Operated as a matched filter, the device presently has a dynamic range of approximately 30 dB.

Figure 5-5 shows the device impulse response with a programming voltage shown in the bottom of the picture. The device has been programmed with a square wave so that about 10 adjacent taps are programmed on and 10 taps are programmed off. The device impulse response gives the single tap programmable dynamic range. From the figure, one sees that the single tap dynamic range is between 6 and 10 dB depending upon position in the device. The dependence of dynamic range on position is a result of the balance between the two tracks and is not a fundamental problem. The balance is determined by the uniformity of the silicon chip and the air gap. The SAW delay line itself shows a very high degree of balance. Improvements in the uniformity of the chip will improve the balance.

In the device pictured, the single track dynamic range, that is, the dynamic range without the enhancement provided by the dual track structure, is about 3dB. The measured values of the dynamic range agree with calculated results from the analytical model. Presently the dynamic range is limited by the capacitance vs voltage characteristics of the MOS sampling fingers. Since larger capacitance variations than currently utilized are, in principle, possible, increases in dynamic range to approximately 15 dB for a single track can be accomplished by means of changes in silicon processing. Experiments in this direction are presently under way.

D. E. Oates A. C. Anderson
D.L. Smythe J. B. Green

## 5.2 InP OPTOELECTRONIC SAMPLER FOR A WIDEBAND RADAR SIGNAL PROCESSOR

InP optoelectronic switches have shown switching times ranging from 6 ns to <100 ps and on-off ratios exceeding six orders of magnitude.[5-7] One of the important applications of such switches is in high-speed track-and-hold circuits for the sampling of wideband analog signals.[7,8] Two important advantages of the optoelectronic switch over conventional diode bridges are its inherent optical isolation and its zero DC offset. Here the implementation of a high-speed track-and-hold circuit based on an InP optoelectronic switch designed for a wideband radar hybrid signal processor [9] will be described. Topics to be covered include circuit design, switch input-to-output leakage and its circumvention, and circuit performance.

In the hybrid radar signal processor, optoelectronic track-and-hold circuits will buffer the analog signal path from a SAW convolver-based matched filter[10] to a Doppler processor incorporating charge-coupled device matrix-matrix product (CCD MMP) chips.[11] The performance requirements of the track-and-hold circuit in this system call for a 200-MHz analog bandwidth, 10-ns sampling period, with 2 to 3 ns for tracking and 7 to 8 ns for holding, and better than 1 percent accuracy in terms of input-to-output leakage, droop, and residual charge from the previously sampled value.

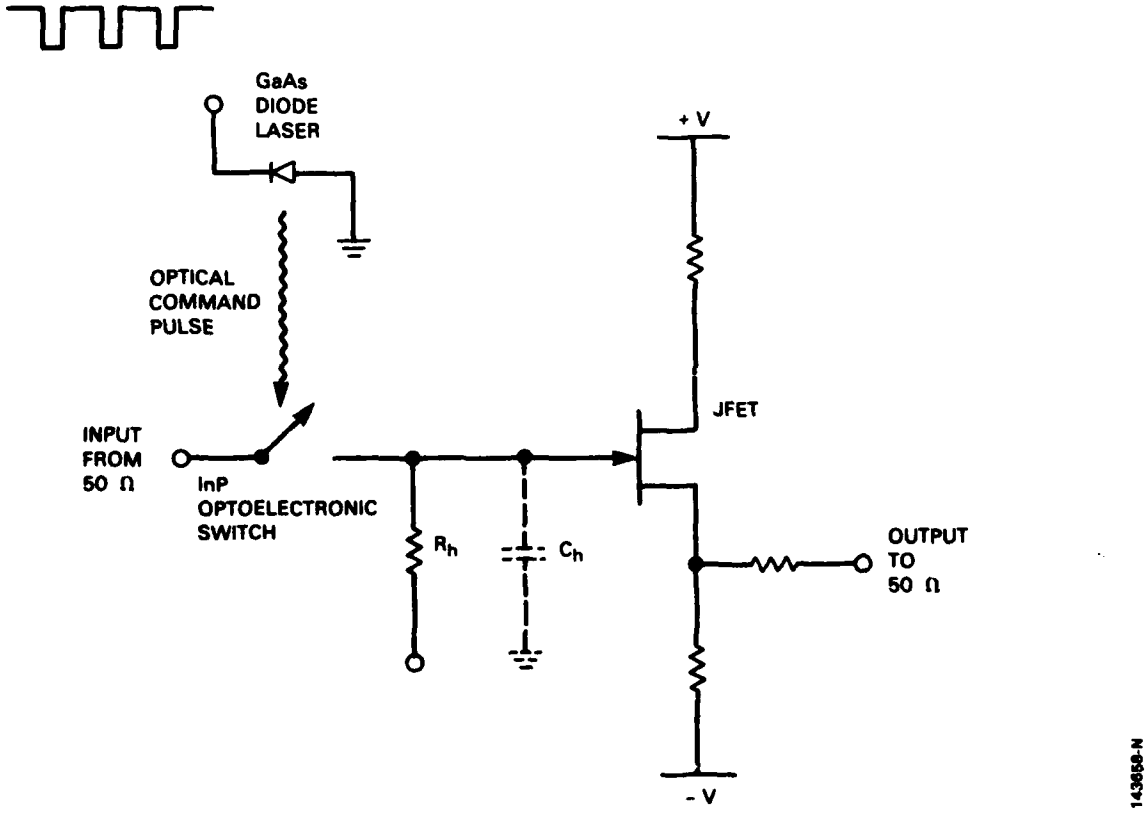


**Figure 5-6. Circuit diagram of the optoelectronic track-and-hold.**

The track-and-hold circuit is shown in Figure 5-6. The JFET source follower shown is the track-and-hold output buffer amplifier; its input gate capacitance is used as the hold capacitor.

It is helpful to consider the equivalent circuit shown in Figure 5-7(a). Here the optoelectronic switch is modeled as a time varying conductance, $G_s(t)$ [Figure 5-7(b)], whose turn-on and off transients are assumed to be simple exponentials with time constants determined by the actual measured value of switch transient conductance, in parallel with a

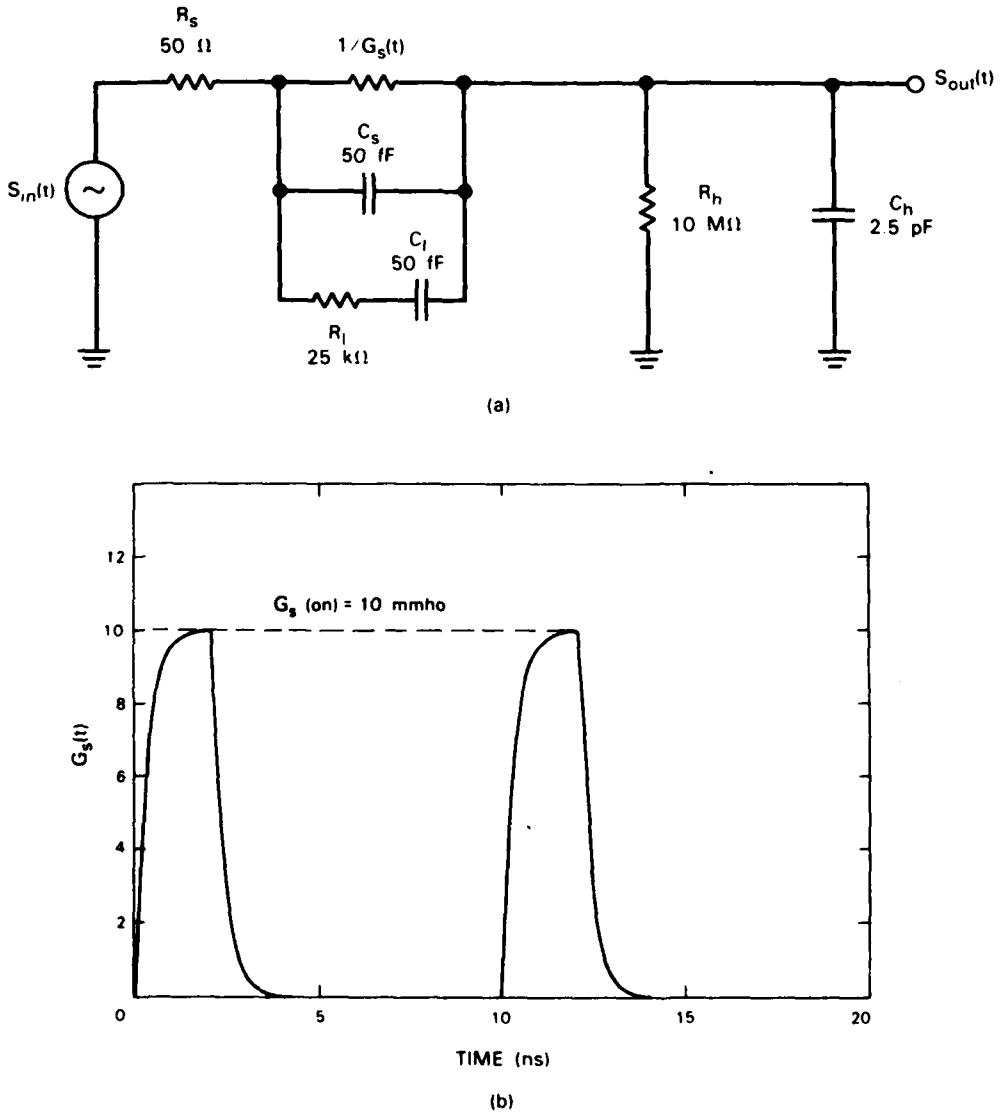


**Figure 5-7. (a) Equivalent circuit for optoelectronic track-and-hold; (b) model of the time-variant conductance of InP switch, $G_s(t)$, controlled by the laser command pulses.**

ıall parasitic capacitor, $C_s$. In the rest of the circuit, $R_s$ specifies the source resistance, d $C_h$ and $R_h$ are the hold capacitor and the bypass resistor, respectively. $R_l$ and $C_l$ are ıkage elements which are discussed later.

Of primary importance is the switch transient response time. The InP optoelectronic ıitch used is fabricated on Fe-doped semi-insulating InP substrates by introducing Fe ıping during crystal growth. It has a transient response time constant of about 300 ps ıtermined by the carrier lifetime of Fe-doped InP material. This time constant can be rther reduced through ion bombardment and thermal annealing,[5-7] but this process pically reduces device optical sensitivity as well as the on/off conductivity ratio and erefore is not suitable for our track-and-hold application. The 300-ps transient response ne constant of switches fabricated on Fe-doped substrate ultimately limits its impulse sponse to a 3-dB analog bandwidth of 350 MHz. Furthermore, the time constant of the rcuit, $R_{on}C_h$, where $R_{on}$ is the series combination of the source resistance, $R_s$, and switch ı-resistance, $1/G_s(on)$, further reduces the analog bandwidth. However, the added effect of ior-sample residue places more severe constraints on circuit performance. In the 2-ns ımpling window budgeted, there should be at least 5 $R_{on}C_h$ time constants to allow the ior-sample residue to decay to 1 percent of its original value. This requires an $R_{on}C_h$ ınstant of 400 ps during the 2-ns sampling window. For a 2.5-pF hold capacitance (the ıput gate capacitance of the JFET used in the output buffer amplifier), an $R_{on}$ of $<160\ \Omega$ required. Since the signal propagates in a nominal 50-$\Omega$ environment, the on-resistance of ıe switch, $1/G_s(on)$, should be below 110 ohm. With switches with typical optical ınsitivity, $1/G_s(on)$ of 100 $\Omega$ is attainable with optical power supplied by a commercial aAs diode laser. For the combination of a switching time constant of 300 ps and ıpacitor charging time constant of 400 ps, the calculated circuit response function, $h(t,\tau)$, emonstrates a 3-dB analog bandwidth of 260 MHz, which is more than adequate for the )0-MHz requirement cited earlier.

In a time-variant linear circuit such as the track-and-hold being modeled, the impulse sponse can no longer be defined simply by $h(t-\tau)$ as in a time-invariant linear circuit.[12] ıstead, the circuit response in the time domain is described by

$$S_{out}(t) = \int S_{in}(\tau)\ h(t,\ \tau)\ d\tau \quad .$$

To prevent input-to-output leakage during the hold mode, the switch should have large ff-resistance and well-behaved parasitics. For a 2.5-pF hold capacitance, the off-resistance ıould be $>400$ k$\Omega$ ($R_{off}C_h > 1$ $\mu$s), which translates into a resistance on/off ratio of 4000 ) achieve $<1$ percent leakage during 10-ns time period. Likewise, the bypass resistance, $R_h$, ıould also be $>400$ k$\Omega$ to maintain $<1$ percent droop to ground. The actual value of $R_h$ ıed is 10 M$\Omega$ for JFET input gate biasing and therefore droop is not of concern in this articular case. Furthermore, the parasitic capacitance, $C_s$, should also be $<1$ percent of the old capacitance, $C_h$, which resulted in a $C_s$ of $<25$ fF.

Although the switch off-resistance obtained in DC measurements is well over 1MΩ, input-to-output leakages during the hold mode persist in actual circuit responses. More detailed experimental evidence reveals that after each optical command pulse there is residual conduction decaying very slowly with respect to the time scale of the 10-ns sampling period. The magnitude of this residual conduction is found to be not only time dependent but also device-geometry and bias dependent during both the track period and the hold period. The leakage is thought to be caused by deep trapping levels other than the desired recombination centers and/or nonohmic contact electrodes. Figure 5-8 shows the geometry

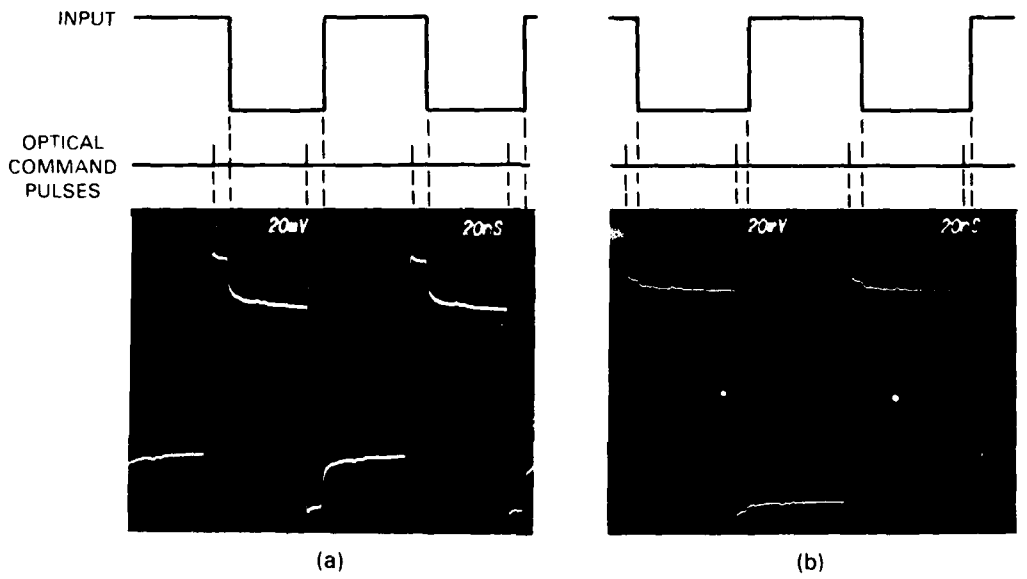


131243 R 01

**Figure 5-8. Square-wave responses of optoelectronic track-and-hold circuits using (a) a 2-μm switch, and (b) a 6-μm switch.**

dependence of this leakage effect. The devices under test have electrode width and spacing of 2 and 6 μm. The sampled waveforms are square waves. The small sharp steps shown in the output waveforms are caused by input-to-output leakage through the parasitic capacitor, $C_s$, while the input waveforms are making their transitions. The slow droops right after them are caused by the slowly decaying residual conductance. It is evident that the leakage effects are much more severe in 2-μm devices than 6-μm devices. Owing to this result, 6-μm devices are used in our circuits even though their sensitivity, which requires 40 mW of optical power to achieve the on-resistance of 100 Ω, is inferior to that of devices with smaller geometry.

For the 6-μm devices, the shunt capacitor $C_s$ was determined to have a value of 50 fF. The series combination of $R_l$ and $C_l$ are added to the equivalent circuit to model the slowly decaying residual conductance (Figure 5-7). In reality, these are time-varying elements;

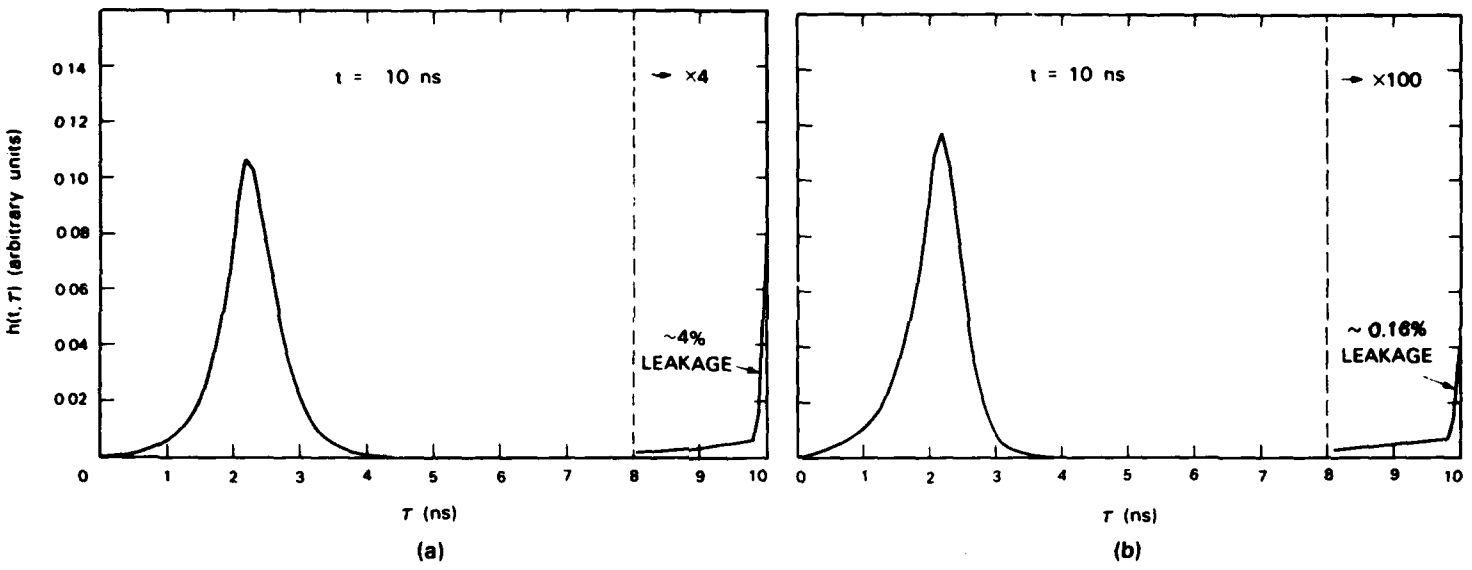


**Figure 5-9. SPICE simulated response functions, h(t,τ), of optoelectronic track-and-hold circuits for (a) single stage, and (b) two cascaded stages.**

143660-N

however, for a sampling period of 10 ns, they are well approximated by fixed elements of 25 kΩ and 50 fF. The response function, $h(t,\tau)$, of this equivalent circuit has been calculated with the SPICE circuit simulation program. Figure 5-9(a) shows a slice of the response function, $h(t_1,\tau)$, for $t_1$ = 10 ns. It is convenient to define an observation time, $t = t_1$, in the hold mode such that the circuit output signal at $t_1$ seconds after the laser command pulse is generated, $S_{out}(t_1)$, can be expressed as

$$S_{out}(t_1) = \int S_{in}(\tau)\ h(t_1,\ \tau)\ d\tau \quad ,$$

similar to the time-invariant linear circuit using impulse response $h(t - \tau)$. From it, the equivalent sampling pulse, leakage effect, and circuit analog bandwidth can be defined. Its analog bandwidth remains 260 MHz while the input-to-output leakage is calculated to be about 4 percent.

To achieve a system accuracy of 1 percent, the switch leakage during the hold mode must be better controlled. Besides the improvements of device characteristics, two identical track-and-holds cascaded in series would also improve circuit isolation from the 4 percent single-stage value to 4 percent of 4 percent, i.e., 0.16 percent. The cascaded track-and-hold circuit has also been simulated using SPICE. Figure 5-9(b) shows the calculated response function, $h(t,\tau)$, which indeed indicates leakage less than 0.2 percent.

Both single track-and-hold and cascaded track-and-hold circuits have been tested. Figures 5-10(a) and (c) show the actual results of track-and-hold operation with 110-MHz sine-wave inputs and sampling at a 100-MHz rate. The staircase-like output waveforms have beat frequencies of 10 MHz. The pictures clearly show the superior isolation achieved by the cascaded track-and-hold. Also shown in Figures 5-10(b) and (d) are their respective SPICE simulation results. The good agreement between simulation and experiment is evident.

Because of their fast switching time, high on/off ratio, and optically isolated command pulse, optoelectronic switches perform well in high-speed track-and-hold applications. If reasonable sensitivity is maintained and the on/off ratio is improved for switches demonstrating a transient time <100 ps, sampling rates over 1 GHz can be projected. A track-and-hold circuit based on an InP optoelectronic switch with a switching time constant of 300 ps has been developed. A slowly decaying residual conductance severely degrades the circuit input-to-output isolation, necessitating the use of two cascaded track-and-holds. A 260-MHz analog bandwidth, 100-MHz sampling rate, and better than 1 percent accuracy was demonstrated in this cascaded configuration. Further work must identify the causes of and cures for the switch leakage effect.

I. Yao
V. Diadiuk

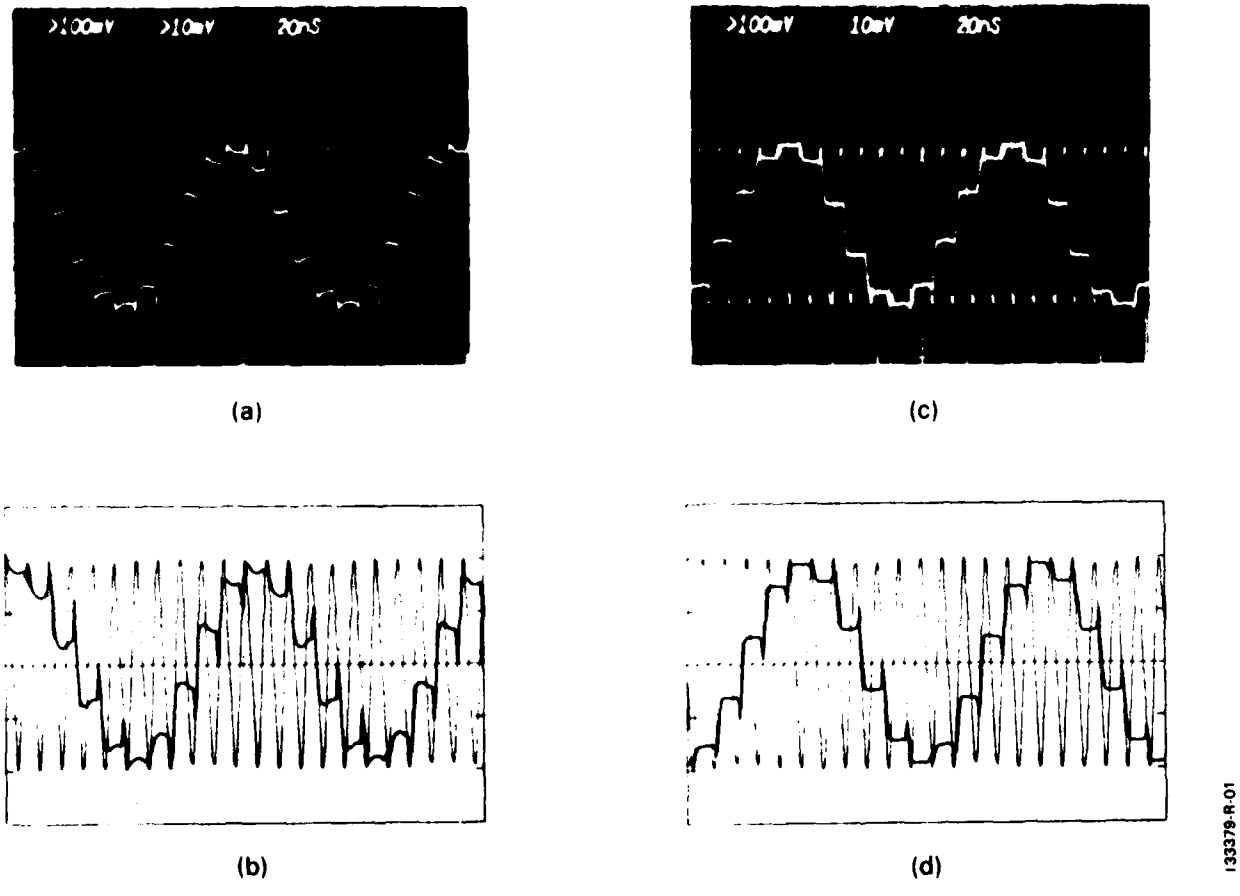


**Figure 6-10. Responses of track-and-hold circuits to 110-MHz sine wave inputs with a 100-MHz sampling rate. (a) Experimental and (b) simulated responses for single-stage track-and-hold; (c) experimental and (d) simulated responses for two-stage track-and-hold.**

## REFERENCES


1. Solid State Research Report, Lincoln Laboratory M.I.T. (1981:3), p. 35, DTIC AD-A112696/0.

2. D.L. Smythe, R.W. Ralston, and E. Stern, *1979 Ultrasonics Symposium Proceedings* (IEEE, New York, 1979), pp. 767-770.

3. Solid State Research Report, Lincoln Laboratory, M.I.T. (1981:4), p. 55, DTIC AD-A114189/4.

4. D.E. Oates and R.W. Ralston, *1981 IEEE Ultrasonics Symposium Proceedings* (IEEE, New York, 1981), pp. 44-47.

5. Solid State Research Report, Lincoln Laboratory, M.I.T. (1981:4), p. 4. DTIC AD-A114189/4.

6. *Ibid.* (1982:1), p. 1, DTIC AD-A118847.

7. A.G. Foyt and F.J. Leonberger, to be published in *Picosecond Optoelectronic Devices*, C.H. Lee, Ed. (Academic Press, New York, 1984).

8. C.H. Cox III, V. Diadiuk, I. Yao, F.J. Leonberger, and R.C. Williamson, Proc. SPIE **439**, 164 (1983).

9. I. Yao, E.M. Hauser, C.A. Bouman, G.T. Flynn, and J.H. Cafarella, 1984 IEEE Ultrasonics Symp., Dallas, TX.

10. Solid State Research Report, Lincoln Laboratory, M.I.T. (1983:3), p. 83, DTIC AD-A140027/4.

11. A.M. Chiang, R.W. Mountain, D.J. Silversmith, and B.J. Felton, Technical Digest, *1984 Intl. Solid-State Circuits Conference* (IEEE, New York, 1984), pp. 110-111; Solid State Research Report, Lincoln Laboratory, M.I.T. (1983:3), p. 71.

12. W.H. Kim and H.E. Meadows, Jr., *Modern Network Analysis*, Chapter 10 (Wiley, New York, 1971).

UNCLASSIFIED

SECURITY CLASSIFICATION OF THIS PAGE (When Data Entered)

| REPORT DOCUMENTATION PAGE | | READ INSTRUCTIONS BEFORE COMPLETING FORM |
|---|---|---|
| 1. REPORT NUMBER<br>ESD-TR-84-042 | 2. GOVT ACCESSION NO.<br>AD-A154 783 | 3. RECIPIENT'S CATALOG NUMBER |
| 4. TITLE (and Subtitle)<br>Solid State Research | | 5. TYPE OF REPORT & PERIOD COVERED<br>Quarterly Technical Report<br>1 May — 31 July 1984 |
| | | 6. PERFORMING ORG. REPORT NUMBER<br>1984:3 |
| 7. AUTHOR(s)<br>Alan L. McWhorter | | 8. CONTRACT OR GRANT NUMBER(s)<br>F19628-85-C-0002 |
| 9. PERFORMING ORGANIZATION NAME AND ADDRESS<br>Lincoln Laboratory, M.I.T.<br>P.O. Box 73<br>Lexington, MA 02173-0073 | | 10. PROGRAM ELEMENT, PROJECT, TASK AREA & WORK UNIT NUMBERS<br>Program Element No. 63250F<br>Project No. 649L |
| 11. CONTROLLING OFFICE NAME AND ADDRESS<br>Air Force Systems Command, USAF<br>Andrews AFB<br>Washington, DC 20334 | | 12. REPORT DATE<br>15 August 1984 |
| | | 13. NUMBER OF PAGES<br>120 |
| 14. MONITORING AGENCY NAME & ADDRESS (if different from Controlling Office)<br>Electronic Systems Division<br>Hanscom AFB, MA 01731 | | 15. SECURITY CLASS. (of this report)<br>Unclassified |
| | | 15a. DECLASSIFICATION DOWNGRADING SCHEDULE |

16. DISTRIBUTION STATEMENT (of this Report)

Approved for public release; distribution unlimited.

17. DISTRIBUTION STATEMENT (of the abstract entered in Block 20, if different from Report)

18. SUPPLEMENTARY NOTES

None

19. KEY WORDS (Continue on reverse side if necessary and identify by block number)

solid state devices
quantum electronics
materials research
microelectronics
analog device technology
photodiode devices
lasers
laser spectroscopy
imaging arrays
signal processing
infrared imaging
surface-wave transducers
charge-coupled devices
acoustoelectric devices

20. ABSTRACT (Continue on reverse side if necessary and identify by block number)

This report covers in detail the solid state research work of the Solid State Division at Lincoln Laboratory for the period 1 May through 31 July 1984. The topics covered are Solid State Device Research, Quantum Electronics, Materials Research, Microelectronics, and Analog Device Technology. Funding is primarily provided by the Air Force, with additional support provided by the Army, DARPA, Navy, NASA, and DOE.

DD FORM 1 Jan 73 1473 EDITION OF 1 NOV 65 IS OBSOLETE

UNCLASSIFIED

SECURITY CLASSIFICATION OF THIS PAGE (When Data Entered)

END

FILMED

7-85

DTIC